

**University of Alberta**

*Study of Anode Materials for the Application in a H<sub>2</sub>S Compatible Direct Oxidizing Solid Oxide Fuel Cell*

by

*Joyce Ai Ling Funk*



A thesis submitted to the Faculty of Graduate Studies and Research in partial fulfillment of the requirements for the degree of Master of Science

in

*Chemical Engineering*

Department of *Chemical and Materials Engineering*

Edmonton, Alberta

*Spring 2006*



Library and  
Archives Canada

Bibliothèque et  
Archives Canada

Published Heritage  
Branch

Direction du  
Patrimoine de l'édition

395 Wellington Street  
Ottawa ON K1A 0N4  
Canada

395, rue Wellington  
Ottawa ON K1A 0N4  
Canada

*Your file* *Votre référence*  
*ISBN: 0-494-13813-0*  
*Our file* *Notre référence*  
*ISBN: 0-494-13813-0*

**NOTICE:**

The author has granted a non-exclusive license allowing Library and Archives Canada to reproduce, publish, archive, preserve, conserve, communicate to the public by telecommunication or on the Internet, loan, distribute and sell theses worldwide, for commercial or non-commercial purposes, in microform, paper, electronic and/or any other formats.

The author retains copyright ownership and moral rights in this thesis. Neither the thesis nor substantial extracts from it may be printed or otherwise reproduced without the author's permission.

**AVIS:**

L'auteur a accordé une licence non exclusive permettant à la Bibliothèque et Archives Canada de reproduire, publier, archiver, sauvegarder, conserver, transmettre au public par télécommunication ou par l'Internet, prêter, distribuer et vendre des thèses partout dans le monde, à des fins commerciales ou autres, sur support microforme, papier, électronique et/ou autres formats.

L'auteur conserve la propriété du droit d'auteur et des droits moraux qui protègent cette thèse. Ni la thèse ni des extraits substantiels de celle-ci ne doivent être imprimés ou autrement reproduits sans son autorisation.

---

In compliance with the Canadian Privacy Act some supporting forms may have been removed from this thesis.

Conformément à la loi canadienne sur la protection de la vie privée, quelques formulaires secondaires ont été enlevés de cette thèse.

While these forms may be included in the document page count, their removal does not represent any loss of content from the thesis.

Bien que ces formulaires aient inclus dans la pagination, il n'y aura aucun contenu manquant.

  
**Canada**

## **Abstract**

The purpose of this research is focused on the analysis of potential sulfur resistant anode materials and on developing an understanding of the reactivity and kinetics on methane oxidation for the application in a H<sub>2</sub>S compatible SOFC. This research examines Ni/YSZ, Cu/YSZ, Ni/Cu/YSZ and two different preparations of LiCoO<sub>2</sub>/YSZ for the direct oxidation of methane at 500 – 800 °C. It was found Ni/YSZ is severely poisoned by H<sub>2</sub>S (~100ppm). Ni/Cu/YSZ also exhibits H<sub>2</sub>S degradation, while Cu/YSZ did not show any H<sub>2</sub>S degradation at high temperatures (700 and 800 °C). However, at low temperatures (500 and 600 °C), all of the catalysts exhibit severe H<sub>2</sub>S degradation with the exception of LiCoO<sub>2</sub>/YSZ. The LiCoO<sub>2</sub>/YSZ catalysts were not affected by H<sub>2</sub>S. Unfortunately, the LiCoO<sub>2</sub>/YSZ catalysts exhibit lower reactivity towards methane oxidation compared to the Cu/YSZ catalyst. Thus, Cu/YSZ would be the best candidate as a potential SOFC anode in the presence of H<sub>2</sub>S.

## **ACKNOWLEDGEMENTS**

This degree was completed with the help of many people. I would like to thank my supervisor, Dr. Nelson for all his support, guidance and patience. I would also like to give a special thanks to my parents that have been very supportive and patient throughout my education. I would also like to thank Dr. Maham for his encouragement and positive attitude throughout my study here at the University of Alberta. I also greatly appreciate all of the group members that helped me with my studies and also thank them for all their kindness and encouragement. I would like to thank Wa'el Abdallah, Alex Abraham, Becky DeMott, Brian Greenhalgh, Claudia Guarino, Abu Saleh Junaid, Carolyn Kenney, Pete Punwin, Martina Rusnacik, Mingyong Sun and Zhenhui Wang, I acknowledge the Natural Sciences and Engineering Research Council (NSERC) for all their funding. I also would like to thank Dr. Etsell for all his help and encouragement. I would also like to thank Andree Koenig and the technical support group for all their help.

## TABLE OF CONTENTS

### CHAPTER 1: INTRODUCTION

1.1	Introduction .....	1
1.2	Fuel Cells.....	2
1.2.1.	Introduction to Fuel Cells .....	2
1.2.2.	Applications of Fuel Cells.....	3
1.2.3.	Types of Fuel Cells .....	5
1.2.4.	Solid Oxide Fuel Cell Operation and Benefits .....	8
1.3	Fuel Cells and Hydrogen Sulfide Containing Fuels .....	10
1.4	Research Objectives .....	12

### CHAPTER 2: LITERATURE REVIEW

2.1	General Introduction to Solid Oxide Fuel Cells .....	13
2.2	Components and Materials of SOFCs .....	16
2.2.1	Solid Electrolytes .....	17
2.2.2	Anodes .....	22
2.2.3	Cathodes .....	25
2.3	Reforming of Hydrocarbon Fuels in SOFCs .....	26
2.4	Thermodynamics of Fuel Cells .....	30
2.5	Direct Oxidation of Hydrocarbons in SOFCs .....	33
2.6	Fuel Cell Research using H <sub>2</sub> S .....	40
2.7	Summary of Literature Review .....	47

### CHAPTER 3: EXPERIMENTAL METHODS

3.1	Objective .....	50
3.2	Materials used for Catalyst Preparation and Testing.....	50
3.3	Catalyst Preparation .....	51
3.4	Characterization by X-ray Photoelectron Spectroscopy .....	53
3.4.1	XPS Sample Preparation .....	56
3.5	Brunauer-Emmett-Teller (BET) Surface Area Characterization .....	56

3.5.1	AutoChem II 2920 (Automated Catalyst Characterization System) .....	58
3.5.2	Sample Preparation .....	59
3.5.3	BET Experimental Procedure .....	61
3.6	Anode Material Reaction Analysis on Methane Oxidation .....	63
3.6.1	Experimental Procedure for Running Reaction Tests .....	63
3.6.2	Analysis of Product Gas using a Mass Spectrometer .....	65

#### CHAPTER 4: RESULTS

4.1	XPS Characterization Results .....	68
4.2	BET Surface Area Characterization .....	70
4.3	Anode Material Analysis on Methane Oxidation .....	71
4.3.1	Calculating Methane Conversion .....	71
4.3.2	Methane Conversion Results on Catalysts Performed without H <sub>2</sub> S .....	73
4.3.3	Methane Conversion Results on Catalysts Performed in the Presence of H <sub>2</sub> S .....	76
4.3.4	CO <sub>2</sub> Selectivity Results .....	79
4.3.4.1	CO <sub>2</sub> Selectivity Results for Catalysts in a H <sub>2</sub> S-free Environment .....	79
4.3.4.2	CO <sub>2</sub> Selectivity Results for Catalysts in a H <sub>2</sub> S Environment .....	81
4.3.5	Catalyst Degradation .....	83
4.4	Methane Oxidation Reaction Kinetic Analysis .....	85
4.4.1	Reaction Kinetic Parameters for Catalysts without H <sub>2</sub> S .....	86
4.4.2	Reaction Kinetic Parameters for Catalysts in the Presence of H <sub>2</sub> S .....	87
4.4.3	Rate of Disappearance of Methane as a Function of Methane Partial Pressure for the Catalysts in an H <sub>2</sub> S-free Environment .....	88
4.4.4	Rate of Disappearance of Methane as a Function of Methane Partial Pressure for the Catalysts in an H <sub>2</sub> S Environment .....	92

#### CHAPTER 5: DISCUSSION

5.1	XPS Analysis and BET Surface Measurements .....	97
5.2	Methane Conversion and CO <sub>2</sub> Selectivity Analysis .....	99

5.3	Reaction Kinetic Analysis on Methane Oxidation Reactions .....	102
-----	----------------------------------------------------------------	-----

CHAPTER 6: CONCLUSIONS AND RECOMMENDATION

6.1	Conclusions .....	107
-----	-------------------	-----

6.2	Recommendations and Future Work .....	108
-----	---------------------------------------	-----

REFERENCES .....	111
------------------	-----

APPENDIX A (Reaction Kinetic Data).....	115
-----------------------------------------	-----

## LIST OF TABLES

### CHAPTER 1

Table 1-1	Technical characteristics of various types of fuel cells.....	6
-----------	---------------------------------------------------------------	---

### CHAPTER 3

Table 3-1	Compositions of metal nitrates and YSZ used for catalyst preparation using wet impregnation .....	52
Table 3-2	Composition of carbonates and YSZ used for catalyst preparation using a solid -state reaction method .....	53
Table 3-3	Inlet flow rate conditions and compositions of gases used in reaction tests.....	64

### CHAPTER 4

Table 4-1	Metal compositions and oxidation states determined from XPS .....	69
Table 4-2	Multipoint BET surface area measurements .....	71
Table 4-3	CO <sub>2</sub> selectivity results for catalysts in an H <sub>2</sub> S-free environment .....	80
Table 4-4	CO <sub>2</sub> selectivity results for catalysts in an H <sub>2</sub> S environment .....	82
Table 4-5	Reaction parameters for methane oxidation on catalysts exposed without H <sub>2</sub> S .....	87
Table 4-6	Reaction parameters for methane oxidation on catalysts exposed in H <sub>2</sub> S .....	88



## LIST OF FIGURES

### CHAPTER 2

Figure 2-1	Basic operation of an SOFC .....	14
Figure 2-2	Specific ion conductivities of selected solid oxide electrolytes .....	21
Figure 2-3	Configurations of various SOFC modes .....	29

### CHAPTER 3

Figure 3-1	XPS spectrum of peak intensity as a function of binding energy for Ni/YSZ .....	55
Figure 3-2	Schematic of quartz sample tube and components for introduction into AutoChem II .....	60
Figure 3-3	BET spectrum for kaolin standard in 20% N <sub>2</sub> in Helium .....	62
Figure 3-4	Basic operation of mass spectrometer .....	65
Figure 3-5	Mass spectrum for blank run (Period B conditions) .....	67

### CHAPTER 4

Figure 4-1	Methane conversion at 800 °C (H <sub>2</sub> S-free environment) .....	74
Figure 4-2	Methane conversion at 700 °C (H <sub>2</sub> S-free environment) .....	74
Figure 4-3	Methane conversion at 600 °C (H <sub>2</sub> S-free environment) .....	75
Figure 4-4	Methane conversion at 500 °C (H <sub>2</sub> S-free environment) .....	75
Figure 4-5	Methane conversion at 800 °C (H <sub>2</sub> S environment) .....	77
Figure 4-6	Methane conversion at 700 °C (H <sub>2</sub> S environment) .....	77
Figure 4-7	Methane conversion at 600 °C (H <sub>2</sub> S environment) .....	78
Figure 4-8	Methane conversion at 500 °C (H <sub>2</sub> S environment) .....	78
Figure 4-9	Percent change in CO <sub>2</sub> selectivity between Period A and E for catalysts exposed without H <sub>2</sub> S .....	84
Figure 4-10	Percent change in CO <sub>2</sub> selectivity between Period A and E for catalysts exposed with H <sub>2</sub> S .....	84
Figure 4-11	Rate of methane disappearance as a function of methane partial pressure for Ni/YSZ (H <sub>2</sub> S-free) .....	89

Figure 4-12	Rate of methane disappearance as a function of methane partial pressure for Cu/YSZ (H <sub>2</sub> S-free) .....	89
Figure 4-13	Rate of methane disappearance as a function of methane partial pressure for Ni/Cu/YSZ (H <sub>2</sub> S-free) .....	90
Figure 4-14	Rate of methane disappearance as a function of methane partial pressure for LiCoO <sub>2</sub> (1)/YSZ (H <sub>2</sub> S-free) .....	90
Figure 4-15	Rate of methane disappearance as a function of methane partial pressure of methane for LiCoO <sub>2</sub> (1)/YSZ (H <sub>2</sub> S-free) .....	91
Figure 4-16	Rate of methane disappearance as a function of methane partial pressure for Ni/YSZ (H <sub>2</sub> S) .....	94
Figure 4-17	Rate of methane disappearance as a function of methane partial pressure for Cu/YSZ (H <sub>2</sub> S) .....	94
Figure 4-18	Rate of methane disappearance as a function of methane partial pressure for Ni/Cu/YSZ (H <sub>2</sub> S) .....	95
Figure 4-19	Rate of methane disappearance as a function of methane partial pressure for LiCoO <sub>2</sub> (1)/YSZ (H <sub>2</sub> S) .....	95
Figure 4-20	Rate of methane disappearance as a function of methane partial pressure for methane for LiCoO <sub>2</sub> (1)/YSZ (H <sub>2</sub> S) .....	96

## LIST OF EQUATIONS

### CHAPTER 1

Equation (1-1) – (1-3)	Summary of electrode reactions in a PEM fuel cell .....7
Equation (1-4) – (1-7)	Summary of electrode reaction in a SOFC .....8
Equation (1-8) – (1-9)	Partial oxidation of H <sub>2</sub> S in the Claus process .....10
Equation (1-10) – (1-13)	H <sub>2</sub> S oxidation reactions in an SOFC .....11

### CHAPTER 2

Equation (2-1) – (2-2)	Oxygen conducting electrolyte reactions .....18
Equation (2-3) – (2-4)	Hydrogen conducting electrolyte reactions .....18
Equation (2-5) – (2-8)	Reactions involved with steam reforming of methane ....27
Equation (2-9) – (2-10)	Energy balance for a fuel cell system (isothermal) .....31
Equation (2-11) – (2-12)	Thermal efficiency of a fuel cell .....32
Equation (2-13) – (2-14)	Electromotive force equations .....33
Equation (2-15) – (2-17)	Carbon deposition reactions .....35

### CHAPTER 3

Equation (3-1)	Kinetic energy of emitted photoelectrons .....54
Equation (3-2) – (3-3)	BET equations .....57
Equation (3-4)	Equation to determine volume at STP .....57
Equation (3-5)	Surface area equation .....58
Equation (3-6)	Complete methane oxidation reaction .....64

### CHAPTER 4

Equation (4-1) – (4-2)	Methane conversion equations .....72
Equation (4-3) – (4-4)	Partial methane oxidation reactions .....72
Equation (4-5)	CO <sub>2</sub> selectivity equation .....79
Equation (4-6)	CO <sub>2</sub> selectivity change between Period A and E .....83
Equation (4-7)	Power law combined with the Arrhenius equation .....85
Equation (4-8)	Rate of disappearance of methane equation .....85

CHAPTER 5

Equation (5-1) – (5-11)

Possible reactions based on the Langmuir-Hinshelwood  
model .....102

## NOMENCLATURE

A	Pre-exponential factor	
$A_{N_2}$	Area of a nitrogen molecule	(m <sup>2</sup> /molecule)
C	Concentration	(mol/m <sup>3</sup> )
dX	Change in conversion	
E	Electromotive force at temperature T	(V)
E°	Electromotive force at standard state	(V)
E <sub>a</sub>	Activation Energy	(J/mol)
E <sub>binding</sub>	Binding energy	
E <sub>kinetics</sub>	Kinetic energy	
F	Faraday's constant (F = 96,485)	(C/mol)
F	Molar flow rate	(mol/min)
ΔG	Change in Gibbs free energy	
ΔH	Difference in enthalpy of reaction	
h	Planck's constant (h = 6.626068 x 10 <sup>-34</sup> )	(m <sup>2</sup> kg/s)
K	Equilibrium constant	
k	Rate constant	
M	Mass of catalyst	(g)
n	Number of moles	
P	Pressure	(mm Hg)
Q	Heat transfer	
R	Gas Constant (8.314)	(J/mol·K)
(-r <sub>CH<sub>4</sub></sub> )	Rate of methane disappearance	(mol/ min g metal)

$\Delta S$	Change in entropy	
S	Selectivity	
SA	Surface area	(m <sup>2</sup> /g)
T	Temperature	(K)
T <sub>o</sub>	Ambient temperature	(K)
V	Volume	(m <sup>3</sup> )
W	Work done	
X	Conversion	
z	Number of electrons transferred per molecule of fuel converted	

### Subscripts

a	Ambient conditions
elec	Electric work
elec,rev	Reversible electric work
i	Inlet parameter
m	Monolayer
o	Outlet parameter
R	Reaction
max	Maximum reversible work

### Greek Letters

$\alpha$	Reaction order of methane
$\eta$	Thermal efficiency

$\nu$  Frequency of the exciting radiation

$\beta$  Reaction order of oxygen

$\Phi$  Work function

# Chapter 1

## Introduction

### 1.1 Introduction

The generation of energy by clean, efficient and environmental friendly means is one of the major challenges for engineers and scientists. For centuries, human impact such as clearing forests and burning coal, oil and gas, and emitting carbon dioxide and other heat trapping gases into the atmosphere faster than plants and oceans can absorb has caused disastrous effects on the environment and on human health. During the past century, global surface temperatures have increased at a rate near  $0.6\text{ }^{\circ}\text{C}$  per/century (National Oceanic and Atmospheric Administration, 2001). World emissions of carbon dioxide are expected to increase by 54% above 1990 levels by 2015, which, based on present trends, is expected to increase the average surface temperature  $1.7 - 4.9\text{ }^{\circ}\text{C}$  over the period 1990-2100 (National Center for Atmospheric Research, 2001).

Human activity most likely caused most of the past century's warming, a landmark report from the United Nations Intergovernmental Panel on Climate Change (IPCC) declared in 2001 (Appenzeller and Dimick, 2004). Problems with the energy supply are not only related to global warming but also to air pollution, acid rain precipitation, ozone depletion, forest destruction, and emission of radioactive substances. Energy exploitation of fossil fuels is reaching limits. World population is increasing at a rate of  $1.2 - 2\%$  per year (Stambouli and Traversa, 2002). Therefore, economic development will continue to grow. Global demand for energy services is expected to



increase by an order of magnitude by 2050, while primary energy demands are expected to increase by 1.5 to 3 times (Stambouli and Traversa, 2002). As the world's oil supply decreases, the development of new power generation technologies will become increasingly important. Some of the solutions that have evolved include energy conservation through improved energy efficiency, reduction in fossil fuel use, and an increase in the supply and use of renewable resources.

## **1.2 Fuel Cells**

### **1.2.1 Introduction to Fuel Cells**

Fuel cells have offered a realistic prospect of being commercially viable only in the last two decades due to their significant environmental benefits and high electrical efficiency (Omerod, 2003). Fuel cells have the ability to produce a large amount of power, and will be in high demand in the future as a possible sustainable energy resource. The combination of the high electrical efficiency and lower emissions of sulfur, nitrogen oxides, hydrocarbon pollutants and carbon dioxide due to the increased efficiency give fuel cells significant advantages over conventional power generation. Unfortunately, fuel cell technology is not presently commercially viable due to their high cost compared to conventional power generation systems. However, significant advances in the development of materials with improved properties and in manufacturing processes in the last two decades have made fuel cells a realistic proposition to compete on a commercial scale with conventional power generation systems (Omerod, 2003).

A fuel cell is a device that converts chemical energy directly into electricity and heat. They can be referred to as batteries which, when provided with fuel and air,

provide sustainable energy. In general, all fuel cells share the use of hydrogen as the fuel. The basic operating principle of all types of fuel cells is similar. In a typical fuel cell, gaseous fuels are fed continuously to the anode (negative electrode) and an oxidant is fed continuously to the cathode (positive electrode); the electrochemical reactions take place at the electrodes which produce an electric current. Depending on the type of electrolyte, either protons or oxide ions are transported through an ion conducting, electronically insulating electrolyte, while electrons travel in an external circuit delivering electric power. A more detailed description of solid oxide fuel cell (SOFC) operation is discussed in the following chapter.

### **1.2.2 Applications of Fuel cells**

Fuel cells have high reliability and low maintenance, and coupled with their quiet operation and modular nature, they are particularly suited to localized power generation networks and in small-scale and remote applications. Applications range from very small-scale systems requiring only a few watts to large-scale distributed power generation of hundreds of megawatts (Omerod, 2003). Fuel cells offer significantly higher power densities than batteries, as well as being smaller and lighter and having much longer lifetimes. This gives them the commercial viability towards applications, for example, laptop computers, mobile phones, portable electronic devices and computer systems. In addition, the combination of their high efficiency and significantly reduced emissions of pollutants makes fuel cell powered vehicles an attractive proposition, especially in heavy populated areas where pollution is a problem (Omerod, 2003). Low temperature fuel cells, in particular proton exchange membrane (PEM) fuel cells, are

most suited for transport applications because of the need for short warm-up and cool down times and because there are no problems with temperature cycling (Omerod, 2003). Hydrogen powered fuel cells in vehicles are also regarded as 'zero emission' vehicles; however, hydrogen gas is very expensive to produce and difficult to store. The other major disadvantage using hydrogen as a fuel is the emissions generated in producing hydrogen and the low energy density of hydrogen gas per unit volume (compared to liquid fuels). Therefore, hydrogen fuel cells are not economically viable or practically feasible. More likely, liquid fuels, such as methanol or hydrocarbon fuels will be used with onboard fuel processors to catalytically convert the fuel to produce hydrogen and carbon dioxide, or the fuel cell will directly oxidize the liquid fuels into water and carbon dioxide.

Solid oxide fuel cells (SOFCs) are particularly suited for combined heat and power (CHP) applications ranging from less than one kilowatt to several megawatts, which includes individual households, larger residential units, and business and industrial premises, to provide all the power and hot water from a single unit (Omerod, 2003). These types of CHP units have greater efficiency than conventional power stations supplied by boiler units and also have better reliability. In terms of large scale power generation systems (hundreds of megawatts), SOFCs can be integrated into existing systems where heat from the fuel cell is used to drive a gas turbine to produce more electricity and increase system efficiency to as high as 80% (Omerod, 2003). This is significantly higher than conventional electricity generation. Fuel cells are also ideal for small-scale and remote applications such as gas pipelines and farms. Of the several fuel cell producers, Siemens Westinghouse® deals with many applications regarding SOFCs.

They have developed a successful commercial prototype 150 cm cell, and a 100-kilowatt co-generation system that has operated in the Netherlands for more than two years and continues to operate successfully ([www.siemenswestinghouse.com](http://www.siemenswestinghouse.com)).

### **1.2.3 Types of Fuel Cells**

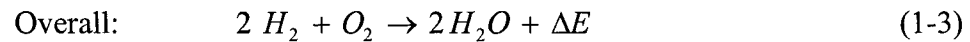
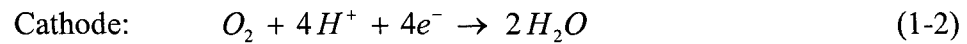
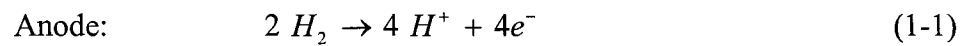
There are various types of fuel cells being used and researched, including alkaline fuel cells (AFC), phosphoric acid fuel cells (PAFC), polymer electrolyte membrane fuel cells (PEM), molten carbonate fuel cells (MCFC), and solid oxide fuel cells (SOFC). The types of fuel cells are classified by the nature of the electrolyte used as the ionic conductor in the cell and are summarized in Table 1 (Stambouli and Traversa, 2002).

Alkaline fuel cells use an aqueous solution of either sodium or potassium hydroxide as the electrolyte, with hydrogen as the fuel and air or pure oxygen as the oxidant and have an operating temperatures at around 70 °C. The electrodes are made from carbon with a platinum electrocatalyst (Omerod, 2003). AFCs are the oldest fuel cell that requires a source of pure hydrogen as the fuel. Pure hydrogen must be used or the fuel cell will become poisoned by both carbon monoxide and carbon dioxide (Omerod, 2003). Phosphoric acid fuel cells use a phosphoric acid electrolyte and operate on hydrogen fuel with air or pure oxygen as the oxidant, and have an operating temperature of 200 °C. Unlike AFCs, PAFCs are able to operate using hydrogen contaminated with carbon dioxide, which places less stringent demands on the external fuel processor (Omerod, 2003). The polymer electrolyte membrane fuel cell, also known as the proton conducting membrane or solid polymer fuel cell, uses a proton conducting polymer membrane as the electrolyte and requires hydrogen as the fuel and oxygen as the

Table 1-1. Technical characteristics of various types of fuel cells (Adapted by Stambouli and Traversa, 2002).

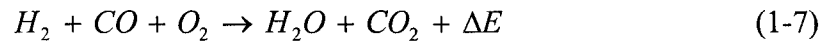
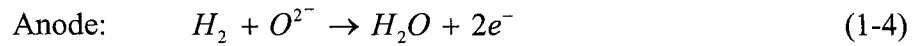
Types of Fuel Cells	Electrolyte	Operating T	Fuel	Oxidant	Efficiency
Alkaline (AFC)	Potassium hydroxide	50 - 200 °C	Pure hydrogen or hydrazine	O <sub>2</sub> /Air	50 – 55%
Direct Methanol (DMFC)	polymer	60 – 200 °C	Liquid methanol	O <sub>2</sub> /Air	40 – 55%
Phosphoric acid (PAFC)	Phosphoric acid	160 – 120 °C	Hydrogen from hydrocarbons and alcohol	O <sub>2</sub> /Air	40 – 50%
Sulfuric acid (SAFC)	Sulfuric acid	80 – 90 °C	Alcohol or impure hydrogen	O <sub>2</sub> /Air	40 – 50%
Proton-exchange membrane (PEMFC)	Polymer, proton exchange membrane	50 – 80 °C	Less pure hydrogen from hydrocarbons or methanol	O <sub>2</sub> /Air	40 – 50%
Molten carbonate (MCFC)	Molten salt such as nitrate, sulfate, carbonates...	630 – 650 °C	Hydrogen, CO, natural gas, propane, marine diesel	CO <sub>2</sub> /O <sub>2</sub> /Air	50 – 60%
Solid Oxide (SOFC)	Ceramic as stabilised zirconia and doped perovskite	600 – 1000 °C	Natural gas or propane	O <sub>2</sub> /Air	45 – 60%
Protonic ceramic (PCFC)	Thin membrane of barium cerium oxide	600 – 700 °C	hydrocarbons	O <sub>2</sub> /Air	45 – 60%

oxidant. The operating temperature is about 80 °C. Similar to AFCs, the electrodes are made from carbon with a platinum electrocatalyst (Omerod, 2003). PEM fuel cells are also poisoned with carbon monoxide, which results in a complex and expensive fuel processor to convert practical hydrocarbon fuels into hydrogen and carbon dioxide removing all traces of carbon monoxide (Omerod, 2003). A summary of electrode reactions and the overall cell reaction for PEMs is shown below (Omerod, 2003):



Molten carbonate fuel cells have a molten potassium lithium carbonate electrolyte, which requires an operating temperature of 650 °C. They operate on a mixture of hydrogen and carbon monoxide, which is formed by internally reforming practical hydrocarbon fuels within the fuel cell. Solid oxide fuel cells, which is the topic of this research, use a solid ceramic inorganic oxide as the electrolyte, typically yttria-stabilized zirconia (YSZ), as opposed to a liquid electrolyte. Operating temperatures are usually between 750 – 1000 °C. Similar to MCFCs, SOFCs usually operate on a mixture of hydrogen and carbon monoxide formed by internally reforming practical hydrocarbon fuels within the fuel cell. The products formed are water and carbon dioxide.

A summary of the reactions in a SOFC are shown below (Omerod, 2003):



Characterization of each type of fuel cell is by the electrolyte and also by the operating temperature, as described above. In general, the most interest and research in fuel cell technology is currently on PEMs and SOFCs.

#### 1.2.4 Solid Oxide Fuel Cell Operation and Benefits

SOFCs have recently emerged as a practical high temperature fuel cell technology. SOFCs consist of a solid ceramic as the electrolyte and operate at high temperatures (600 – 1000 °C). The high operating temperatures allow for internal reforming, promote rapid electrocatalysis with non-precious metals, and produce high quality byproduct heat for co-generation (Mcintosh and Gorte, 2004). Efficiencies can reach up to 70% with an additional 20% as heat recovery (Stambouli and Traversa, 2002). Advantages of SOFCs over other types of fuel cells are listed below (Stambouli and Traversa, 2002):

- The most efficient (fuel input to electricity output) fuel cell electricity generators currently being developed world-wide.

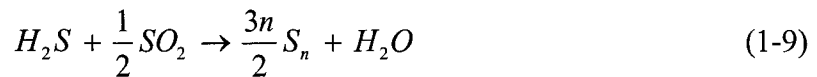
- They are flexible in the choice of fuel such as carbon-based fuels including natural gas.
- SOFC technology is ideally suited for applications in the distributed generation (i.e., stationary power) market because of the high conversion efficiency.
- SOFCs have a modular and solid-state construction and do not contain any moving parts, thereby are quiet enough to be installed indoors.
- The high operating temperatures allow SOFCs to produce high quality heat byproducts, which can be used for co-generation or for use in combined cycle applications.
- SOFCs do not contain noble metals that could be problematic in resource availability and cost in high volume manufacturing.
- SOFCs do not have problems with electrolyte management.
- SOFCs have extremely low emissions by eliminating the danger of carbon monoxide in exhaust gases, as any CO produced is converted to carbon dioxide at the high operating temperatures.

In addition to the above advantages, SOFCs produce much lower emissions than current conventional power systems. The high efficiency of SOFCs results in less fuel being consumed to produce a given amount of electricity, which corresponds to a lower emission of carbon dioxide (primary greenhouse gas), allowing for a potential reduction of carbon dioxide emissions by more than two million kg per year (Stambouli and Traversa, 2002). Moreover, emissions from SOFC systems produce almost no  $\text{NO}_x$ ,  $\text{SO}_x$  and particulates, therefore eliminating 20,000 kg of acid rain and smog-causing pollutants from the environment (Stambouli and Traversa, 2002).



### 1.3 Fuel Cells and Hydrogen Sulfide Containing Fuels

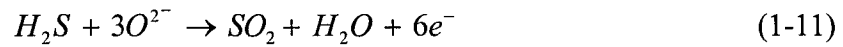
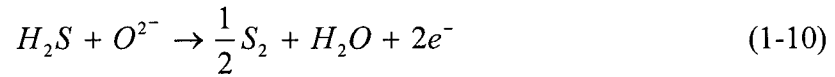
The United States alone produces over 12 million tons of hydrogen sulfide, mainly as an industrial by-product in the refining of fossil fuels (Aguilar et al., 2004). The lack of a commercial use for hydrogen sulfide results in virtually all of it being converted to sulfur using the Claus Process, where partial oxidation with air produces elementary sulfur and water (Aguilar et al, 2004). This process is shown by Equations (1-8) and (1-9) (Aguilar et al., 2004).



Equation (1-8) is a non-catalytic combustion process usually carried out at around 1100 °C, whereas Equation (1-9) is a reversible catalytic process carried out using an equilibrium reactor train. It is possible to recover the low-grade thermal energy from the Claus Process, but it is more advantageous to electrochemically oxidize hydrogen sulfide in a fuel cell. This results in a direct conversion of the overall reaction free energy into electricity, which can reach up to 80% efficiencies for integrated systems (Aguilar et al., 2004). In addition, fuel cells using hydrogen sulfide fuels produce sulfur dioxide, which can be used in the manufacture of sulfuric acid and sodium hydroxide.

The ability for SOFCs to operate on hydrogen sulfide containing fuels provides a tremendous potential to enter the energy market and take advantage of the current energy delivery infrastructure. Approximately 10 ppm of sulfur containing compounds is added

to natural gas as an odorant (Aguilar et al., 2004), and gasoline regulations in most of the U.S. allow 300 ppm of sulfur (Hyuk et al., 2001). However, the common Ni/YSZ anode can only tolerate H<sub>2</sub>S levels less than 5 ppmw at 800 °C (Aguilar et al., 2004). Because most hydrocarbon fuels contain significant levels of sulfur, SOFCs must be able to operate with fuels containing sulfur, particularly H<sub>2</sub>S, to be practically viable. There are several possible reactions for the oxidation of H<sub>2</sub>S in a SOFC illustrated by Equations (1-10) to (1-13). The two main electrochemical processes at the anode are shown by Equations (1-10) and (1-11) (Aguilar et al., 2004).



In order to produce a viable H<sub>2</sub>S tolerant SOFC, the anode material must be conductive, chemically and electrochemically stable, and catalytically active in an H<sub>2</sub>S rich environment. This may be problematic in some cases due to the corrosive nature of H<sub>2</sub>S. The poor performance of traditional metallic anodes with H<sub>2</sub>S containing fuels has led to the investigation of composite oxides and sulfides as potential electrode materials due to their increased stability and desirable electrical properties (Aguilar et al., 2004).

## 1.4 Research Objectives

The main purpose of this research is focused on the analysis of potential sulfur resistant anode materials for the application in a hydrogen sulfide compatible solid oxide fuel cell. Sulfur resistant anodes in solid oxide fuel cells will become very useful and result in the ability to use virtually all fuels, since hydrogen sulfide is one of the main impurities in fuels. Even at low levels of hydrogen sulfide (<10ppm), degradation of fuel cell performance becomes a problem due to its corrosive nature. Currently, processing of the fuel is required to reduce levels of hydrogen sulfide below 5 ppm. As an alternative to the additional processing, this research will examine different anode materials and determine their ability to resist degradation due to hydrogen sulfide. The primary objective will be to understand the reactivity and kinetics using various catalysts of methane oxidation in the presence of hydrogen sulfide.

The following chapter discusses the literature review describing the operation, thermodynamics and components of SOFCs. In addition, previous work on different types of SOFC anodes and the progress in obtaining an alternative hydrogen sulfide resistant anode for SOFC applications will also be discussed. The subsequent chapters will describe the experimental methods, results, discussion, and concluding remarks.

## Chapter 2

### Literature Review

#### 2.1 General Introduction to Solid Oxide Fuel Cells

Solid oxide fuel cells (SOFCs) are energy conversion units that produce electrical energy and heat with greater energy efficiency and lower pollutant emission than conventional heat engines, steam and gas turbines, and combined cycles (Omerod, 2003). The basic components of the fuel cell consist of a cathode, anode and the electrolyte. SOFCs are characterized as having a solid ceramic electrolyte, which is a metallic oxide that conducts oxygen anions ( $O^{2-}$ ) and are also electronic insulators. Figure 2-1 shows a schematic diagram of the basic operation of an SOFC ([www.seca.doe.gov](http://www.seca.doe.gov)). On the cathode, molecular oxygen diffuses to the surface of the electrocatalyst, adsorbs on the surface and dissociates to oxygen atoms on the adsorption site. The atoms then diffuse to the reaction sites, where they combine with oxygen vacancies and electrons to form oxygen ions. The oxygen ions are then transferred to the ionic conducting electrolyte, and subsequently diffuse through the electrolyte to the anode under the influence of a gradient in electrochemical potential. At the anode, the oxygen ions react with the fuel to form water (and carbon dioxide) releasing electrons, which generate power while traveling to the cathode through an external circuit leading to the reduction of oxygen (Xia et al., 2004).

SOFC operating temperatures are usually between 800 – 1000 °C, although there is considerable interest in lowering the operating temperature of smaller SOFCs, in

## Solid Oxide Fuel cell

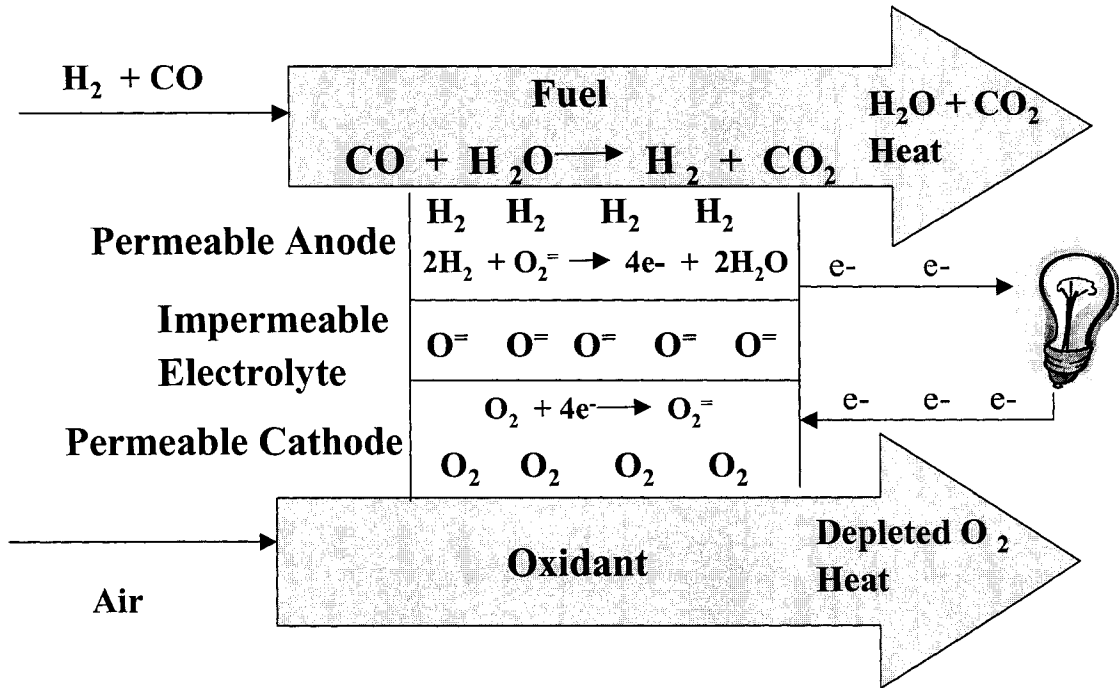


Figure 2-1. Basic Operation of an SOFC (adapted <http://www.seca.doe.gov>).

particular, to reduce costs (Ormerod, 2003). High temperature operation can cause serious problems, such as internal mechanical stress due to the difference in thermal expansion coefficients of the materials and chemical reactions (Hatae et al., 2004). However, the low operating temperatures can lead to large voltage losses due to the ohmic resistance of the materials and the polarization at the electrodes (Hatae et al., 2004). The high operating temperatures also allow the fuel cell to operate on hydrocarbon fuels without the need for a complex and expensive external fuel reformer, such as that required for a PEM fuel cell. The hydrocarbon fuel is catalytically converted or internally reformed to carbon monoxide and hydrogen within the SOFC, and the carbon monoxide and hydrogen are then electrochemically oxidized to carbon dioxide and water at the anode. The elevated operating temperatures also allow for the production of high temperature heat as a by-product in addition to the electrical power. This additional heat can be used to power other systems to produce more electricity.

SOFCs are the practical and economical choice of fuel cell technology due to their flexibility in the choice of fuel, the ability to operate directly on available hydrocarbon fuels, and their higher overall efficiency compared to other types of fuel cells. The other major advantage is their tolerance to carbon monoxide, which is electrochemically oxidized to carbon dioxide at the anode. This contrasts markedly with PEM fuel cells, which are highly susceptible to poisoning by carbon monoxide (Ormerod, 2003). Thus, PEM fuel cells require more complex and expensive external processing of hydrocarbon feeds to convert all the carbon monoxide to carbon dioxide. SOFCs also have greater tolerance to impurities in the fuel that poison other fuel cells. Additional benefits include the fact that they do not contain any precious metals which add

significantly to the cost of the fuel cell, and that the absence of any liquids in the cell eliminates potential problems due to corrosion and loss of electrolyte (Ormerod, 2003). While SOFCs have many advantages over other fuel cell types, they also have several disadvantages. One of the disadvantages for certain applications is the length of time that is generally required to heat up and cool down the system. This is a consequence of the need to use a relatively weak, brittle component as the substrate material and because of the problems associated with thermal expansion mismatches. In turn, this restricts the use of SOFCs in applications that require rapid temperature fluctuations, which is particularly true for transport applications where rapid start-up and cool down is essential (Ormerod, 2003).

## **2.2 Components and Materials of SOFCs**

SOFCs have specific requirements for the materials used as the anode, cathode, electrolyte, and interconnect. Each component has more than one primary function and must meet certain requirements. Some of the characteristics that these components must possess are chemical and physical stability in the appropriate chemical environment, be chemically compatible with the other components of the system, and have similar thermal expansion coefficients to the other components to avoid cracking or delamination during fabrication and operation (Ormerod, 2003). In addition, SOFC components must be affordable and strong, yet easy to fabricate. Currently, the most widely used components of an SOFC consist of a yttria-stabilized zirconia (YSZ) electrolyte, strontium-doped lanthanum manganite ( $\text{La}_{1-x}\text{Sr}_x\text{MnO}_3$ ) cathode, mixed nickel yttria-stabilized zirconia (Ni-

YSZ) cermet anode, and a doped lanthanum chromite ( $\text{LaCrO}_3$ ) interconnect (Ormerod, 2003).

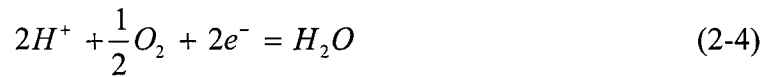
### 2.2.1 Solid Electrolytes

The electrolyte is probably the most crucial component of the SOFC. It must be dense to separate the fuel and air compartments of the cell, and retain it high ion conductivity and low electronic conductivity over a very wide range of oxygen partial pressures. In the 1960s, much of the research on SOFCs was focused on optimizing the ionic conductivity of the solid electrolyte (Ormerod, 2003). For example, the use of ytterbium oxide gave higher ionic conductivities but was unfortunately extremely expensive. The most common electrolyte used today is yttria-stabilized zirconia (usually around 8 mol% yttria) because it has good oxygen ion conductivity, is quite stable in both reducing and oxidizing environments, and is not reactive towards the other SOFC components. It is also abundant, relatively low in cost and is strong while being easy to fabricate. The conductivity of solid electrolytes is usually less than that for liquid electrolytes. The conductivity for YSZ is about 0.02 S/cm at 800 °C and 0.1 S/cm at 1000 °C, which makes it necessary to operate at high temperatures. Thus, research was needed to establish technology for fabricating and handling thin plates of electrolyte to decrease its ohmic loss (Yokokawa et al., 2001).

There are two main types of solid electrolytes, which are used in SOFCs. These include oxygen and hydrogen conducting electrolytes. The reactions involved in the oxygen conducting electrolytes are summarized in Equations (2-1) and (2-2) and the



hydrogen conducting electrolytes are shown in Equations (2-3) and (2-4) at the anode and cathode, respectively (Sangtongkitcharoen et al., 2005).



The difference between electrolyte types is the location of the water produced. Water is produced in the reaction mixture in the anode chamber for the oxygen-conducting electrolyte, while in the case of the hydrogen-conducting electrolyte water is produced on the cathode.

Pure  $ZrO_2$  is monoclinic at room temperature and undergoes phase transitions to a tetragonal structure above 1170 °C, and to the cubic structure above 2370 °C (Ormerod, 2003). Ytria, along with some other aliovalent oxides ( $Sc_2O_3$ , CaO, MgO and various rare-earth oxides), show a high solubility in  $ZrO_2$  and stabilize the zirconia in the cubic fluorite structure from room temperature to its melting point of 2680 °C, while concurrently increasing the concentration of oxygen ion vacancies which results in a dramatic increase in ionic conductivity. It has been shown that the ionic conductivity is at a maximum near the minimum level of dopant oxide required to fully stabilize the cubic phase (Ormerod, 2003). At higher dopant levels, the ionic conductivity decreases, due to defect ordering, vacancy clustering, and/or electrostatic interaction. Although

some other oxide dopants produce stabilized zirconia with higher ionic conductivity than yttria-stabilized zirconia, yttria is used because of its low cost, availability, high stability and its chemical inertness with other components. In addition, YSZ is non-porous to prevent mixing of the fuel and oxidant gas feeds (Ormerod, 2003).

The synthesis of zirconia powders has advanced and allowed the production of YSZ in the form of small, sub-micron, spherical particles with a narrow particle size distribution. These particle characteristics result in higher reactivity and high packing density, enabling the complete densification of the powders at low sintering temperatures (Minh, 1993). The low sintering temperatures are needed in order to enable electrolyte layers to be prepared which can withstand more rapid temperature fluctuations (Minh, 1993). Conventional zirconia used in SOFCs is generally used at an operating temperature greater than 850 °C. High operating temperatures also place severe demands on the materials used in the interconnect, and for manifolding and sealing which necessitates the use of expensive ceramic materials and specialist metal alloys. Therefore, there is currently interest in lowering the operating temperature of SOFCs (less than 700 °C) to enable the use of cheaper materials, such as stainless steel, and also reduce fabrication costs while maintaining efficiency and high power outputs.

The operating temperature is mainly governed by the properties of the electrolyte. Some of these properties include ionic conductivities and the thickness of the electrolyte layer. Therefore, the two possible solutions in lowering the operating temperature are either to reduce the thickness of the YSZ electrolyte layer or identify an alternative electrolyte material that exhibits higher oxygen ion conductivities. Currently, the thickness limit dense impermeable electrolyte films that can be reliably produced using

conventional fabrication routes is approximately 10-15 microns (Ormerod, 2003). The identification of alternative solid electrolyte materials has been active and is still the subject of intense research. Currently, the best alternative electrolytes to yttria-stabilized zirconia are gadolinia-doped ceria (Mogensen et al., 2000) and lanthanum gallate based structures (Steele and Heinzel, 2001). These alternative electrolytes can possibly lower the operating temperature of SOFCs to temperatures as low as 500 °C to 700 °C (Ormerod, 2003). Figure 2-2 shows the specific ionic conductivities of selected solid oxide electrolytes.

Gadolinia-doped ceria (CGO) offers excellent promise as a potential electrolyte for low temperature SOFCs. Unfortunately, at elevated temperatures in a reducing atmosphere, ceria undergoes partial reduction to  $Ce^{3+}$ , which leads to electronic conductivity resulting in lower efficiency of the fuel cell. There has been considerable research in trying to minimize the electronic conductivity of doped ceria under reducing conditions. If the operating temperature of the SOFC is low (~500 °C) then any electronic conductivity is small enough that it can be neglected (Ormerod, 2003). The main problem operating at such low temperatures is the development of sufficiently active cathode materials, which will be discussed in the next section.

Lanthanum gallate ( $LaGaO_3$ ) has also been studied as an alternative electrolyte for low temperature SOFCs (Steele and Heinzel, 2001).  $LaGaO_3$  has higher ionic conductivity because it substitutes both the trivalent lanthanum and gallium with divalent cations, which are generally strontium and magnesium (LSGM) (Ormerod, 2003). The ionic conductivity of LSGM is significantly higher than YSZ and is slightly less than that

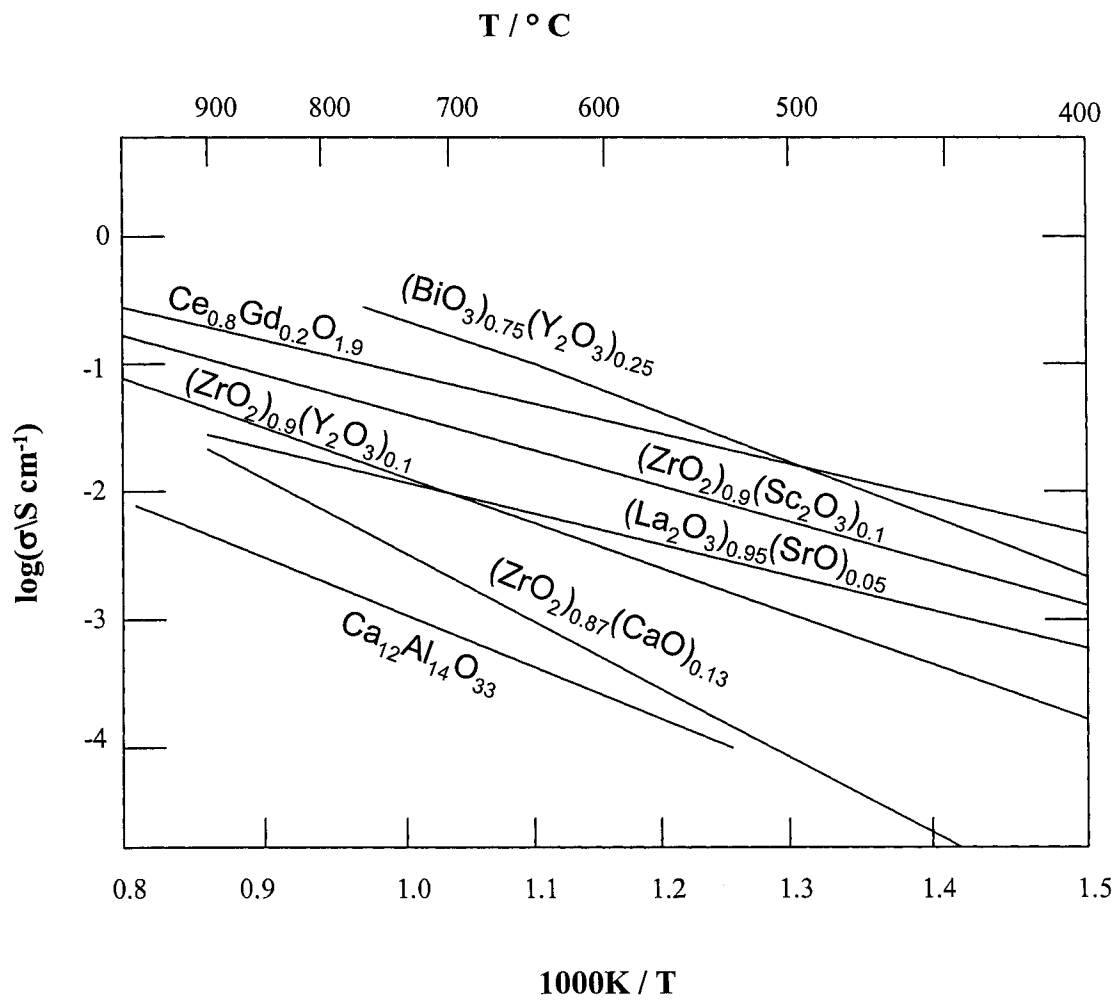


Figure 2-2. Specific ion conductivities of selected solid oxide electrolytes (adapted from Omerod, 2003).

of CGO at 500°C (Steele and Heinzl, 2001). However, the potential range of operating temperatures for LSGM is greater than CGO because it does not suffer from the problems of electronic conductivity exhibited by CGO at higher temperatures. Thus, LSGM could be used in SOFCs at operating temperatures of 500 – 700 °C, which are too low to obtain adequate power densities with zirconia based SOFCs. Unfortunately, there have been problems with the use of LSGM associated with the stability of certain compositions within the material. It has been proven difficult to prepare pure single-phase electrolytes of LSGM, and additional non-conductive phases such as  $\text{La}_4\text{Ga}_2\text{O}_9$  and  $\text{SrLaGa}_3\text{O}_7$  were detected at the grain boundaries (Steele and Heinzl, 2001). These points raise doubts about the long-term durability of LSGM in SOFCs, and additional research in LSGM is still required.

### **2.2.2 Anodes**

Alternative anode materials have been intensely researched in order to improve the performance and stability of the SOFC. The fuel fed to the anode is generally reducing in nature; thus, metals can be used as the anode material. However, the metal must not be oxidized under the operating conditions of the SOFC (Ormerod, 2003). Since the SOFC usually operates under high temperature conditions, the selection of a metal anode material is limited. The high operating temperatures of SOFCs prohibit the use of low melting metals. The anode material must contain large amounts of metal to be electronically conductive. Precious metals, with the exception of silver, are impractical from an economical standpoint (Gorte et al., 2000). The most common anode material used is nickel because of its low cost compared to precious metals. Although cobalt and

ruthenium offer potential advantages over nickel, including sulfur tolerance, and in the case of ruthenium higher reforming activity and greater resistance to sintering, the cost of these materials effectively precludes their use (Ormerod, 2003).

Nickel has been the most suitable anode metal for first generation SOFCs. Unfortunately, many issues associated with anodes originate from cermet Ni/YSZ anodes. The anode must have a porous structure, which furthermore must be maintained at the high operating temperatures. This is partly achieved by dispersing the nickel with the solid electrolyte material to form the cermet, which maintains the porosity by preventing sintering of the nickel particles during operation and also gives the anode a thermal expansion coefficient comparable to that of the electrolyte (Ormerod, 2003). Since the operational temperature of SOFCs is high (higher than two thirds of the melting temperature of nickel), it is difficult to prevent bulk diffusion of nickel (Minh, 1993). The thermal expansion coefficient of nickel is appreciably different from that of yttria-stabilized zirconia, and thus adhesion of a pure nickel anode to the electrolyte would be a major problem during fabrication and firing, and temperature cycling during operation (Minh, 1993). In this case, nickel particles sinter during operation, resulting in coarsening of particles and breaking of the electrical path and finally, the degradation of the anode activity (Yokokawa et al., 2001). One of the most impressive achievements for the improvement of SOFC anodes is addition of ceria ( $\text{CeO}_2$ ) to a Ni/YSZ cermet. This results in the anode being tolerant to heat and atmospheric cycling without degradation (Yokokawa et al., 2001).

The anode must also be electrically conducting to function as an electrode. The electronic conductivity of the anode depends on its microstructure, in particular the size

and particle size distribution of the electrolyte and the metal particles, and also the connectivity of the metal particles in the cermet. For example, the electronic conductivity of the nickel/solid electrolyte cermet depends on the nickel content. The threshold for good electrical conductivity is about thirty volume percent nickel; below this value the electronic conductivity of the cermet is effectively that of the solid electrolyte. Above this threshold value, the electronic conductivity increases about three orders of magnitude (Ormerod, 2003). The proportion of nickel used is also related to the thermal expansion mismatch with the solid electrolyte. The thermal expansion mismatch of a Ni/YSZ cermet increases linearly with the nickel content and thus, the higher the nickel content of the anode the greater the thermal mismatch with the electrolyte (Ormerod, 2003). This will eventually result in a greater mismatch and more chance there will be cracking of the electrolyte or delamination of the anode during the fabrication process and/or in operation during temperature cycling (Minh, 1993).

Considerable research has been associated in mitigating these types of problems. Such improvements involve minimizing any processing flaws in the electrolyte, improving its fracture toughness, using graded anodes of different compositions and altering the thickness of the electrolyte and anode layers (Majumdar et al., 1986). Another approach is to incorporate small quantities of a third material into the anode in an attempt to match the thermal expansion coefficient with that of the electrolyte (Ormerod, 2003). There is currently much interest in developing alternative anode materials.

The anode performance is also affected by the reactivity in the triple phase boundary (TPB) region. The TPB is the region where the reactions occur where the gas

phase, ionic conductor, and the electronic conductor come together. The TPB occurs in the first 10  $\mu\text{m}$  near the electrolyte and is affected strongly by the composition and structure of this region (Gorte et al., 2000). For example, the performance of the SOFC can be enhanced by introducing doped ceria, which is an excellent mixed conductor in the TPB (Gorte et al., 2000).

### **2.2.3 Cathodes**

The cathode must be stable in an oxidizing atmosphere and, similar to the anode, it must exhibit good electronic conductivity and have a porous structure which must be maintained at the high operating temperatures (Omerod, 2003). Ionic conductivity is also desirable for extending the reaction zone well into the electrode since the ions must ultimately be transferred to the electrolyte (McIntosh and Gorte, 2004). Unfortunately, the high operating temperature of SOFCs limits the choice of cathode material to noble metals or oxides that have sufficiently high electronic conductivity. Since noble metals are precluded due to their high cost, metal oxides are commonly used. In most cases, the cathode is a composite of an electronically conductive ceramic and an ionically conductive oxide, which often exhibits similar properties as the electrolyte (McIntosh and Gorte, 2004). The reduction of oxygen at the cathode takes place only in the vicinity of the TPBs between an electronic conductor, an ionic conductor, and oxygen gas. The required simultaneous transport of oxygen ions and electrons implies that a mixed conductor, a material conductive to both oxygen ions and electrons, would make a better cathode than a pure electronic conductor (Xia et al., 2004). The cathode material must also have a thermal expansion coefficient comparable to that of the solid electrolyte and



not show any tendency to react with the electrolyte (Ormerod, 2003). Strontium-doped lanthanum manganite (LSM) is the most commonly used cathode material for zirconia based SOFCs because of its high thermal and chemical stability (Ormerod, 2003).

Lanthanum manganite ( $\text{LaMnO}_3$ ) is a perovskite material with intrinsic p-type conductivity, the oxygen stoichiometry of which at high temperature is a function of the oxygen partial pressure having an oxygen excess in an oxidizing environment, while becoming oxygen deficient in a reducing environment (Ormerod, 2003). It is important that significant changes in the oxygen stoichiometry are avoided. While LSM has shown promising performance operating at temperatures above 800 °C, its performance decreases rapidly as the operating temperature decreases (Xia et al., 2004). Therefore, there has been research in improving LSM to operate at lower temperatures, such as the use of dual phase cathodes or by improvements in the cathode microstructure (Xia et al., 2004). Other cathode materials used include LSC (strontium-doped lanthanum cobaltite) and LSF (strontium-doped lanthanum ferrite) (Foger and Ahmed, 2005).

### **2.3 Reforming of Hydrocarbons in SOFCs**

One of the main advantages of SOFCs is their ability to reform hydrocarbon fuels within the actual fuel cell to produce hydrogen and carbon monoxide, which then can be used to produce electricity and heat. Researchers have investigated several different methods of reforming within the fuel cell. The direct electrochemical oxidation of hydrocarbon fuel, such as methane, is not yet a practical option (Gardner, 1997). Several chemical reaction pathways, competing with electrochemical oxidation, occur more readily. Problems encountered consist of carbon deposition, which results in a dramatic

decrease in performance in the fuel cell. One of the methods used to address this problem is steam reforming to prevent carbon formation. For example, steam reforming methane results in the chemical reaction illustrated by Equation (2-5) (Marina and Mogensen, 1999):



This is followed by an electrochemical oxidation of hydrogen at the same anode shown by Equation (2-6) and the conversion of CO can further proceed by electrochemical oxidation by Equation (2-7) or by the water-gas shift reaction in Equation (2-8) (Marina and Mogensen, 1999).

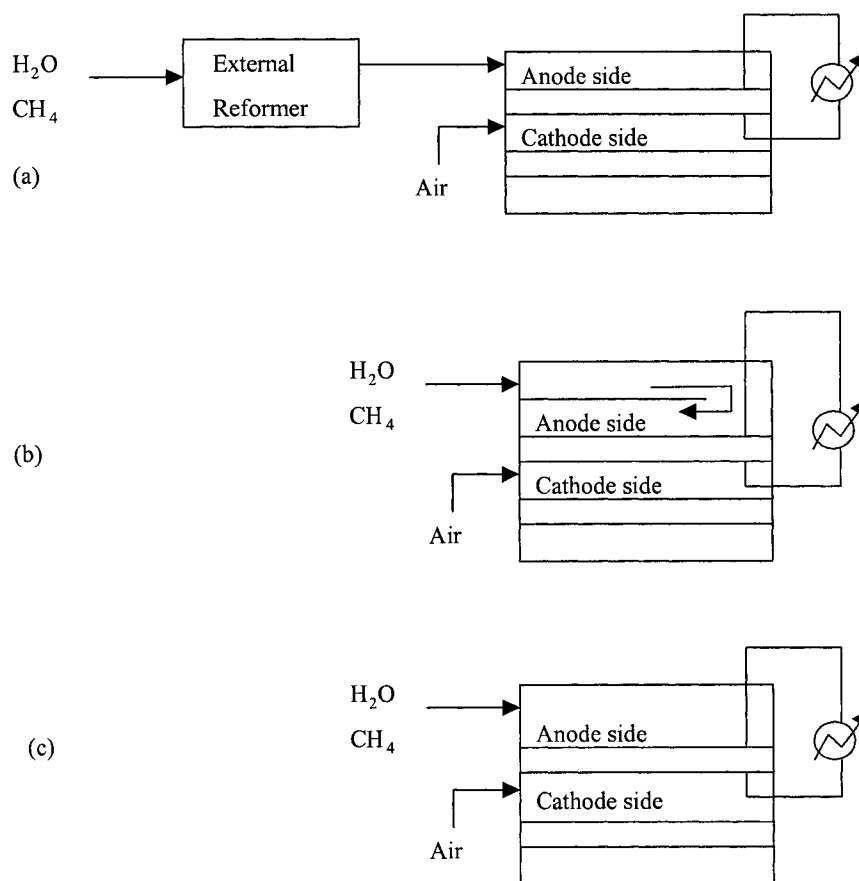


The ideal temperature for the steam reforming process is carried out at temperatures above 600 – 700 °C. The steam to methane ratio commonly used is 3:1 to suppress carbon formation in the fuel cell (Gardner, 1997). Unfortunately, excess steam further degrades the electrochemical work potential of the fuel cell (Mogensen and Krammer, 2003). Furthermore, hydrocarbon steam reforming is considered a strong endothermic reaction that can give rise to potential instabilities in the coupling between the slow exothermic fuel cell reactions and the rapid endothermic reforming reaction (Omerod,

2003). In certain applications, especially in small-scale devices, oxygen or air is used as the oxidant rather than steam because of the cost and complexity associated with using large quantities of steam, which makes its use less favorable in small-scale systems (Omerod, 2003). However, this could lead to an inherent efficiency loss due to the large energy loss in oxidizing the hydrocarbon fuel.

There are three different reforming techniques that are used in reforming fuel into useful hydrogen. These include external reforming, indirect internal reforming and direct internal reforming. Figure (2-3) illustrates the three different modes of reforming (Sangtongkitcharoen et al., 2005). External reforming consists of endothermic reforming and electrochemical reactions to be operated separately in different units and there is no direct heat transfer between both units. This requires a high energy supply to the reformer. In contrast, indirect and direct internal reforming includes endothermic reactions from the steam reforming reaction and the exothermic reaction from the oxidation reaction to be operated as a single unit. Therefore, there is no need for a separate fuel reformer, and energy supply to this unit is eliminated. Thus, this makes internal reforming a much more attractive and efficient means of producing electrical power in SOFCs. For indirect internal reforming, the reforming reaction occurs in the cell stack. This allows for heat transfer from the fuel cell chamber to the reformer, which leads to efficient energy production. However, a portion of the heat may not be efficiently utilized due to its limited heat transfer rate. On the other hand, direct internal reforming requires the reforming reaction to take place at the anode of the fuel cell. Heat and steam released from the electrochemical reaction upon power generation is effectively used for the endothermic reforming reaction since both processes take place

simultaneously at the anode (Sangtongkitcharoen et al., 2005). This makes direct internal reforming the best viable option and provides the greatest system efficiency with the least loss of energy in SOFC operation.



Configurations of various SOFC modes. (a) ER-SOFC, (b) IIR-SOFC and (c) DIR-SOFC.

Figure 2-3. Configurations of Various SOFC Modes (Adapted by Sangtongkitcharoen et al., 2005).

## 2.4 Thermodynamics of Fuel Cells

The main difference between fuel cell (electrochemical systems) and heat engine (combustion engine) efficiencies is a fundamental one with regard to the conversion of chemical energy reactions into electrical work. Both systems are still constrained by the second law of thermodynamics. However, this statement does not mean the two systems produce the same thermal efficiency when fed the same amount of chemical reactants. Conventional power systems are based on an ideal heat engine cycle. The work extracted from the heating value of fuel is less than the Carnot efficiency (Gardner, 1997). On the other hand, fuel cells are non-heat engine energy conversion technologies which are not limited by the Carnot efficiency. Ideally, they convert the change in Gibbs free energy in fuel oxidation directly into electricity, which results in a very high fraction of the heating value of a hydrocarbon fuel, such as natural gas. Compared to conventional fossil fueled power plants, the fuel is oxidized in a substantial adiabatic combustion process. This converts the change in Gibbs free energy into thermal energy (entropy), rather than into electrical work directly. In a fuel cell, the fuel is oxidized in an isothermal process with minimal entropy production and maximum work production (Gardner, 1997).

The combustion of fuel is based on the heating value of the fuel, which is the amount of heat released when a specific amount of fuel at room temperature is completely burned and the combustion products are cooled to room temperature. Therefore, the combustion efficiency can be defined as the ratio of the amount of heat released during combustion over the heating value of the fuel burned (Cengel and Boles, 1998). Most fuels contain hydrogen, which produces water when burned. This will give a different heating value depending if the product is in vapor or liquid form. The heating

value is usually classified as the lower heating value (LHV) or the higher heating value (HHV). The difference between the two values is that the water either leaves as vapor (LHV) or in liquid form (HHV). In other words, the difference between the two values is equal to the product of the amount of water and the enthalpy of vaporization of water at room temperature (Cengel and Boles, 1998).

Assuming an isothermal process, an energy balance for a fuel cell system is illustrated by Equation (2-9) (Hassazadeh and Mansouri, 2005).

$$Q - W_{elec} = \Delta H_R \quad (2-9)$$

where,  $\Delta H_R$  is the difference between molar enthalpies of products and reactants (fuel and oxidizer),  $Q$  is the heat transfer and  $W_{elec}$  is the work done. With the assumption of an isothermal system, it may require that heat be removed or added to the system. In this case, Equation (2-10) is assumed; that is, the heat transfer to or from the system is assumed reversible (Hassazadeh and Mansouri, 2005).

$$W_{elec,rev} = -\Delta H_R + Q = -\Delta H_R + T\Delta S_R = -\Delta G_R(T, P) \quad (2-10)$$

where,  $S_R$  is the entropy of reaction and  $G_R$  is the Gibbs free energy of reaction. Hence, the maximum work is the difference between the entering and leaving values of the Gibbs energy for the fuel cell system (Hassazadeh and Mansouri, 2005). The thermal energy of an ideal fuel cell is represented by Equation (2-11) (Hassazadeh and Mansouri, 2005).

The thermal efficiency of the fuel cell is the ratio of the maximum reversible work done by the system to the heating value of the fuel.

$$\eta_{fuelcell} = \frac{W_{max}}{Q_{in}} = \frac{-\Delta G_R}{-\Delta H_R} \quad (2-11)$$

In general, the thermal efficiency should not exceed unity. However, based on the second law of thermodynamics, where heat addition is required by the process, the fuel cell efficiency might be greater than unity provided that the heat addition by the surroundings was excluded from  $Q_{in}$  (Gardner, 1997). This is shown by Equation (2-12) below;

$$\eta_{fuelcell} = \frac{W_{max}}{Q_{in}} = \frac{-\Delta G_R}{-\Delta H_R + (T_o * \Delta S_R)} = 1 \quad (2-12)$$

The production of useful electrical work comes from the free electrons released by the oxidation of fuel at the anode. These electrons then are carried to the cathode side through an external load without going back through the electrolyte. It is important to keep in mind that the electrolyte function is to conduct ions between electrodes, while preventing electrons released from the anode from returning back towards the cathode. The ions are driven through the electrolyte by the difference in electrochemical potential across it from the oxidation of fuel at the anode (Gardner, 1997). This difference in chemical potential produces an electromotive force (emf) across the cell. The magnitude of the cell emf depends on the number of charges transferred for each mole of fuel converted to electricity in the cell reaction. For example, for one mole of methane

converted ( $\text{CH}_4 + \text{O}_2 = \text{CO}_2 + 2\text{H}_2$ ), eight moles of electron charges are transferred (Gardner, 1997). This results in a total of  $8F$  coulombs of electricity generated per mole of methane. The emf developed by fuels converting methane is shown by Equation (2-13) (Gardner, 1997);

$$E_n = \frac{-\Delta G(T)}{8F} \quad (2-13)$$

where  $F = 96484.6$  coulombs per mole of electrons (Faraday constant),  $G$  is Gibbs free energy and  $T$  is the temperature. In general, the theoretical emf or Nernst potential is given by Equation (2-14) (Gardner, 1997);

$$E_n(T) = E^0(T) - \left[ \frac{RT}{zF} \right] * \left( \left[ \sum n_i \ln \frac{p_i}{p_o} \right]_{\text{products}} - \left[ \sum n_j \ln \frac{p_j}{p_o} \right]_{\text{reactants}} \right) \quad (2-14)$$

where  $E^0(T)$  is the standard or Gibbs potential of the fuel cell reaction,  $z$  is the number of electrons transferred per molecule of fuel converted,  $n$  is the number of moles and  $p$  is the partial pressure. Eventually, the theoretical work from an anion-conducting electrolyte fuel cell would be equivalent to the isothermal expansion of oxygen from its partial pressure in the cathode air stream to its partial pressure in the anode (Gardner, 1997).



## 2.5 Direct Oxidation of Hydrocarbons in SOFCs

There has been considerable research in the oxidation of simple hydrocarbons in SOFCs. However, any fuel can, in principle, be oxidized in an SOFC with very few exceptions. The common statement in the fuel cell community is that “fuel cells work on any fuel as long as its hydrogen” (Gorte et al., 2000). The fact that fuel cells run on hydrogen is sometimes stated to be an advantage since hydrogen is renewable, but this ignores the fact that the vast majority of hydrogen is generated by reforming hydrocarbons. The other difficulty involved in the production of hydrogen is its distribution and storage. This has resulted in research into developing fuel cells that can operate based on the direct oxidation of hydrocarbons, specifically methane as the fuel. The direct oxidation of methane in SOFCs was first reported in detail by Steele et al. (1998). It was observed that methane could be converted into carbon dioxide and water with good activity on oxide-based electrodes using platinum as a current collector. Furthermore, it was found that the oxidation on some electrodes was only partial and that the selectivity depended on the composition of the electrode material (Steele et al., 1998).

However, several major problems remain to be investigated before such SOFCs can be routinely operated on the direct feed of alternative hydrocarbon fuels other than hydrogen. One of the problems includes carbon deposition on the anode, causing a blockage of active sites and degradation of cell performance, as well as poor durability (Sangtongkitcharoen et al., 2005). For example, nickel cermets are the common anode material in SOFCs, but Ni/YSZ was found to catalyze the formation of carbon fibers that will separate the fine nickel particles from the YSZ (Mogensen and Kammer, 2003). Therefore, further research on replacing nickel with different anode materials and

processes were investigated to solve such problems. It is important to note the reactions involved carbon deposition at the anode require further insight to understand the mechanism of deactivation. The following reactions related to carbon formation that are most probable are (Sangtongkitcharoen et al., 2005):



There have been attempts to steam reform the hydrocarbon in a fuel cell, where high conversions require high temperatures. It was found that carbon formation becomes thermodynamically unfavored when the steam to methane ratio is greater than one (Sangtongkitcharoen et al., 2005). Unfortunately, steam reforming of hydrocarbons other than methane can easily lead to carbon formation. As the operating temperature in the SOFC increases, carbon formation was found to decrease (Sangtongkitcharoen et al., 2005). This statement was not observed in this research and also disagrees with the results of Murray et al., 1999.

It was found that using conventional nickel based anodes produced excellent power densities and stable operation for dry methane fuels between 500 – 700 °C because carbon formation from methane is not thermodynamically favored at these temperatures (Murray et al., 1999). However, carbon formation was observed when ethane was used as the fuel (Murray and Barnett, 1999). This is, however, in contrast to the fact that the rate of formation of carbon is highest at temperatures between 500 and 650 °C

(Mogensen and Kammer, 2003). Kim et al. (2001) also showed that Ni/YSZ exposed in dry methane at 800 °C for 1.5 hours resulted in complete destruction of the cermet, with carbon formation equal to several times the weight of the nickel cermet. The ideal replacement for conventional nickel based anodes should be easy to maintain in the metallic state, easy to process and catalytically inert towards carbon formation. Cobalt and iron have been tried as a replacement for nickel, but exhibit similar catalytic properties to that of nickel and result in carbon formation (Gorte et al., 2000). Oxides have also been used as the anode for direct oxidation in SOFCs, but were found to give low power densities for practical use because oxides have lower electronic conductivities than precious metals (Gorte et al., 2000).

Copper based anodes have been researched intensely in the past few years. Copper is relatively inert for the formation of C-C bonds and is relatively inexpensive (Gorte et al., 2000). The substitution of nickel with copper was shown to eliminate the formation of graphite from hydrocarbon fuels, including fuels that are liquid at room temperature, such as n-decane, toluene and synthetic diesel (Hyuk et al., 2001). Copper provides good electronic conductivity necessary for anode performance but is not active for the oxidation of hydrocarbons (Gorte et al., 2000). Compositional metal alloys with nickel have been investigated in the past. Kim et al. (2002a) examined the use of copper/nickel alloys as anodes for direct oxidation of methane at 800 °C for 1.5 hours. They demonstrated that carbon formation was greatly suppressed when nickel is mixed with copper. For a Cu:Ni ratio of 9:1, only small amounts of carbon formed and at a ratio of 1:1, carbon formation seemed to be self limiting and the cermet was not fractured. Nickel was mixed with copper in order to enhance the activity and stability of the anode

material. It is also important to note that increasing reduction temperature and time significantly suppresses carbon formation. It was suggested that the higher reduction temperatures lead to increased copper enrichment (Kim et al., 2002a).

CeO<sub>2</sub> was also added to the copper based anodes to provide ionic and electronic conductivity, thereby increasing the TPB and providing catalytic activity for the oxidation of hydrocarbons (Gorte et al., 2000). This led to intense research related to the addition of CeO<sub>2</sub> to the anode material. Both doped and undoped ceria are mixed ionic and electronic conductors at low oxygen partial pressures and are considered to be promising candidates for SOFC anodes (Marina and Mogensen 1999). It was found that ceria based copper anodes performed much better than copper based anodes without ceria (Gorte et al., 2000). Cu/YSZ was found to exhibit very poor performance when using dry methane at 800 °C (Park et al., 1999). Low values of overall cell voltage demonstrated that Cu/YSZ is essentially inert to methane, acting as neither an electrocatalyst for direct oxidation of methane nor a catalyst to form hydrogen, which could then be oxidized in a subsequent step. On the other hand, when ceria was introduced to the Cu/YSZ catalyst, significant improvement in cell performance was observed (Park et al., 1999). Park et al. also pointed out that the anode is not the only limiting factor in cell performance. Better performance can be expected from using thinner electrolytes and optimized cathodes. McIntosh et al. (2003) found similar results with the addition of ceria to Cu/YSZ. Various fuels such as methane, propane, butane and decane were used with Cu-ceria-YSZ anodes and enhanced performance was noted due to improved connectivity of the electron-conductive phase (McIntosh et al., 2003).

Copper and cobalt mixtures have also been investigated for anode cermets. Mixtures of Cu-Co contents as high as 50 wt% were stable in n-butane at 700 °C for at least 3 hours (Mcintosh and Gorte, 2004). Since cermets made with 100% cobalt were not stable to carbon formation, it appears that the cobalt rich phase must be covered by copper. This was evident for surface alloys of copper and cobalt, formed because the surface energy free energy of copper was lower than that of cobalt, providing a driving force for copper to segregate to a Cu-Co surface (Kim et al., 2002b). While, a limited amount of studies involving copper and cobalt mixtures have appeared, the initial results are intriguing.

A number of research groups have studied nickel/ceria cermet anodes for zirconia based SOFCs, in addition to ceria-gadolinia based SOFCs. Nickel/ceria cermet anodes have been shown to give good performance in ceria based SOFCs operating at temperatures as low as 500 °C (Ormerod, 2003). The addition of ceria to the nickel cermet anode improves the electrical performance and the resistance to carbon deposition (Mogensen et al., 2000; and Tsai and Barnett, 1998). It was found that the catalytic activity of the nickel/ceria anode was higher than that of Ni/YSZ especially at the lower temperatures for the internal reforming of methane (Nakagawa et al., 2001). However, deterioration of the catalytic activity of the nickel/ceria anode was observed at low and high partial pressures of hydrogen and water, respectively. The reason for this could be due to oxidation of the nickel surface by water in both the reaction gas and that produced by the anodic reaction (Nakagawa et al., 2001). The addition of 0.2 grams of ceria per gram of nickel cermet (40 wt% nickel), resulted in higher performance compared to Ni/YSZ using hydrogen as the fuel (Park et al., 1999). Unfortunately, both nickel anodes

deactivated quickly when dry methane was introduced. Various dopants have been incorporated into nickel/zirconia and nickel/ceria anodes in an attempt to modify their behavior, particularly in terms of their reforming activity and their resistance to carbon deposition and tolerance to sulfur, which lead to deactivation and loss of cell performance (Ormerod, 2003). Dopants that have been studied include molybdenum, gold, ruthenium and lithium (Mogensen et al., 2002).

Anodes of rare earth doped ceria have been reported to sustain direct oxidation of methane (Marina and Mogensen, 1999). Marina and Mogensen (1999) presented work with gadolinia-doped ceria incorporated in YSZ at atmospheric pressure and in the temperature range of 800 – 1015 °C. It was found that ceria suppressed carbon deposition in a methane-rich atmosphere on the catalysts and anode, which resulted in the operation of the fuel at a low steam to carbon ratio. Unfortunately, gadolinia-doped ceria produced low electrocatalytic activity towards methane oxidation due to the material of the anode current collector, which was found to be inert for electrochemical methane oxidation (Marina and Mogensen, 1999).

The practical feasibility of operating a fuel cell directly with hydrocarbon fuels has only been recently demonstrated. Several of the major alternative material challenges are still uncertain and will probably only become apparent after long term testing in more realistic operating conditions (Gorte et al., 2000). If SOFCs are to be used for transportation and portable power generation systems, the cells will need to be mechanically stable and capable of rapid heating to at least 500 °C, since direct-oxidation fuel cells will require operating temperatures at least as high as that required for catalytic combustion (Farrauto et al., 1992).

## 2.6 Fuel Cell Research using H<sub>2</sub>S

H<sub>2</sub>S is a major pollutant and is a by-product in many process operations, such as hydrotreating, processing of natural gas and coking. It is anticipated that additional large quantities of H<sub>2</sub>S will be produced when coal liquefaction attains commercial importance (Wei and et al., 2004). Hydrogen sulfide is also contained in petroleum and natural gas. Natural gas may contain hydrogen sulfide concentrations between less than 10 ppm to over 500,000 ppm (Chuang et al., 2001). The treatment and disposal of hydrogen sulfide is regarded as a worldwide problem. Processes developed to remove and recover H<sub>2</sub>S include adsorption, absorption, conversion to elemental sulfur and oxidation to sulfur oxides. The capital investment required to facilitate sulfur recovery units is significant. Therefore, researchers are looking for a more economical solution in recovering H<sub>2</sub>S and to minimize its environmental impact. It has been a significant goal to utilize the large amount of energy associated with the conversion of H<sub>2</sub>S to sulfur or sulfur dioxide as electrical energy (Liu et al., 2003). Fuel cell technology provides a potential economical solution for sulfur recovery because fuel cells generate high-grade electric power from the large amount of chemical energy available from the oxidation of H<sub>2</sub>S and can convert H<sub>2</sub>S selectively to high-purity sulfur (Wei et al., 2004). H<sub>2</sub>S has a high chemical potential (0.742 V if sulfur is produced and 0.758V for sulfur dioxide as the product, at 750 °C and 1 atmosphere), which serves as the motivation for using H<sub>2</sub>S as an alternative fuel in SOFCs (Liu et al., 2001).

The feasibility of electrochemically oxidizing H<sub>2</sub>S in a fuel cell was first reported by Pujare et al. (1987). This resulted in research in alternative electrolytes and anode materials for H<sub>2</sub>S applications in SOFCs. The potential for using H<sub>2</sub>S in a fuel cell has

long been recognized, but has not been commercially attained. The highest output reported for a SOFC H<sub>2</sub>S fuel cell is 400 mW/cm<sup>2</sup> power density, attained at 770 °C using lithium cobalt sulfide as the anode and a Siemens Westinghouse YSZ electrolyte/cathode assembly (He et al., 2002). Suitable anode materials exposed in a H<sub>2</sub>S environment should have good electrical conductivity, good catalytic activity and sulfur tolerance at high temperatures (Pujare et al., 1987). Unfortunately, H<sub>2</sub>S is a very corrosive and toxic gas. It is known to degrade fuel cell performance containing a variety of anode materials. In the past, Siemens Westinghouse testing of SOFCs specified a sulfur acceptance level of 0.1 ppmv due to its detrimental effects on fuel cell performance (Israelson, 2004). Although, high sulfur tolerance can be achieved with SOFCs that have anodes based on electronically conductive oxides or sulfides, operating temperatures should still remain quite high (800 °C and higher) to achieve reasonable electronic conductivities and performance (Hongpeng et al., 2005). Intense research has been developed on lowering the operating temperature of SOFCs for economical reasons as well as simplifying fuel cell design and materials. Thus, there is a need for the development of sulfur tolerant anodes at lower operating temperatures.

Platinum is a popular anode material used in SOFCs with pure hydrogen as the fuel, and this anode gives promising results. Unfortunately, platinum degrades over time in an H<sub>2</sub>S environment (He et al., 2002). This phenomenon is related to the reversible formation and decomposition of PtS on the platinum anode interface surface. At temperatures higher than 850 °C, poisoning and fouling of the anode are partly alleviated due to thermal stability of PtS (He et al., 2002). Moreover, most metal and metal oxides are severely corroded by H<sub>2</sub>S at high temperatures (Liu et al., 2003). Matsuzaki and



Yasuda (2000) also found that the Ni/YSZ cermet electrode was degraded when the concentration of H<sub>2</sub>S exceeded 2 ppmw at 1000 °C. It is also important to note that 2-15 ppm H<sub>2</sub>S deteriorates the electrode at 1000 °C, but the poisoning effect is reversible when an H<sub>2</sub>S-free fuel is supplied again.

There has been considerable research on metal sulfides as an alternative anode catalyst. Metal sulfides are much more economical compared to precious metals. Of the materials Pujare et al. (1987) examined, it was found that NiFe<sub>2</sub>S<sub>4</sub> and WS<sub>2</sub> had the best exchange current densities. The performance of a SOFC utilizing 50% H<sub>2</sub>S (balance nitrogen) as the fuel was studied with cobalt, tungsten and lithium cobalt metal sulfides (Yates and Winnick, 1999). Cobalt sulfide was found to degrade into jaipurite (CoS<sub>1.035</sub>), which resulted in the delamination of the anode from the YSZ. This was a major problem that led to poor performance of the fuel cell. Tungsten sulfides were also examined and were shown to be much more stable than cobalt sulfides. Lithium cobalt sulfides (Li<sub>2</sub>S/CoS<sub>1.035</sub>) were investigated and gave the best cell performance compared to the others; however, the cell performance still decreased over time. The operation at high temperatures may have caused slow sintering of the Li<sub>2</sub>S/CoS<sub>1.035</sub> (Yates and Winnick, 1999).

Metal (iron, cobalt and nickel) based molybdenum sulfide catalysts display high activity in an H<sub>2</sub>S environment, a general feature recognized in MoS<sub>2</sub> based hydrodesulfurization catalysts (Liu et al., 2003). It is also known to be sulfur tolerant, as well as being an effective catalyst for reversible decomposition of H<sub>2</sub>S at temperatures above 600 °C (Chivers and Hyne, 1980), and it was found to form an active anode catalyst that is characterized by good electronic conductivity (Wei et al., 2004). However,

MoS<sub>2</sub> is volatile at high temperatures. On the other hand, a Ni-Mo-S composite has been found to be involatile, with nickel adding additional catalytic activity to the anode (Wei et al., 2004). A high performance metal sulfide-based anode consisting of a composite molybdenum nickel sulfide admixed with YSZ (ionic conductor) and silver (electronic conductor) was investigated by Wei et al. (2004). The cell performance was tested by adding pure H<sub>2</sub>S into the anode feed at 750 and 850 °C. Ni-Mo-S alone contained no strong ionic conductors that creates limited anode reactions adjacent to the electrolyte. Mixtures of 0-10 wt% of one or both silver and YSZ were added to the Mo-Ni-S anode, and it was found that the addition of less than 5 wt% of either silver or YSZ produced little benefit. This is not surprising since silver is an electronic conductor and would not enhance ionic conductivity in the anode. Improvement in ionic conductivity would be required to result in an increase in overall cell performance. Thus, YSZ was added to increase the ionic conductivity, which would be expected to increase the reaction zone in the anode. When the temperature was increased to 850 °C, the fuel cell performance was increased dramatically (Wei et al., 2004), and similar results occurred when silver powder was added to Co-Mo-S (Liu et al., 2003). However, the addition of greater than 10 wt% of either silver or YSZ resulted in detrimental effects. These effects included silver particle agglomeration on the anode surface and dense anode materials produced when too much YSZ was added. Thus, particle agglomeration decreases the cell performance by providing an extra barrier for mass-transport processes of reactants and products. A mixture of 5 wt% each of silver and YSZ into Ni-Mo-S gave the best results (Wei et al., 2004). It is also important to note that the anodes containing silver were less sintered, had higher surface areas and were more porous than the corresponding anodes

without silver. Therefore, anode morphology plays a significant role in cell performance (Wei et al., 2004). It is also well understood that silver readily reacts with sulfur at low temperatures to form silver sulfides. Fortunately, the reaction is reversed at temperatures above 200 °C when silver sulfide thermally decomposes into its elements (Macintyre, 1992).

Lui et al. (2003) incorporated molybdenum sulfides with various metals such as iron, cobalt and nickel, which have shown to be stable and active at temperatures up to 850 °C using pure H<sub>2</sub>S as the fuel and air supplied as the oxidant. They also found that there was poor electrical contact between the platinum current collecting layer and the anode layer. This problem was solved by adding silver powder into the anode material as the current collector instead of applying a platinum layer. The results showed that the addition of silver powder (up to 10% by weight) into the Co-Mo-S catalyst improved the cell performance and the cell was stable over an extended period of time. The ideal temperature for producing the greatest performance was found to be 850 °C. These observations were consistent with a mechanism in which sulfur was generated more rapidly at active sites than it was removed by desorption and transport at 800 °C, which limited the ability of H<sub>2</sub>S fuel to access the triple-phase boundary (Liu et al., 2003).

Clearly, there has been much research on metal sulfide anode materials. Research on metals and oxides has also been the subject of intense investigation. Nickel, being the most common metal used as an anode material in SOFCs, is known to be quickly poisoned by H<sub>2</sub>S at levels as low as 0.05 ppmw at 800 °C, improving only slightly with increasing temperature (Matsuzaki and Yasuda, 2000). The reason for this is that surface sulfides instead of bulk sulfides of nickel are formed at low levels of sulfur, which block

the active sites that cause deactivation of anode performance (Hongpeng et al., 2005). Hyuk et al. (2001) presented a study of copper (20 wt%) and ceria (10 wt%) in YSZ. The operating conditions were first pure hydrogen at 700 °C for 16 hours and then switched to 50 mol% n-decane (5000 ppm S) for another 24 hours. The resistance was then measured and the results show that the presence of sulfur at these levels gave rise to no measurable changes in resistance, implying that copper was not affected significantly. These results are not surprising given that equilibrium calculations have proven that  $\text{Cu}_2\text{S}$  formation is not favorable at these operating conditions (Hyuk et al., 2001). It is known that surface sulfides are more stable than bulk  $\text{Cu}_2\text{S}$  (Bartholomew et al., 1982). Thus, their presence would not have a significant effect on anode performance, since the role of copper appears to be only that of providing electronic conductivity (Gorte et al., 2000). On the other hand, the current density decreased dramatically when 5000 ppmw sulfur was introduced and could only be restored with steam. These results show that copper combined with ceria can be used with moderate levels of sulfur (Hyuk, et al., 2001). Hongpeng, et al. (2005) later demonstrated that copper-ceria anodes operated well at 800°C in an  $\text{H}_2\text{S}$  environment (up to 450 ppm). Unfortunately, at high  $\text{H}_2\text{S}$  levels, anode deactivation was observed and can be attributed to the reaction of the  $\text{CeO}_2$  with  $\text{H}_2\text{S}$  to form  $\text{Ce}_2\text{O}_2\text{S}$ . Copper-ceria was also found to be capable of generating electric power using less processed fuels, such as jet fuels and Pennsylvania crude oil, containing sulfur up to 900 ppmw (Zhou et al., 2004). This study showed stable power generation for 30 hours on both jet fuel and crude oil, and over 100 hours when nitrogen was used to dilute the fuel and crude oil.

Investigation on composite oxide anode materials are also being studied due to their increased stability and desired electrical properties. Pyrochlore oxides based on  $Gd_2Ti_2O_7$  with partial substitution of titanium and molybdenum ions has been shown to be sulfur tolerant in a fuel gas mixture of 10%  $H_2S$  and 90%  $H_2$  (Zha et al., 2005). It is interesting to note that there was more than 50% improvement in the peak power when exposed in  $H_2S$  compared to pure hydrogen. Zha et al. (2005) hypothesis on this observation was that this improvement was partly due to the enhanced dissociative adsorption/diffusion of hydrogen on the titanium and/or molybdenum sites. The other possible reason may be due to the selective catalytic activity of  $Gd_2Ti_{1.4}Mo_{0.6}O_7$  towards electrochemical oxidation of  $H_2S$ . Luis et al. (2004) focused on the stability and electrochemical performance of perovskite-type materials in a  $H_2S$  mixture (10%  $H_2S$  in 90%  $H_2$  and 90%  $N_2$ ). Strontium-doped lanthanum vanadium oxide (LSV) based anodes were investigated and found to be stable in the presence of  $H_2S$ , suggesting that LSV anodes are very active toward the electrochemical oxidation of  $H_2S$  (Luis et al., 2004). The interfacial resistances decreased when exposed to  $H_2S$ , confirming that LSV was stable. There was also a noticeable increase in cell performance in the presence of  $H_2S$ . Previous studies have indicated that LSV would not be a suitable anode because it could potentially form a nonconductive  $Sr_3V_2O_8$  phase at very low oxygen partial pressures. The possible reason is that the ions from the cathode side would readily react with the LSV, creating an insulating layer for electronic transport and result in a decrease in cell performance. However, when  $H_2S$  is present the formation of a conductive vanadium sulfide phase occurs instead of an insulating  $Sr_3V_2O_8$  (Luis et al., 2004).

There has also been research on the poisoning effect of sulfur on SOFC anodes to aid in the search for a better sulfur tolerant and active anode for SOFC use. Previous studies used direct-current polarization methods and impedance analysis to evaluate poisoning effects on sulfur, which generally show that even low levels of H<sub>2</sub>S may cause significant performance losses at the fuel electrode (Matsuzaki and Yasuda, 2000). Several possible reasons may account for the decrease in performance due to the presence of H<sub>2</sub>S. However, the exact reason for H<sub>2</sub>S degradation has not yet been clearly defined (Matsuzaki and Yasuda, 2000). As seen earlier, there are many benefits in reducing the operating temperature in an SOFC. On the other hand, it was found that decreasing the operating temperature increases the possibility of sulfur impurities to absorb onto the surface of the fuel electrode (Matsuzaki and Yasuda, 2000), which was seen earlier.

## **2.7 Summary of Literature Review**

The main purpose of this research is focused on the identification of potential sulfur resistant anode materials for the application in a hydrogen sulfide compatible SOFC. Properties of ideal anode materials would include tolerance to H<sub>2</sub>S, good electrical conductivity, and active towards direct oxidation of hydrocarbon fuels at high temperatures. The feasibility for electrochemically oxidizing H<sub>2</sub>S in a SOFC was first reported by Purjare et al. (1987). This led to considerable research in alternative electrolytes and anode materials for H<sub>2</sub>S applications in SOFCs. The presence of H<sub>2</sub>S results in degradation of the anode and fuel cell performance due to the corrosive nature of H<sub>2</sub>S, even at low concentrations. Most metal and metal oxides are known to be severely corroded by H<sub>2</sub>S at high temperatures (Liu et al., 2003). Platinum, a popular

anode material used in SOFCs, was studied in the presence of H<sub>2</sub>S. Unfortunately, platinum degrades over time in an H<sub>2</sub>S environment (He et al., 2002). There has also been considerable research on the effects of H<sub>2</sub>S on Ni/YSZ, the most common anode used in SOFC applications. Matsuzaki and Yasuda (2000) found that Ni/YSZ cermet degraded when the concentration of H<sub>2</sub>S reached as low as 0.05ppmw at 800 °C, improving slightly with temperature and the poisoning effect is reversible when an H<sub>2</sub>S-free fuel is supplied again. Copper combined with ceria, utilizing pure hydrogen and varying concentrations of H<sub>2</sub>S at 700 °C, has been investigated by Hyuk et al. (2001). It was found that copper-ceria operated well at 800 °C in an H<sub>2</sub>S environment up to 450 ppm H<sub>2</sub>S.

Considerable research also involves metal sulfides as another promising anode for the use of H<sub>2</sub>S operated SOFCs. Metal sulfides are more economical compared to precious metals and have been found to be more resistant to H<sub>2</sub>S compared to conventional metal and metal oxide supports. In particular, metal based molybdenum sulfides such as Ni-Mo-S (Wei et al., 2003) and Co-Mo-S (Liu et al., 2003) promoted in silver were found to be sulfur tolerant, and effective catalysts for reversible H<sub>2</sub>S decomposition. It is also important to note that many researchers confirmed that these anodes in the presence of H<sub>2</sub>S produced the greatest performance at higher temperatures. These observations were thought to be related to a mechanism in which sulfur was generated less rapidly at the active sites compared to those being removed by desorption (Liu et al., 2003). However, several possible reasons may account for the decrease in performance due to the presence of H<sub>2</sub>S. The exact reason for H<sub>2</sub>S degradation has not yet been clearly define in literature (Matsuzaki and Yasuda, 2000).

Considerable research has been done on obtaining active and H<sub>2</sub>S tolerant anodes for operation in an H<sub>2</sub>S compatible SOFC. However, most of the research involves the investigation of the anodes for direct H<sub>2</sub>S oxidation. Thus, more research is required involving H<sub>2</sub>S resistant anode materials for the direct oxidation of hydrocarbon fuels in a SOFC with H<sub>2</sub>S as an impurity. This research will provide knowledge and understanding on the fundamental reaction kinetics on methane oxidation of various metals and metal oxides for application in a H<sub>2</sub>S compatible SOFC.



# Chapter 3

## Experimental Methods

### 3.1 Objective

The main objective of this research is the analysis of potential sulfur resistant anode materials for the application in a hydrogen sulfide compatible solid oxide fuel cell. Furthermore, this study will develop an understanding of the reactivity and kinetics using various catalysts for methane oxidation in the presence of hydrogen sulfide. Surface characterization techniques such as XPS and BET surface area will be used to aid in understanding the nature and reaction kinetics of the various anode materials.

### 3.2 Materials Used for Catalyst Preparation and Testing

1. Nickel (II) nitrate hexahydrate ( $\text{Ni}(\text{NO}_3)_2 \cdot 6 \text{H}_2\text{O}$ ), Aldrich, 99%.
2. Copper (II) nitrate hemipentahydrate ( $\text{Cu}(\text{NO}_3)_2 \cdot 2.5\text{H}_2\text{O}$ ), Aldrich, 99.99+%.
3. 8 mol% yttria ( $\text{Y}_2\text{O}_3$ )-stabilized-zirconia ( $\text{ZrO}_2$ ), (TZ-8Y), Tosoh.
4. Lithium carbonate ( $\text{Li}_2\text{CO}_3$ ), Fisher, 99 %
5. Cobalt (II) carbonate hydrate ( $\text{CoCO}_3 \cdot x\text{H}_2\text{O}$ ), Aldrich, 99%.
6. 9.87 % oxygen / balance helium gas mixture, Praxair.
7. 10 % hydrogen / balance argon gas mixture, Praxair.
8. 29.9 % nitrogen / balance helium gas mixture, Praxair.
9. Ultra high purity helium gas, Praxair, 99.999% (5.0 grade)
10. 24.9 % methane / balance helium, Praxair.

11. 101 ppm H<sub>2</sub>S, 25.2 % methane / balance helium, Praxair.

### 3.3 Catalyst Preparation

The five anode catalysts prepared for this study include nickel (Ni/YSZ), copper (Cu/YSZ), nickel/copper (Ni/Cu/YSZ) and two different preparations of lithium cobalt oxide (LiCoO<sub>2</sub>/YSZ), all incorporated into a yttria-stabilized zirconia (YSZ) support. The Ni/YSZ, Cu/YSZ and Ni/Cu/YSZ catalysts were prepared using wet impregnation. Wet impregnation is a common method to prepare anode cermets, and the preparation procedure described by Cracium et al. (1999) was used to prepare the Ni/YSZ, Cu/YSZ and Ni/Cu/YSZ catalysts. LiCoO<sub>2</sub>/YSZ was prepared using a solid-state reaction procedure. The total metal content used in all the catalysts was approximately 20 mole percent. The wet impregnation method was performed by mixing the support (8 mol% YSZ, Tosoh) and the corresponding metal nitrates. The nitrate powder was first dissolved in about 1 gram of water. The amount of water was determined by first mixing the water drop wise into a pre-determined YSZ support until the YSZ support was just wet (incipient). Once the aqueous nitrate solution was made, it was then physically mixed with the YSZ powder. The catalysts were then dried overnight at 110 °C to remove any excess water, ground to a fine powder with a mortar and pestle and then calcined at 950 °C for 2 hours at a heating and cooling rate of 5 and 3 °C/min, respectively. Table 3-1 illustrates the composition of material used for each catalyst prepared using wet impregnation.

Table 3-1. Compositions of metal nitrates and YSZ used for catalyst preparation using wet impregnation.

Catalyst	Nitrate Compound	Mass of nitrate used (g)	Mass of YSZ used (g)	Mass of water used (g)
Ni/YSZ	$\text{Ni}(\text{NO}_3)_2 \cdot 6\text{H}_2\text{O}$	2.765	5.001	1.035
Cu/YSZ	$\text{Cu}(\text{NO}_3)_2 \cdot 2.5\text{H}_2\text{O}$	2.804	5.002	1.047
Ni/Cu/YSZ	$\text{Ni}(\text{NO}_3)_2 \cdot 6\text{H}_2\text{O}$	1.384	5.001	1.034
	$\text{Cu}(\text{NO}_3)_2 \cdot 2.5\text{H}_2\text{O}$	1.077		

The  $\text{LiCoO}_2/\text{YSZ}$  catalysts were prepared using two different solid-state reaction methods as described by Ohzuku and Ueda (1994). The first method consists of physically mixing the lithium carbonate, cobalt carbonate and the YSZ support (YSZ) together followed by calcination. The second method of preparing the  $\text{LiCoO}_2/\text{YSZ}$  catalyst was performed by first mixing the metal carbonates followed by the calcination procedure. After the catalyst was calcined, the catalyst was ground into a fine powder then mixed with YSZ and again calcined. The calcination procedure was performed at 850 °C for 24 hours followed by another 12 hours at 650 °C. The decomposition of lithium cobalt oxide is around 900 °C (Antolini, 1998). Thus, the calcination temperature did not exceed 900 °C to avoid decomposition of the catalyst. Table 3-2 shows the carbonate and YSZ compositions used to prepare the  $\text{LiCoO}_2/\text{YSZ}$  catalysts.

Table 3-2. Composition of carbonates and YSZ used for catalyst preparation using a solid-state reaction method.

	Carbonate Compound	Mass of carbonate used (g)	Mass of YSZ used (g)
LiCoO <sub>2</sub> /YSZ (Prep 1)	Li	0.352	10.001
	Co	1.132	
LiCoO <sub>2</sub> /YSZ (Prep 2)	Li	0.352	10.003
	Co	1.132	

### 3.4 Characterization by X-Ray Photoelectron Spectroscopy (XPS)

XPS is one of the most versatile techniques used for analyzing surfaces chemically. XPS is used to determine the surface elemental composition, the oxidation state of the element, and in favorable cases, on the dispersion of one phase over another. The foundation of this technique comes from Einstein's explanation of the photoelectric effect, whereby photons can induce electron emission from a solid provided the photon energy ( $h\nu$ ) is greater than the work function ( $\phi$ ). The work function is defined as the minimum energy required to remove an electron from the highest occupied energy level in the solid to the vacuum level. In other words, an atom absorbs a photon of energy then core or valence electrons with binding energies are ejected with kinetic energy (Niemantsverdriet, 1995). In XPS, a monochromatic beam of x-rays (Mg K $\alpha$  or Al K $\alpha$ ) is incident upon a solid surface, causing photoemission from both core and valence levels

of surface atoms into the vacuum. Chemical identification is related to the core electrons deep inside the atoms that are largely insensitive to their surroundings when condensed into the solid phase and retain binding energies,  $E_B$ , that are signatures of the atom type, i.e. the number of protons in the nucleus (Attard and Barnes, 1998). Applying the principle of energy conservation, one may estimate the kinetic energy of emitted photoelectrons ( $E_{KIN}$ ), demonstrated by Equation (3-1) (Attard and Barnes, 1998).

$$E_{KIN} = h\nu - E_B + \phi \quad (3-1)$$

The binding energy of a core level ( $E_B$ ) is measured with respect to the highest occupied level of the solid. The photon energy is equal to the total energy available to excite a core electron. However, some of the photon energy is transformed into kinetic energy of the photoemitted electrons. Thus, for a fixed photon energy, photoemission from an atom with well-defined core levels (of a particular binding energy) will produce photoelectrons with well-defined kinetic energies, which vary systematically from element to element (Attard and Barnes, 1998).

In this case,  $h\nu$  and  $\phi$  are known, therefore, the measured kinetic energy is converted to a binding energy scale. A representative XPS figure (Figure 3-1) presents photoelectron intensities as a function of binding energy. The XPS library embedded in the data collection software was used to determine the elements present in the sample by the corresponding binding energies of the different elements.

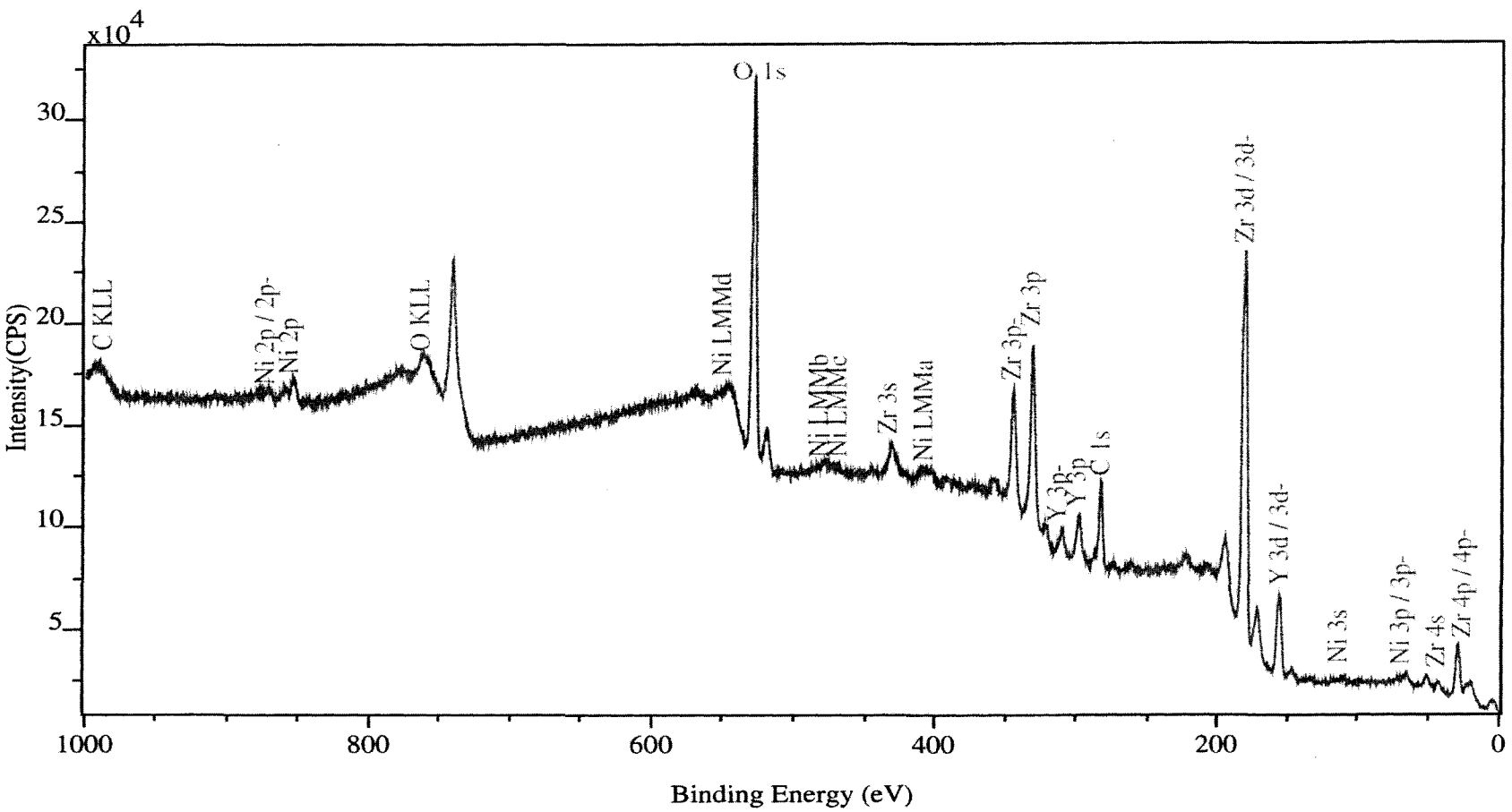


Figure 3-1. XPS Spectrum of Peak Intensity as a Function of Binding Energy for Ni/YSZ.

### **3.4.1 XPS Sample Preparation**

The samples can be prepared either in powder or wafer form. In this study, XPS samples were prepared in a wafer form by weighing about 100 mg of well ground catalyst and placing the sample into a 10 mm die. A 10 mm rod is used to spread the sample evenly on the bottom of the die and then the rod is placed back in the center of the die. Once the die is properly assembled, the die is then pressed firmly with a hydraulic press at a pressure of about 10,000 psi for about 10 minutes. The die is then disassembled and the sample is carefully taken out from the die. The pressed sample should result in a very thin like wafer form. Ethanol was used to clean the die between preparations of samples. The samples are then transferred to the loading chamber of the XPS and degassed overnight, or until the pressure is less than  $1 \times 10^{-7}$  Torr.

### **3.5 Brunauer-Emmett-Teller (BET) Surface Area Characterization**

The principle underlying surface area measurements is to physically adsorb an inert gas (nitrogen) and determine how many molecules are required to form a complete monolayer. However, molecules may adsorb beyond the monolayer to form multilayers (Chorkendorff and Niemantsverdriet, 2003). The BET isotherm provides an extension of the Langmuir monolayer model to multilayer adsorption. One of the major restrictions in utilizing the Langmuir adsorption isotherm is that it does not allow the adsorbate film thickness to be greater than one monolayer. The assumptions of the BET isotherm are as follows (Attard and Barnes, 1998):

- i) Adsorption of the first adsorbate layer is assumed to take place on an array of surface sites of uniform energy (cf. Langmuir assumptions).

- ii) Second layer adsorption can only take place on top of first, third on top of second, etc. When  $P = P_o$  (the saturated vapour pressure of the adsorbate), an infinite number of layers will form.
- iii) At equilibrium, the rates of condensation and evaporation are the same for each individual layer.
- iv) Summation of the amount adsorbed in all layers then give the BET equation, which is expressed in linear form is shown by Equation (3-2).

$$\frac{P}{V_{STP}(P_o - P)} = \frac{1}{V_m C} + \frac{C-1}{V_m C} \times \frac{P}{P_o} \quad (3-2)$$

Equation (3-2) can be further simplified into Equation (3-3),

$$\frac{x}{V_{STP}(1-x)} = \frac{1}{V_m C} + \frac{x(C-1)}{V_m C} \quad (3-3)$$

where  $x = P/P_o$ ,  $V_{STP}$  is the volume at STP (mL),  $V_m$  is the monolayer volume (mL),  $P_o$  is the equilibrium pressure of the condensed gas (approx.  $P_a$ ) in mm Hg,  $P$  is the absolute pressure of nitrogen (% nitrogen/100  $\times P_a$ ) in mm Hg, and  $C$  is a constant (dimensionless). The volumes must first be converted to volumes at standard temperature and pressure.  $V_{STP}$  is calculated by using Equation (3-4).

$$V_{STP} = V \times \left( \frac{273.15K}{273.15K + T_a} \right) \times \left( \frac{P_a}{760mmHg} \right) \quad (3-4)$$



where  $T_a$  (°C) and  $P_a$  (mm Hg) are temperature and pressure, respectively. The unknown parameters are  $V_m$  and  $C$  from Equation (3-3). Equation (3-3) is in a linear form; thus, the slope and intercept can be obtained, and can then be used to determine the values of  $V_m$  and  $C$ . These parameters are then used to determine the surface area illustrated by Equation (3-5).

$$SA = \frac{V_m \times 6.023 \times 10^{23} \times A_{N_2}}{22414 \text{ cm}^3 / \text{mol}} \quad (3-5)$$

where  $SA$  is the surface area in  $\text{m}^2$  and  $A_{N_2}$  is the area of the nitrogen molecule in  $\text{m}^2/\text{molecule}$  ( $0.162 \times 10^{-18} \text{ m}^2/\text{molecule}$ ).

### 3.5.1 AutoChem II 2920 (Automated Catalyst Characterization System)

BET measurements were performed using an AutoChem II 2920 (Automated Catalyst Characterization System). The AutoChem II 2920 is an instrument that is able to automatically perform and control temperature programmed analysis such as oxidation, reduction, desorption, reaction, pulse chemisorption and BET surface area. The AutoChem II 2920 allows gas to flow over the sample and into the analyzer. The gas then interacts with the sample as the temperature changes and reaches the detector. The detector collects the data and the embedded software calculates and plots the results. The type of detector used is called a thermal conductivity detector (TCD). The TCD contains heated filaments, which measure the difference in gas thermal conductivity sensed between the gases flowing over the sample and reference filaments. The gases flowing passed the TCD work to cool the filament by extracting heat. When the gas reaches the

sample, it causes a change in composition of the gas and results in a change in thermal conductivity of the gas. These changes are sensed by the TCD as an increase or decrease in the amount of power required to maintain the filament at a constant temperature (Micromeritics Manual).

### **3.5.2 Sample preparation**

A small amount of quartz wool was placed in a clean quartz U-tube before placing approximately 0.30 grams of the sample into the tube. Subsequently, the side of the U-tube was cleaned with a cotton swab to ensure that most of the sample was located at the bottom of the sample U-tube. The retaining nuts, ferrules and Kalrez® O-rings were placed on the sampling tube which is illustrated by Figure 3-2. The sample tube was then screwed carefully into the AutoChem II 2920.

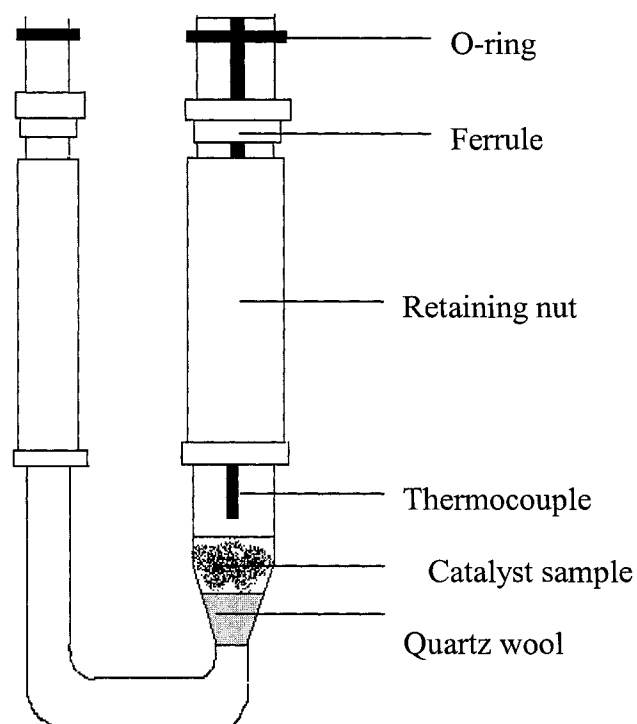


Figure 3-2. Schematic of Quartz Sample Tube and Components for Introduction into AutoChem II.

### 3.5.3 BET Experimental Procedure

Once the quartz sample tube is prepared, it is placed and screwed carefully into the AutoChem II 2920, the furnace is placed over the sample tube and then the experiment is ready to proceed. The sample is first programmed to be outgassed in helium for 1 hour at 300 °C. The reason for this step is to make sure that the catalyst surface is clean from impurities. After the sample has been outgassed in helium, it is then reduced in 10% hydrogen in argon for 20 minutes at 800 °C. The reduction of catalyst is required to allow the oxide material to form into a metallic state. The TCD measures the hydrogen content of the gas mixture before and after reaction. The furnace is taken out after the reduction step is finished and the sample is allowed to cool to room temperature. The TCD is then allowed to stabilize to produce a flat baseline for further analysis. A mixture of 30% nitrogen in helium is then fed across the sample. The sample is then immersed in liquid nitrogen (-196 °C) for the process of nitrogen adsorption. Once the surface is saturated with nitrogen atoms, the desorption of nitrogen takes place by immersing the sample into a water bath (room temperature). The desorption process changes the composition of the inlet nitrogen and helium gas, which is detected by the TCD. The results show the adsorption and desorption peak intensities as a function of time as shown by Figure 3-3.

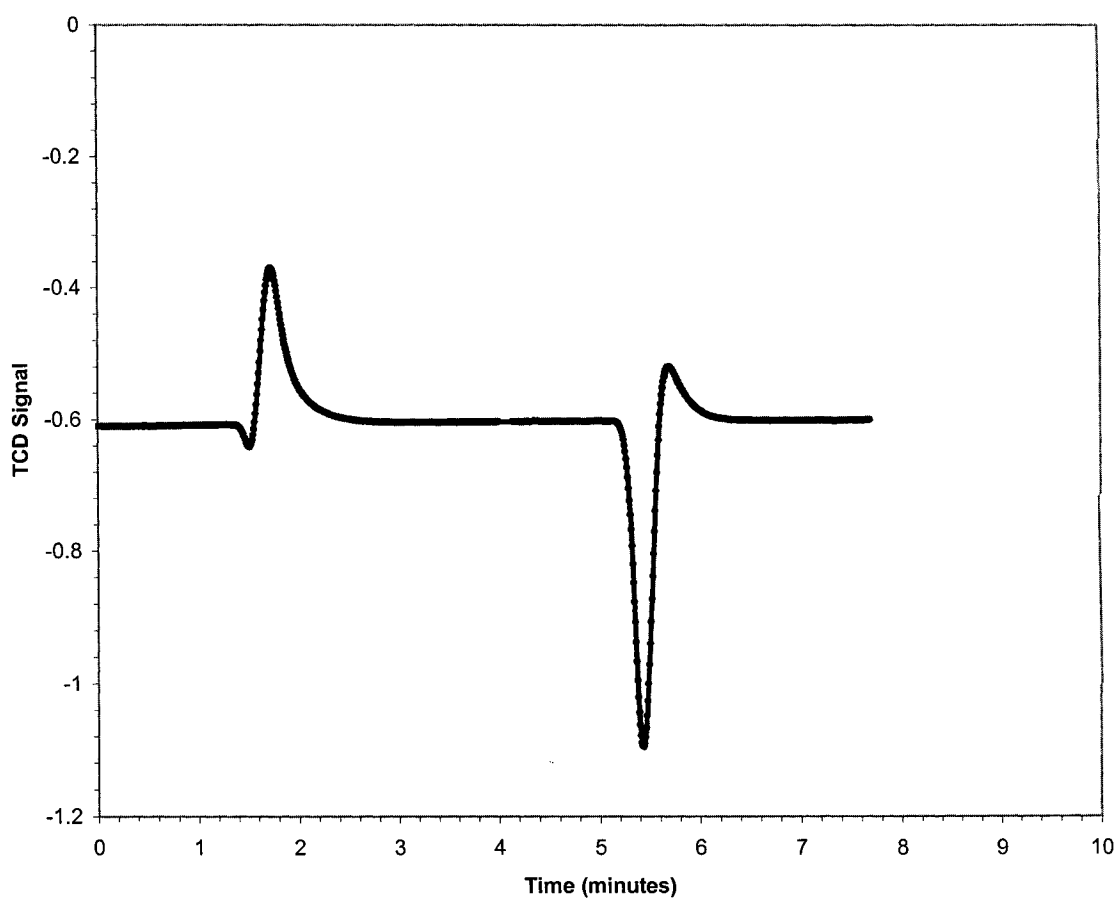


Figure 3-3. BET Surface Area Spectrum for Kaolin Standard in 20% N<sub>2</sub> in Helium

The amount of nitrogen desorbed and the sample weight of the catalyst are used to calculate the surface area. This procedure was repeated two more times with 20% nitrogen and 10% nitrogen in helium, respectively. Three different nitrogen blends were used in order to obtain a multipoint BET surface area measurement. Therefore, a calibration was done previously for all three nitrogen mixtures. The  $V_{STP}$  in Equation (3-2) was obtained by taking the amount of nitrogen desorbed (peak area) from the experiment and combining it with the calibration for the corresponding nitrogen gas mixture. It is important to note that the carrier gas helium was chosen because its thermal

conductivity (relative to air) is greatly different from that of nitrogen. The thermal conductivity (relative to air) of helium and nitrogen are 5.84 and 1.00, respectively (AutoChem II 2920 Operating Manual).

### **3.6 Anode Material Reaction Analysis on Methane Oxidation**

Reaction tests on all five catalysts were performed using the AutoChem II 2920 and a mass spectrometer. The Autochem II 2920 acts as a differential flow reactor and the mass spectrometer analyzes the product gas compositions. A detailed description of the mass spectrometer is discussed in Section 3.6.2. The sample preparation is similar to that shown in Figure 3-2. The mass of sample used was approximately 250 mg for all the catalysts tested and was introduced into the Autochem II 2920. A program, which contains a sequence of steps, was developed to perform a methane oxidation reaction at various temperatures to test the reactivity of the catalysts.

#### **3.6.1 Experimental Procedure for Running Reaction Tests**

Methane oxidation reactions were tested on the five catalysts in a H<sub>2</sub>S free environment and in a H<sub>2</sub>S atmosphere. The reactions were carried out at 500, 600, 700 and 800°C. Therefore, a total of 40 experiments were performed. Repeated runs were also performed in order to validate the first run. The anode material was first reduced in 10% hydrogen balance argon at an increasing temperature rate of 10 °C/min and then held at 800 °C for 20 minutes. Once the catalyst was reduced, the furnace temperature was adjusted to reach the reaction temperature set point. The methane oxidation reaction was then performed by flowing 25% methane and 10% oxygen, both balanced in helium

over the catalyst. The H<sub>2</sub>S environment was simulated by adding 101 ppm H<sub>2</sub>S to the 25% methane in helium mixture. Table 3-3 shows the different conditions (Periods A thru E) used to examine the reactivity of the catalyst towards methane and oxygen for both H<sub>2</sub>S free and H<sub>2</sub>S systems. Each period was held for 30 minutes. It is important to note that Period A contains the theoretical amount of oxygen required to fully combust methane, which is shown by Equation (3-6). The oxygen concentration was decreased from Periods A thru D, illustrated by Table 3-3. Period E conditions were brought back to the same conditions as Period A. This would allow for investigation in catalyst degradation.



Table 3-3. Inlet flow rate conditions and compositions of gases used in reaction tests.

Period	Flow rate of Methane/Helium (ml/min)	Flow rate of Oxygen/Helium (ml/min)	Stoichiometric mole ratio of CH <sub>4</sub> :O <sub>2</sub>
A	10	50	1 : 2
B	20	40	2.5 : 2
C	30	30	5 : 2
D	50	10	25 : 2
E	10	50	1 : 2

### 3.6.2 Analysis of Product Gas Using a Mass Spectrometer

The product gas (methane oxidation reactions) from the AutoChem II 2920 exits the analysis exhaust port and re-enters the mass spectrometer (M200ED). A mass spectrometer is an instrument that measures the masses of individual molecules that have been converted into ions. However, it does not measure the molecular mass directly, but rather the mass-to-charge ( $m/z$ ) ratio of the ions formed from the molecules. In many cases, the ions encountered usually have one charge ( $z = 1$ ), thus  $m/z$  becomes the molecular mass (ionic). The basic operation of a mass spectrometer is shown by Figure 3-4 ([www.asms.org](http://www.asms.org)).

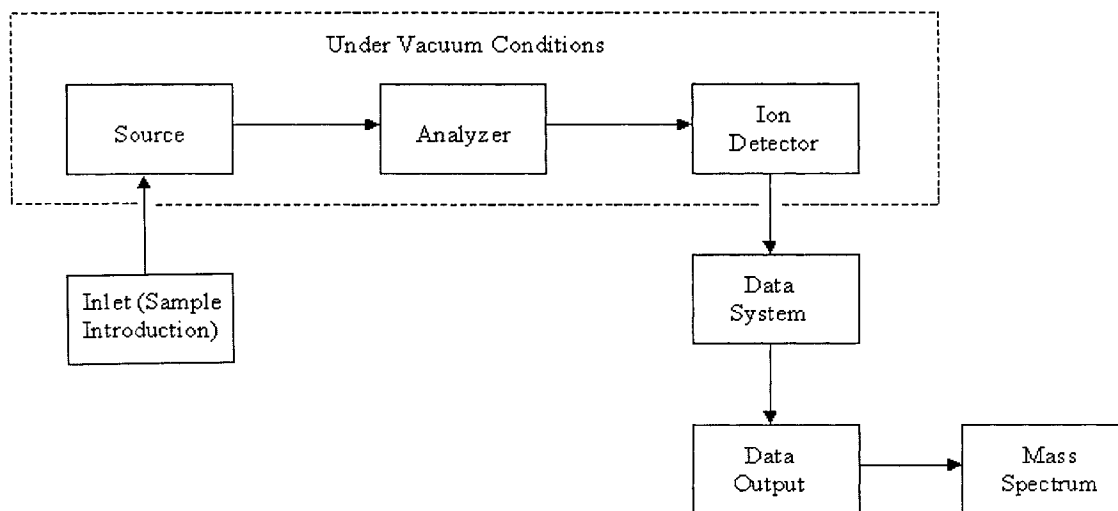


Figure 3-4. Basic Operation of Mass Spectrometer (adapted from [www.asms.org](http://www.asms.org))



The formation of gas phase sample ions is essential to the mass sorting and detection processes that occur in the mass spectrometer. Ions are generated by bombarding the gaseous sample molecules with a beam of energetic molecules. The energy of the bombarding electrons is generally much greater than the bonds holding the molecules together. Therefore, high energy electrons interact with the molecule where ionization occurs and bonds are broken that result in fragments seen by the mass spectrum. The gas phase ions are sorted in the mass analyzer according to their  $m/z$  ratio and then are collected by the detector, and the ion flux in the detector is converted to a proportional current. The magnitude of these electrical signals is then recorded as a function of  $m/z$  ratio by the data system. A vacuum is required around the source, ion detector and analyzer. A rotary pump and a turbomolecular pump were used to create the vacuum. It is important to note that the power source is not to be turned on until the pressure is below  $1.0 \times 10^{-3}$  Torr or else the filament may burn out and deposit oxides in the source elements (MD200 Operating Manual). The mass spectrometer results were collected and saved by an external computer, and the results were exported and plotted using Microsoft Excel. Figure 3-5 shows a mass spectrum of a blank run containing no catalyst using Period B conditions.

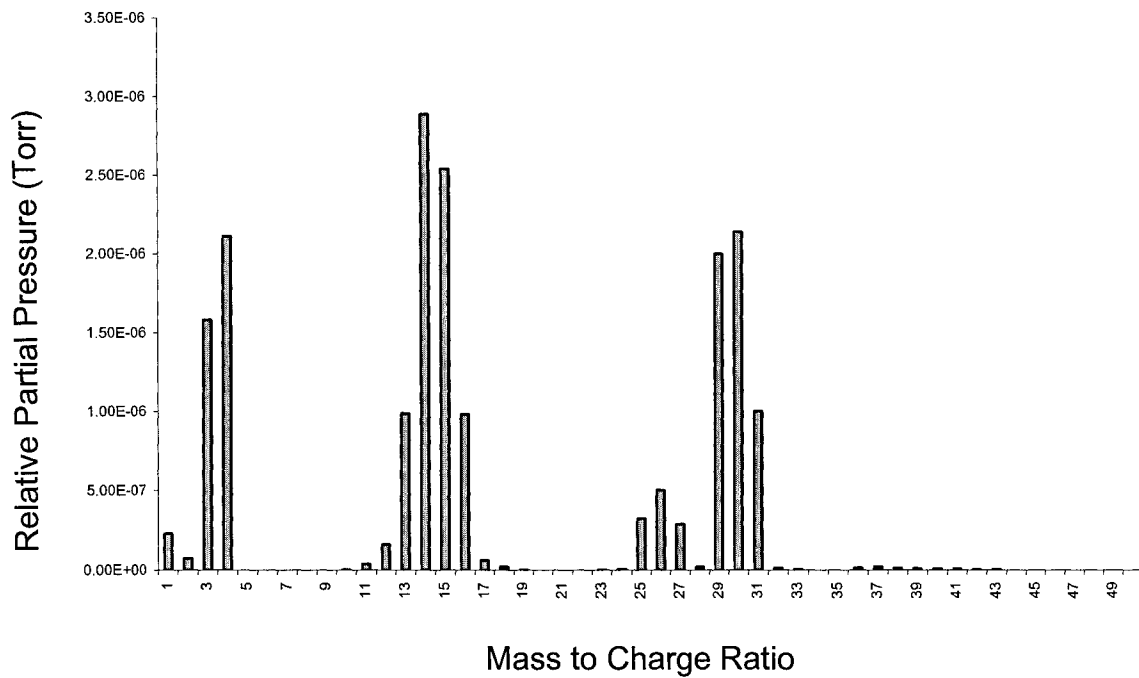


Figure 3-5. Mass Spectrum for Blank Run (Period B conditions) Note: The mass-to-charge ratio values for the different gases were found to be shifted by 2 or 3 mass units due to incorrect instrument calibration.

## Chapter 4

### Results

#### 4.1 XPS Characterization Results

Surface compositional metal loadings and oxidation states were determined using x-ray photoelectron spectroscopy (XPS). The XPS results are shown in Table 4-1. Survey and narrow scans were performed for the purpose of obtaining metal compositions (mass percent) and the metal oxidation states, respectively. The elemental compositions in the sample were calculated using a peak fitting method to extract the peak areas of the individual elements in the samples, which were used to determine the compositions. Similarly, peak fitting was also required to obtain the oxidation states of the metals in the sample. The peak fitting software determines the binding energies of the individual elements and also corrects the binding energy by referencing to adventitious carbon. Once the corrected binding energies are determined, the oxidation state of the metals can be found by comparing the binding energies to literature values. The oxidation state of each metal is shown in Table 4-1. These results indicate the metals are primarily in an oxide form, and this is not surprising since all the catalysts analyzed were calcined in air prior to XPS analysis. It would have been much more useful to perform XPS on the reduced catalysts. Unfortunately, the required XPS parts were not available to perform the reduction on the catalysts within the XPS.

The nickel and copper metal loadings for the Ni/YSZ and Cu/YSZ catalysts examined by XPS are about 25 % lower compared to the theoretical copper and nickel loadings. On the other hand, the metal loading from the XPS showed a low concentration

for nickel and a high concentration for copper for the Ni/Cu/YSZ catalyst. High and low metal loadings of cobalt were found in the lithium cobalt oxide catalysts for preparation 1 and 2, respectively, and there was no evidence of any lithium in the lithium cobalt oxide catalysts. However, it should be noted that concentrations lower than 1 wt% can be difficult to detect by XPS.

Table 4-1. Metal Compositions and Oxidation States Determined from XPS.

Catalyst	Prepared Metal Loading (wt %)	XPS Metal Loading (wt %)	Oxidation State
Ni/YSZ	7.2	5.4	Ni <sup>2+</sup>
Cu/YSZ	9.8	7.1	Cu <sup>2+</sup>
Ni/Cu/YSZ	3.5 (Ni amt.)	0.84	Ni <sup>2+</sup>
	3.9 (Cu amt.)	5.5	Cu <sup>2+</sup>
LiCoO <sub>2</sub> /YSZ prep 1.	0.6 (Li amt.)	0	N/A
	4.9 (Co amt.)	7.92	Co <sup>2+</sup>
LiCoO <sub>2</sub> /YSZ prep 2.	0.6 (Li amt.)	0	N/A
	4.9 (Co amt.)	1.28	Co <sup>2+</sup>

## 4.2 BET Surface Area Characterization

The BET surface area measurements were performed using the AutoChem II 2920, which yields the total surface area of the support (YSZ) and metal. The BET surface area measurements for the five reduced catalysts are shown in Table 4-2. In Equation (3-2), the slope and intercept can be obtained by plotting the left hand side of Equation (3-2) as a function of  $x$  ( $P/P_0$ ). The slope and intercept were subsequently used to calculate the BET surface area. The surface areas reported are for 3-point BET analysis (10, 20, and 30 % nitrogen). The multipoint BET measurements produced very good linearity between all three data points for each catalyst. The Ni/YSZ catalyst resulted in the highest surface area compared to the other four catalysts, whereas the copper catalyst produced the lowest surface area. In addition, the BET surface area was also measured on the YSZ support. The surface area of YSZ is reported to be  $7 \pm 2$  m<sup>2</sup>/g ([www.tosoh.com](http://www.tosoh.com)), and the present measurements determined a value of 12 m<sup>2</sup>/g.

Table 4-2. Multipoint BET Surface Area Measurements

Catalyst	Surface Area (m <sup>2</sup> /g)
YSZ	12.0
Ni/YSZ	8.5
Cu/YSZ	4.9
Ni/Cu/YSZ	5.3
LiCoO <sub>2</sub> Prep.1	6.1
LiCoO <sub>2</sub> Prep.2	5.7

### 4.3 Anode Material Reaction Analysis on Methane Oxidation

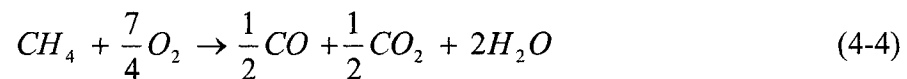
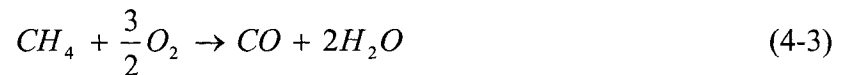
#### 4.3.1 Calculating Methane Conversion

Methane oxidation reactions were performed on the five different catalysts at 500, 600, 700, and 800 °C in the absence and presence of H<sub>2</sub>S. These reactions were carried out in various mixtures of oxygen and methane (Periods A to E), as shown in Table 3-3. Methane conversion is the ratio of the total amount of methane that reacts over the initial amount of methane or the total amount of products from the reaction. The methane conversion can be calculated using Equations (4-1) and (4-2) as shown below.

$$X_{CH_4} = \frac{(P_{CH_4})_{inlet} - (P_{CH_4})_{outlet}}{(P_{CH_4})_{inlet}} \quad (4-1)$$

$$X_{CH_4} = \frac{P_{CO} + P_{CO_2}}{P_{CO} + P_{CO_2} + P_{CH_4,outlet}} \quad (4-2)$$

where  $P$  is the partial pressure of the component as determined by the mass spectrometer. The peak intensities obtained from the mass spectrometer are assumed to be proportional to the partial pressures due to the assumption that the gases are ideal gases, and thus, the partial pressures are also proportional to the concentration. Complete combustion of methane should result in mainly  $CO_2$  (Eq.3-6). On the other hand, partial oxidation of methane would produce  $CO$  and/or  $CO_2$ , shown by Equation (4-3) and (4-4), respectively.



Equation (4-2) was used to calculate the methane conversions with the exception of the reaction on the nickel catalyst exposed in  $H_2S$ , in which Equation (4-1) was used. In this case, Equation (4-2) could not be used due to the unstable production of  $CO_2$ . It is important to note that Equation (4-2) does not take into account carbon formation. On

the other hand, Equation (4-1) does take carbon deposition into account because it involves inlet and outlet concentrations of methane. One drawback in using Equation (4-1) is that relative partial pressures of methane from the mass spectrometer are used and not the absolute values. Thus, variation in methane partial pressures would result in some error in calculating the methane conversion.

#### **4.3.2 Methane Conversion Results on Catalysts Performed without H<sub>2</sub>S**

The methane conversions for the five catalysts at the four temperatures exposed without H<sub>2</sub>S for Periods A to D are shown in Figures 4-1, 4-2, 4-3 and 4-4, respectively. Methane conversion was highest in Period A for all operating temperatures, as expected, because Period A contains the largest amount of oxygen (2:1; O<sub>2</sub>:CH<sub>4</sub>) available for methane oxidation. As the experiment proceeds from Period A thru Period D (decreasing oxygen concentration), the methane conversion results in a decreasing trend. Interestingly, the Ni/YSZ catalyst produced very high methane conversions (~97%) compared to the other catalysts for Period A, B and C at 700 and 800 °C. Even at 600 °C, the Ni/YSZ catalyst produced high reactivity for Period A, B and C (>80%). Methane conversions for the Ni/YSZ catalyst (>500 °C) for Period D were not reported, since the intensities of methane (outlet) from the mass spectrometer were not stable in this region, possibly due to carbon adsorption onto the catalyst surface. Overall, the methane reactivity based on the methane conversion data was highest for Ni/YSZ followed by Ni/Cu/YSZ, Cu/YSZ then the LiCoO<sub>2</sub>/YSZ catalysts, respectively. For example, the methane conversions for Ni/YSZ, Ni/Cu/YSZ, Cu/YSZ and LiCoO<sub>2</sub>/YSZ catalysts (preparation 1 and 2) at 700 °C for Period C were 94%, 74%, 32%, 31% and 31%,



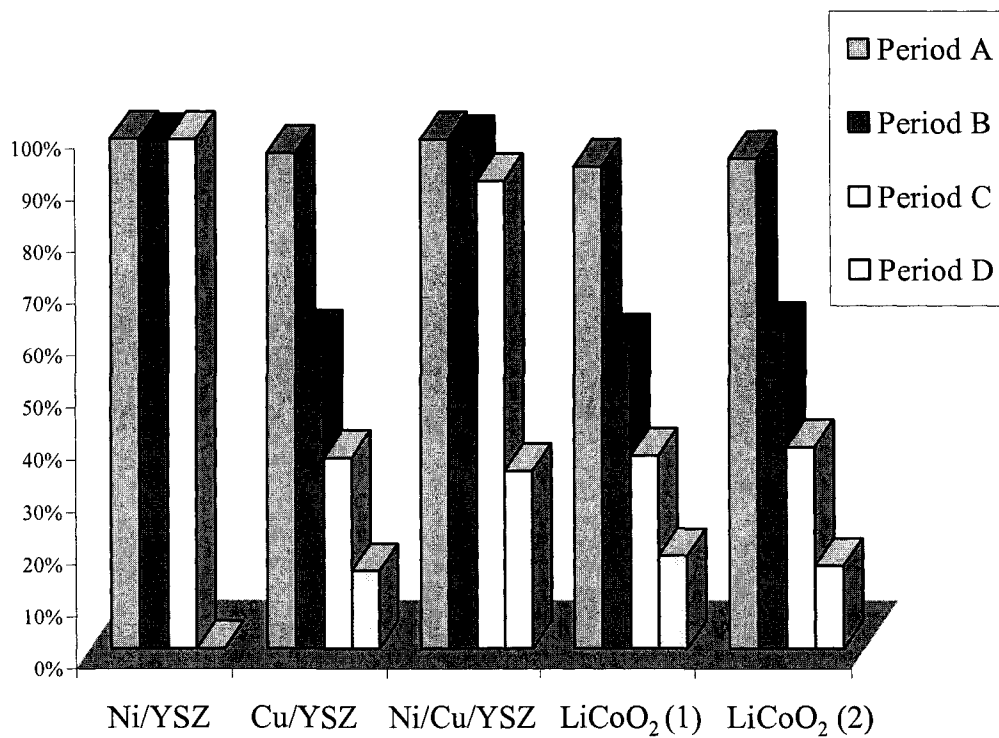


Figure 4-1. Methane Conversion at 800 °C (H<sub>2</sub>S-free)

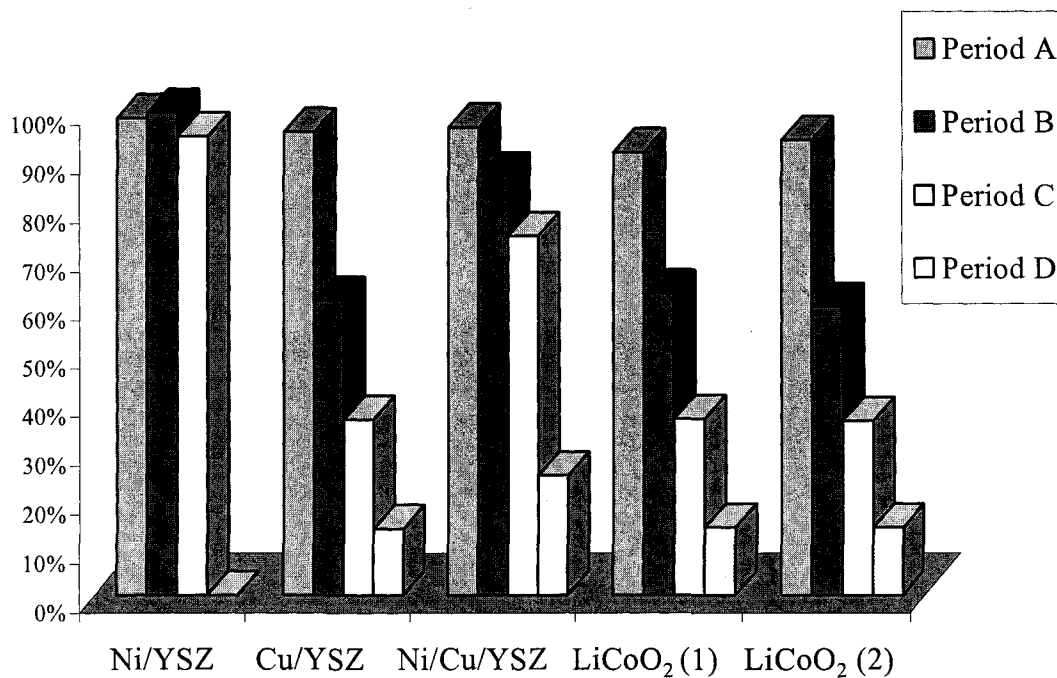


Figure 4-2. Methane Conversion at 700 °C (H<sub>2</sub>S-free).

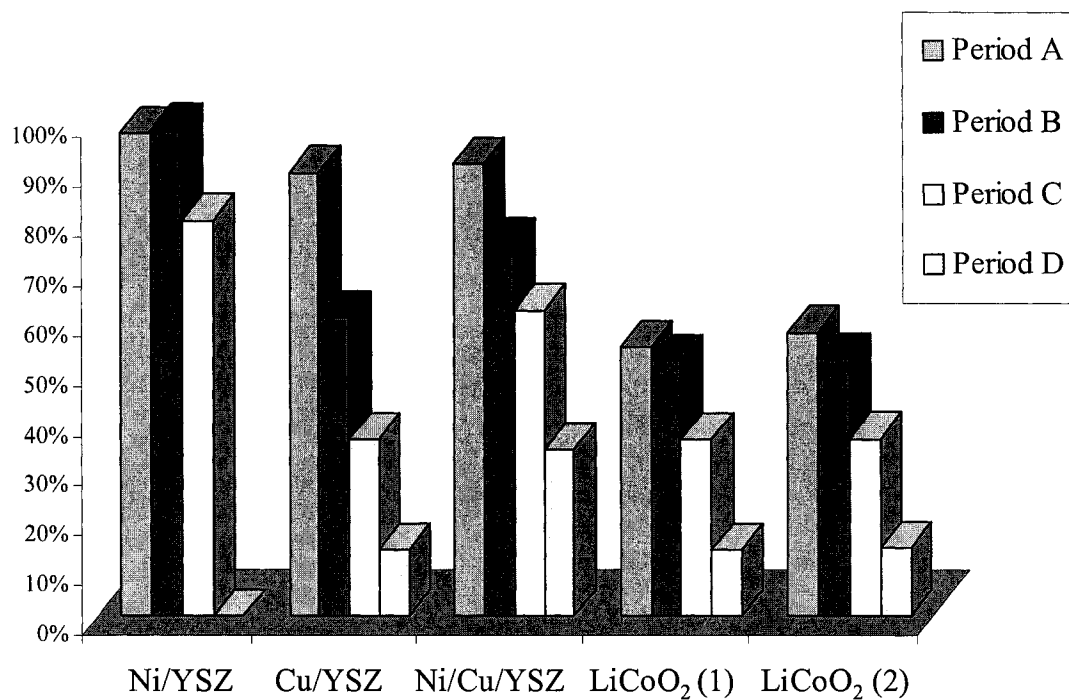


Figure 4-3. Methane Conversion at 600 °C (H<sub>2</sub>S-free).

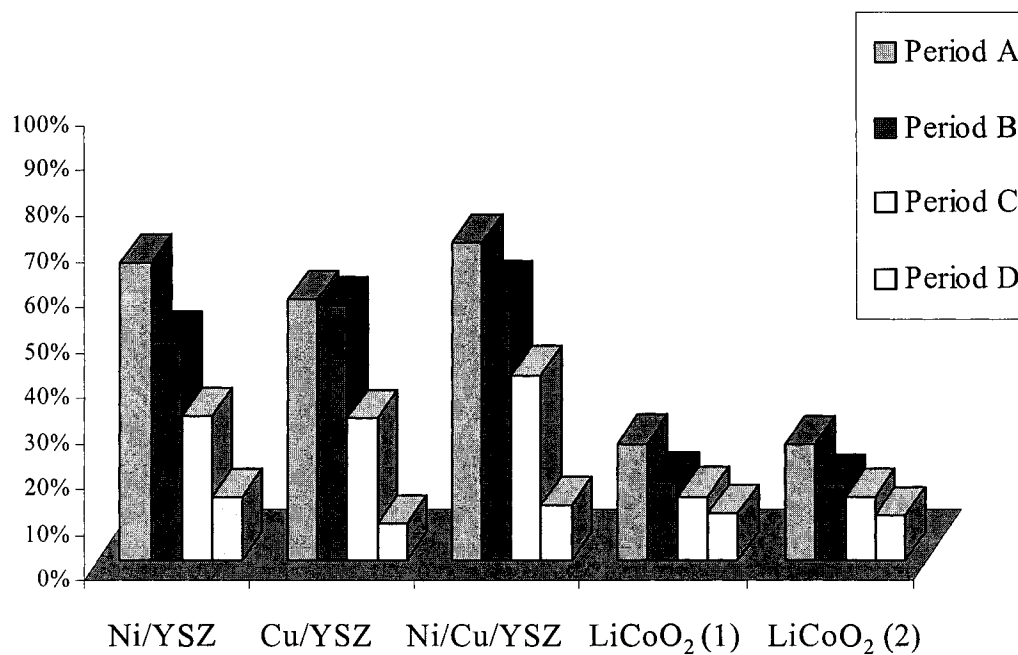


Figure 4-4. Methane Conversion at 500 °C (H<sub>2</sub>S-free).

respectively. Following Period D, the gas composition was returned to stoichiometric levels of methane and oxygen for complete combustion (Period E). This was done to determine if the catalyst exhibits deactivation or degradation, which will be discussed later by the CO<sub>2</sub> selectivity results. Generally, all the catalysts studied resulted in a relatively small methane conversion difference between Period A and E.

#### **4.3.3 Methane Conversion Results run in the presence of H<sub>2</sub>S**

The methane conversions for the five catalysts at the four temperatures exposed in H<sub>2</sub>S for Periods A to D are illustrated in Figures 4-5, 4-6, 4-7 and 4-8, respectively. The Ni/YSZ appeared to be the least reactive towards methane oxidation throughout all periods at all operating temperatures compared to the other catalysts, while Cu/YSZ produced the highest reactivity based on the methane conversion data. For example, methane conversions for Ni/YSZ, Ni/Cu/YSZ, Cu/YSZ and LiCoO<sub>2</sub>/YSZ (preparation 1 and 2) catalysts at 700 °C for Period C were 16%, 37%, 41%, 33% and 33%, respectively. The methane conversion difference for most of the catalysts between Period A and E are much smaller at 800 °C compared to the difference at 500 °C. For example, the nickel catalyst resulted in a 7% and 32% methane conversion difference between Period A and E at 800 and 500 °C, respectively. However, the LiCoO<sub>2</sub>/YSZ catalysts resulted in small changes in methane conversion between Period A and E at all operating temperatures. This indicates that the LiCoO<sub>2</sub>/YSZ catalysts were able to generate the same methane conversions when exposed in an oxygen deficient environment (Period B to D) and then re-exposed to a stoichiometric amount of oxygen (Period E).



Figure 4-5. Methane Conversion at 800 °C (in H<sub>2</sub>S).

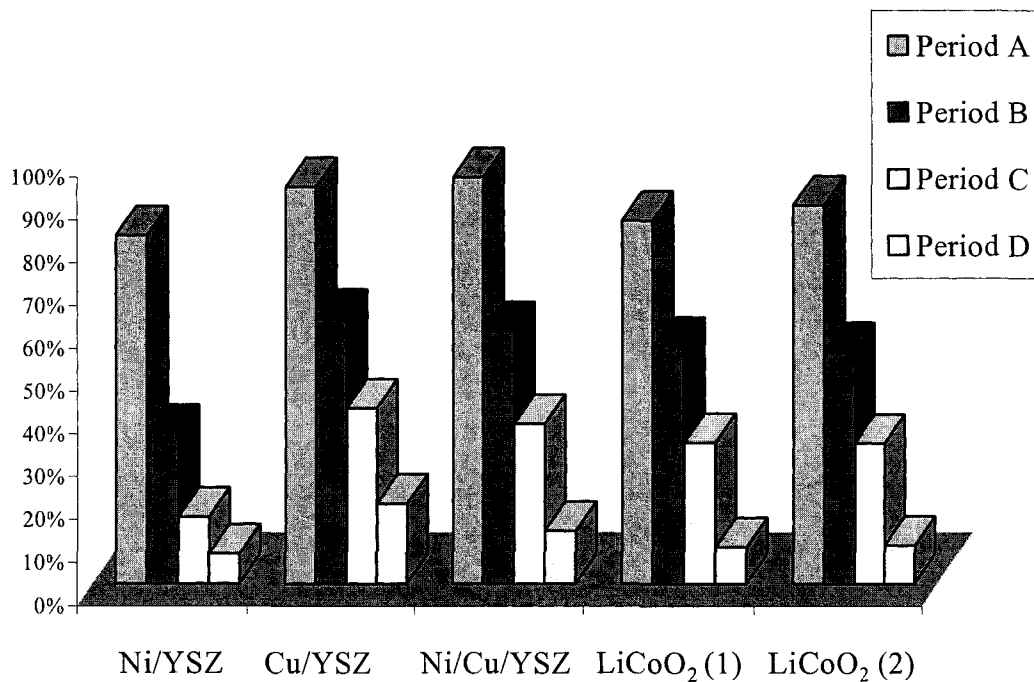


Figure 4-6. Methane Conversion at 700 °C (in H<sub>2</sub>S).

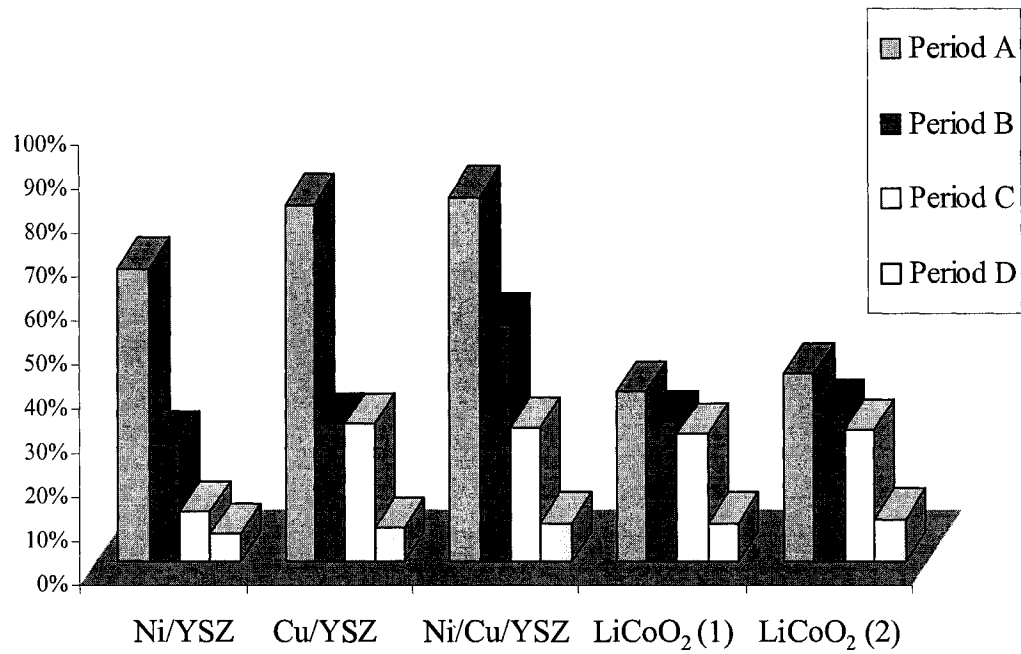


Figure 4-7. Methane Conversion at 600 °C (in H<sub>2</sub>S).

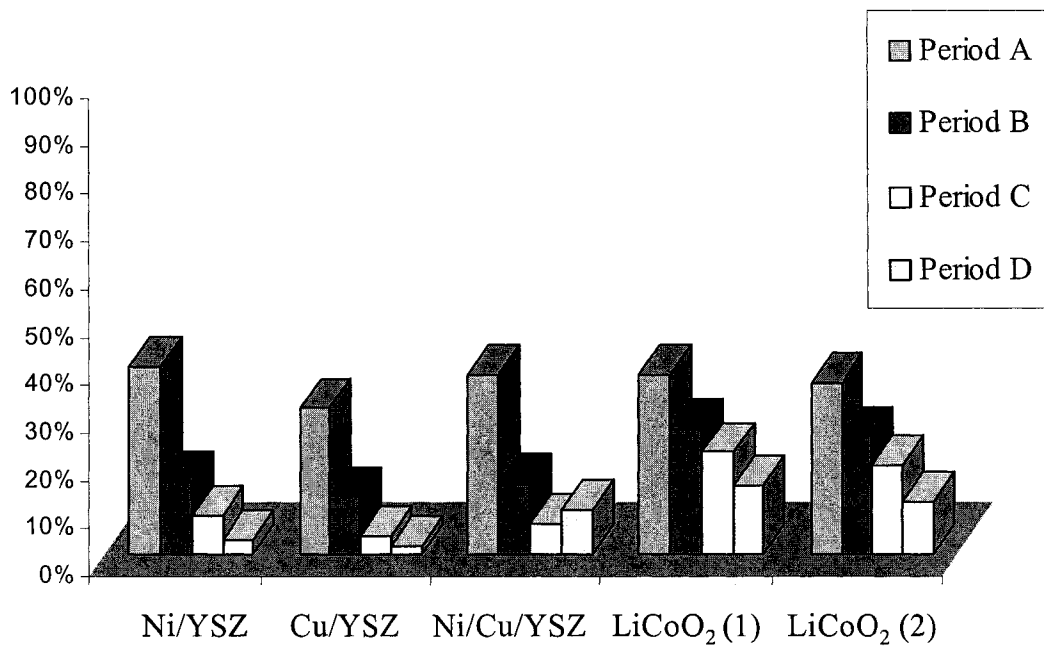


Figure 4-8. Methane Conversion at 500 °C (in H<sub>2</sub>S).

It is important to note that the error involved in calculating the methane conversions would be approximately 10%. This error would include a combination of the instrumental error by the mass spectrometer (~ 10%) and the standard deviation from the partial pressure readings. The partial pressure readings from the mass spectrometer of the product gases are approximately  $\pm 2.5\%$ .

#### 4.3.4 CO<sub>2</sub> Selectivity Results

The CO<sub>2</sub> selectivity for each reaction and catalyst was calculated using Equation (4-5). The partial pressures of the product gases were obtained using the relative peak intensities from the mass spectrometer. The error in calculating the CO<sub>2</sub> selectivity is approximately 10%, which is similar to the errors in the methane conversion data.

$$S_{CO_2} = \frac{P_{CO_2}}{P_{CO_2} + P_{CO}} \quad (4-5)$$

##### 4.3.4.1 CO<sub>2</sub> Selectivity Results for Catalysts in an H<sub>2</sub>S-free Environment

The CO<sub>2</sub> selectivity for the five catalysts exposed without the presence of H<sub>2</sub>S from Periods A to E is presented in Table 4-3. The CO<sub>2</sub> selectivity for Period A produced the highest selectivity towards CO<sub>2</sub> which is not surprising since Period A provides the stoichiometric amount of oxygen (most oxygen available) required to fully combust methane. Since the oxygen levels are decreased from Period A thru D, it is also expected that the selectivity for CO<sub>2</sub> should decrease. Surprisingly, CO<sub>2</sub> selectivity was found highest at 700 °C for Period A for all the catalysts. The Ni/YSZ and Ni/Cu/YSZ showed a dramatic decrease in CO<sub>2</sub> selectivity between Period A and D at temperatures

above 500 °C, whereas the other catalysts only showed a gradual decreasing trend, as shown by Table 4-3. The CO<sub>2</sub> selectivity values for the Ni/YSZ and Ni/Cu/YSZ performed without H<sub>2</sub>S in Period D were less than 0.08 for operating temperatures greater than 500 °C.

Table 4-3. CO<sub>2</sub> Selectivity Results for Catalysts in an H<sub>2</sub>S-free Environment

Catalyst	Temp (°C)	Period A	Period B	Period C	Period D	Period E
Ni/YSZ	800	0.792	0.250	0.010	0.010	0.010
Ni/YSZ	700	0.797	0.298	0.0365	0.012	0.053
Ni/YSZ	600	0.743	0.358	0.117	0.038	0.303
Ni/YSZ	500	0.709	0.725	0.698	0.488	0.706
Cu/YSZ	800	0.802	0.762	0.705	0.465	0.801
Cu/YSZ	700	0.833	0.802	0.755	0.519	0.831
Cu/YSZ	600	0.821	0.807	0.755	0.530	0.821
Cu/YSZ	500	0.741	0.808	0.762	0.540	0.747
LiCoO <sub>2</sub> (1)	800	0.750	0.715	0.635	0.290	0.775
LiCoO <sub>2</sub> (1)	700	0.814	0.794	0.744	0.513	0.817
LiCoO <sub>2</sub> (1)	600	0.687	0.768	0.753	0.524	0.714
LiCoO <sub>2</sub> (1)	500	0.319	0.386	0.416	0.389	0.296
LiCoO <sub>2</sub> (2)	800	0.806	0.766	0.705	0.435	0.802
LiCoO <sub>2</sub> (2)	700	0.826	0.795	0.741	0.517	0.822
LiCoO <sub>2</sub> (2)	600	0.709	0.773	0.758	0.526	0.708
LiCoO <sub>2</sub> (2)	500	0.314	0.367	0.388	0.364	0.282
Cu/Ni/YSZ	800	0.620	0.253	0.0225	0.036	0.610
Cu/Ni/YSZ	700	0.769	0.433	0.152	0.046	0.796
Cu/Ni/YSZ	600	0.729	0.577	0.365	0.075	0.718
Cu/Ni/YSZ	500	0.620	0.514	0.442	0.117	0.620

#### 4.3.4.2 CO<sub>2</sub> Selectivity Results for Catalysts in an H<sub>2</sub>S Environment

The selectivity for CO<sub>2</sub> did not show a significant difference between Period A and E for the LiCoO<sub>2</sub>/YSZ catalysts and the Ni/YSZ, Ni/Cu/YSZ and Cu/YSZ catalysts operated at 700 and 800 °C. On the other hand, the selectivity of CO<sub>2</sub> for Ni/YSZ, Cu/YSZ and Ni/Cu/YSZ produced significantly low values in Period E (less than 0.1) at 500 °C, compared to the values in Period A, shown in Table 4-4. The CO<sub>2</sub> selectivity values were approximately 0.4 for Period D at temperatures above 500 °C for Ni/YSZ and Ni/Cu/YSZ. The missing CO<sub>2</sub> selectivity values indicated in Table 4-4 for Ni/YSZ, Cu/YSZ and Ni/Cu/YSZ could not be obtained due to the unstable production of CO<sub>2</sub> (decreasing levels).



Table 4-4. CO<sub>2</sub> Selectivity Results for Catalysts in an H<sub>2</sub>S Environment.

Catalyst	Temp ( °C)	Period A	Period B	Period C	Period D	Period E
Ni/YSZ	800	0.625	N/A	0.480	0.200	0.640
Ni/YSZ	700	0.768	0.740	0.683	0.405	0.730
Ni/YSZ	600	0.750	0.730	0.600	0.425	0.500
Ni/YSZ	500	0.520	N/A	N/A	N/A	0.100
Cu/YSZ	800	0.800	0.750	0.685	0.382	0.807
Cu/YSZ	700	0.647	0.585	0.510	0.244	0.650
Cu/YSZ	600	0.645	0.642	0.565	0.300	0.340
Cu/YSZ	500	0.6	N/A	N/A	0.164	0.095
LiCoO <sub>2</sub> (1)	800	0.652	0.590	0.500	0.216	0.655
LiCoO <sub>2</sub> (1)	700	0.777	0.763	0.705	0.438	0.780
LiCoO <sub>2</sub> (1)	600	0.550	0.637	0.678	0.445	0.552
LiCoO <sub>2</sub> (1)	500	0.127	0.184	0.21	0.219	0.116
LiCoO <sub>2</sub> (2)	800	0.805	0.755	0.675	0.36	0.800
LiCoO <sub>2</sub> (2)	700	0.790	0.758	0.696	0.423	0.776
LiCoO <sub>2</sub> (2)	600	0.521	0.618	0.653	0.421	0.531
LiCoO <sub>2</sub> (2)	500	0.221	0.278	0.300	0.270	0.1803
Cu/Ni/YSZ	800	0.825	0.783	0.715	0.395	0.832
Cu/Ni/YSZ	700	0.739	0.690	0.670	0.345	0.730
Cu/Ni/YSZ	600	0.800	0.783	0.740	0.487	0.580
Cu/Ni/YSZ	500	0.633	N/A	N/A	0.170	0.090

### 4.3.5 Catalyst Degradation

The deactivation of the catalysts was investigated by calculating the CO<sub>2</sub> selectivity change between Period A and E. Periods A and E exhibit the same methane and oxygen gas compositions used for methane oxidation reactions on all the catalysts. The percent difference in CO<sub>2</sub> selectivity between Period A and E is defined by Equation (4-6). The percent changes in CO<sub>2</sub> selectivity between Period A and E for the catalysts run without H<sub>2</sub>S and with H<sub>2</sub>S are illustrated in Figures 4-9 and 4-10, respectively.

$$\% \Delta S_{CO_2} = \left( \frac{S_{CO_2,A} - S_{CO_2,E}}{S_{CO_2,A}} \right) \times 100 \quad (4-6)$$

The change in selectivity of CO<sub>2</sub> between Period A and E was small (< 5%) for all of the catalysts without H<sub>2</sub>S, with the exception of the Ni/YSZ catalyst at temperatures above 500 °C. The difference in values was as high as 98% for Ni/YSZ at 800 °C and still high (60%) even at 600 °C. Interestingly, the Ni/YSZ, Ni/Cu/YSZ and Cu/YSZ catalysts exposed to H<sub>2</sub>S gave opposite results compared to those performed without H<sub>2</sub>S. This was shown by the increase in selectivity change between Period A and E at 500 and 600 °C. The Ni/YSZ, Cu/YSZ and Ni/Cu/YSZ catalysts reached up to an 85% change in CO<sub>2</sub> selectivity between Periods A and E at 500 °C. This demonstrates that these catalysts exhibit degradation more severely at the lower temperatures under the influence of H<sub>2</sub>S. The LiCoO<sub>2</sub>/YSZ catalysts showed less change (~15%) in CO<sub>2</sub> selectivity at 500 °C compared to the rest of the catalysts exposed in H<sub>2</sub>S. Thus, the LiCoO<sub>2</sub>/YSZ catalysts did not appear to be affected by H<sub>2</sub>S at all operating temperatures.

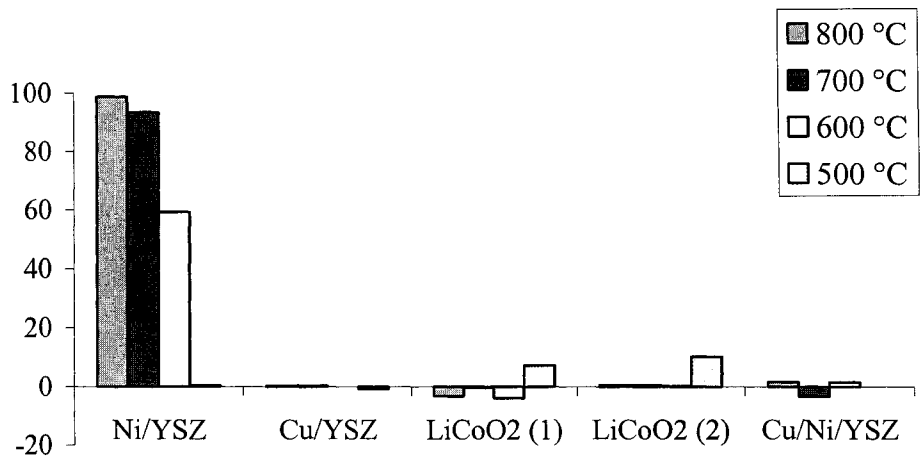


Figure 4-9. Percent Change in CO<sub>2</sub> Selectivity between Period A and E for Catalysts exposed without H<sub>2</sub>S.

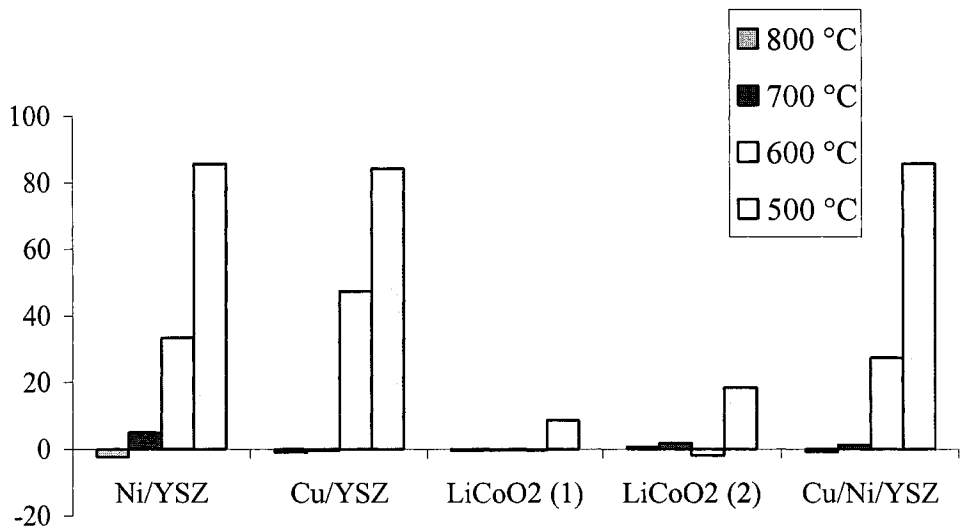


Figure 4-10. Percent Change in CO<sub>2</sub> Selectivity between Period A and E for Catalysts exposed with H<sub>2</sub>S.

#### 4.4 Methane Oxidation Reaction Kinetic Analysis

The investigation on the reaction kinetics involving methane oxidation on the five catalysts in both an H<sub>2</sub>S-free and in a H<sub>2</sub>S environment was analyzed by fitting the experimental data into the combined power law and the use of Arrhenius relationship as shown by Equation (4-7).

$$(-r_{CH_4}) = kC_{CH_4}^{\alpha}C_{O_2}^{\beta} = \left[ A \exp\left(\frac{-E_a}{RT}\right) \right] C_{CH_4,Avg}^{\alpha} C_{O_2,Avg}^{\beta} \quad (4-7)$$

where  $(-r_{CH_4})$  is the rate of disappearance of methane,  $k$  is the rate constant,  $C$  is the concentration, and  $A$  and  $E_a$  are the pre-exponential factor and the activation energy, respectively. The reaction order of methane and oxygen are represented by  $\alpha$  and  $\beta$ , respectively. The rate of methane disappearance was calculated using Equation (4-8).

$$(-r_{CH_4}) = \frac{F_{CH_4,initial} dX_{CH_4}}{M} \quad (4-8)$$

where  $F$  is the molar flow rate of the initial methane gas entering the reactor,  $dX_{CH_4}$  is the change in methane conversion between the inlet and outlet reactor conditions and  $M$  is the total mass of the catalyst used in the reaction. The average concentrations of methane and oxygen and the difference in methane conversion between the inlet and outlet reactor conditions were obtained by assuming that the experimental reactions follow a differential reactor. The four unknown parameters from Equation (4-7) are the pre-exponential factor, reaction order of methane ( $\alpha$ ) and oxygen ( $\beta$ ) and the activation

energy ( $E_a$ ). The unknown four parameters were determined by solving a set of non-linear equations and using the experimental rate of methane disappearance, average concentrations of methane and oxygen and temperature of the reaction. Thus, there was a set of 16 non-linear equations for each catalyst involving the methane oxidation reactions for Periods A thru D at the four different temperatures.

#### **4.4.1 Reaction Kinetic Parameters for the Catalysts without H<sub>2</sub>S**

The pre-exponential factor, reaction orders for methane and oxygen and the activation energy were determined and are presented in Table 4-5. The Ni/YSZ catalyst produced the highest pre-exponential factor, while Cu/YSZ resulted in the lowest value. The pre-exponential factor for Ni/YSZ was 18 times higher than the value for Cu/YSZ. This demonstrates the high reactivity of nickel compared to the other catalysts. This was verified by the high methane conversions observed with the nickel catalyst even at low temperatures ( $> 500$  °C). The activation energy was highest for the Ni/YSZ catalyst, next to the LiCoO<sub>2</sub>/YSZ catalysts and lowest for Cu/YSZ. Catalysts that exhibit high activation energies require high operating temperatures to produce an active catalyst. For example, Ni/YSZ produced a high and low rate of methane disappearance of  $2.4 \times 10^{-4}$  and  $6.9 \times 10^{-5}$  mol/min g metal at 800 °C and 500 °C, respectively, at a methane partial pressure of approximately 6.5 kPa. The dependence of methane is stronger than that of oxygen for the Ni/YSZ catalyst (without H<sub>2</sub>S). On the other hand, the other four catalysts evidenced a stronger dependence on oxygen (higher  $\beta$ ), shown by Table 4-5.

#### 4.4.2 Reaction Kinetic Parameters for the Catalysts in the Presence of H<sub>2</sub>S

The pre-exponential factor, reaction orders for methane and oxygen and the activation energy were determined and are presented in Table 4-6. Interestingly, the Ni/YSZ catalyst showed the lowest values for both  $A$  and  $E_a$ , while Cu/YSZ resulted in the highest values. The activation energies for all of the catalysts with the exception of the Ni/YSZ catalyst were fairly high. Therefore, the catalysts that exhibit high activation energies require high operating temperatures to become active in an H<sub>2</sub>S atmosphere. All of the catalysts showed higher dependence of oxygen compared to methane. Surprisingly, the order of methane was a negative (-0.19) for Ni/YSZ, demonstrating the decreasing rate of methane disappearance as methane/H<sub>2</sub>S concentration increases.

Table 4-5. Reaction parameters for methane oxidation on catalysts exposed without H<sub>2</sub>S.

Catalyst	A	$\alpha$	$\beta$	$E_a$ (kJ/mol)
Ni/YSZ	3.2 E-3	0.98	0.76	32.5
Cu/YSZ	1.8 E-4	0.36	0.77	11.3
Ni/Cu/YSZ	4.2 E-4	1.18	1.39	20.2
LiCoO <sub>2</sub> prep 1.	1.7 E-3	0.21	0.58	29.1
LiCoO <sub>2</sub> prep 2.	2.1 E-3	0.23	0.59	30.6

Table 4-6. Reaction parameters for methane oxidation on catalysts exposed in H<sub>2</sub>S.

Catalyst	A	$\alpha$	$\beta$	E <sub>a</sub> (kJ/mol)
Ni/YSZ	7.9 E-4	-0.19	0.25	21.4
Cu/YSZ	4.5E-3	0.19	0.25	34.2
Ni/Cu/YSZ	1.6E-3	0.29	0.60	27.4
LiCoO <sub>2</sub> prep 1.	2.4E-3	0.37	0.62	32.9
LiCoO <sub>2</sub> prep 2.	1.5E-3	0.30	0.65	28.5

#### 4.4.3. Rate of Disappearance of Methane as a Function of Methane Partial Pressure for the Catalysts in an H<sub>2</sub>S-free Environment

The reaction kinetics of methane oxidation was also illustrated by the rate of methane disappearance as a function of methane partial pressure, which is summarized in Figures 4-11, 4-12, 4-13, 4-14 and 4-15. The rate of disappearance of methane as a function of methane partial pressure should increase with temperature, which is observed with all the catalysts. Figure 4-11 shows an increasing rate of methane disappearance,  $-r_{\text{CH}_4}$ , with respect to increasing methane concentration for temperatures above 500 °C. However, at 500 °C, the rate of methane disappearance stays almost constant with increasing methane partial pressure. Therefore, the use of Ni/YSZ is not recommended at lower temperatures due to poor activity, which was evident by the large activation energy, as discussed earlier. Ni/YSZ produces the largest overall methane uptake as a function of methane partial pressure compared to the other catalysts, as illustrated by

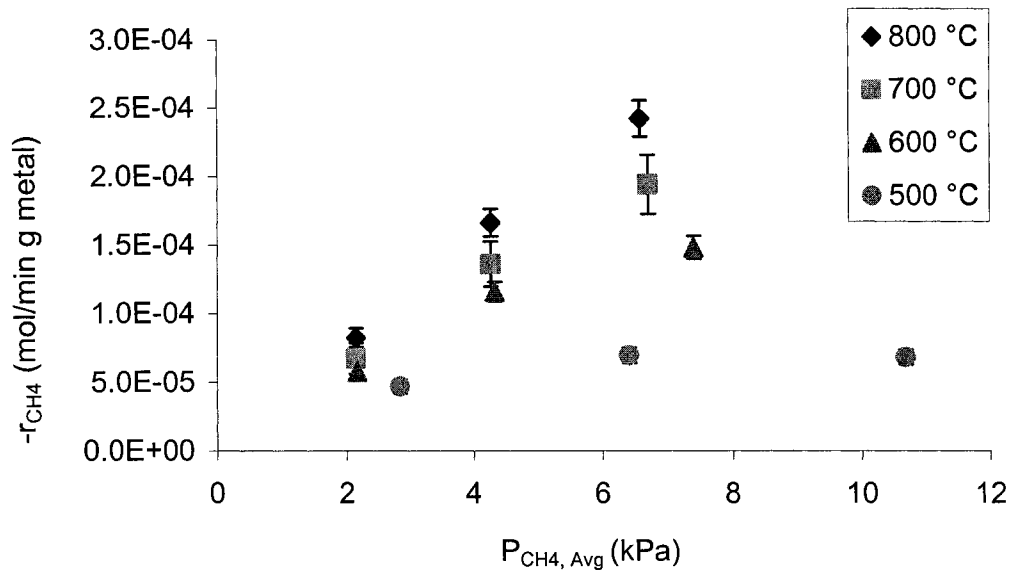


Figure 4-11. Rate of methane disappearance as a function of methane partial pressure for Ni/YSZ (H<sub>2</sub>S-free).

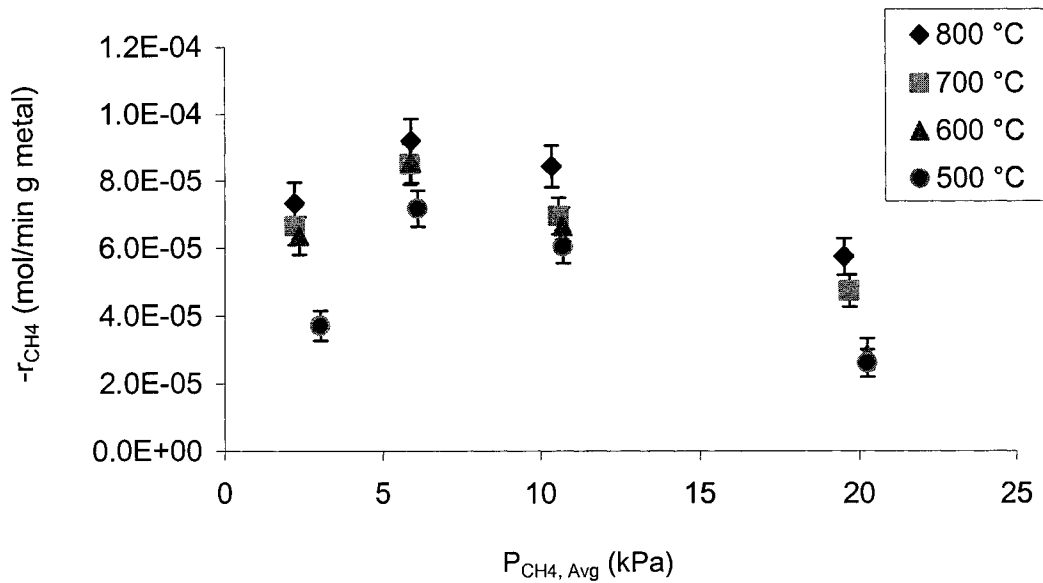


Figure 4-12. Rate of methane disappearance as a function of methane partial pressure for Cu/YSZ (H<sub>2</sub>S-free).



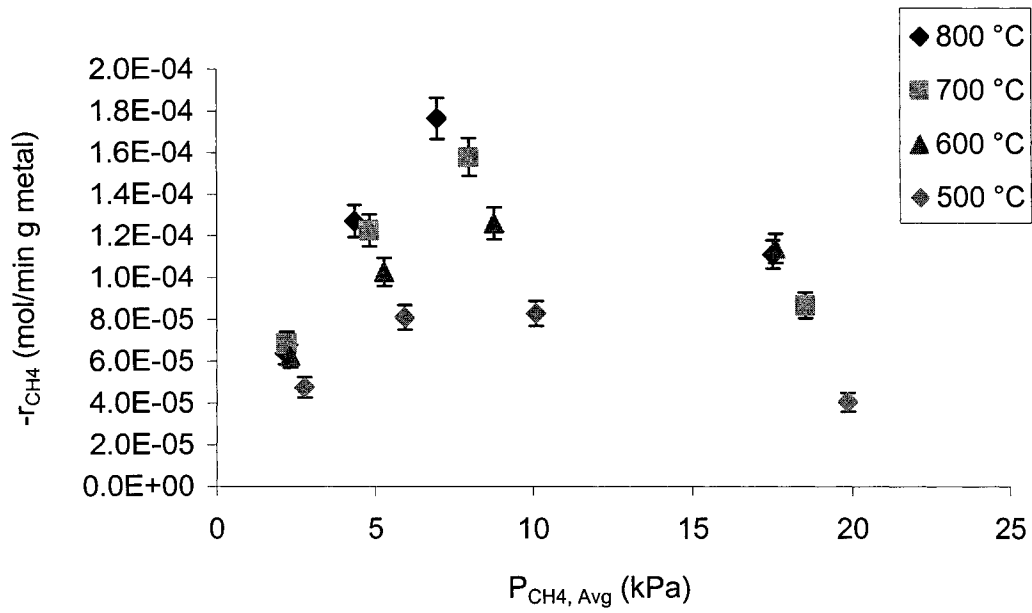


Figure 4-13. Rate of methane disappearance as a function of methane partial pressure for Ni/Cu/YSZ ( $H_2S$ -free).

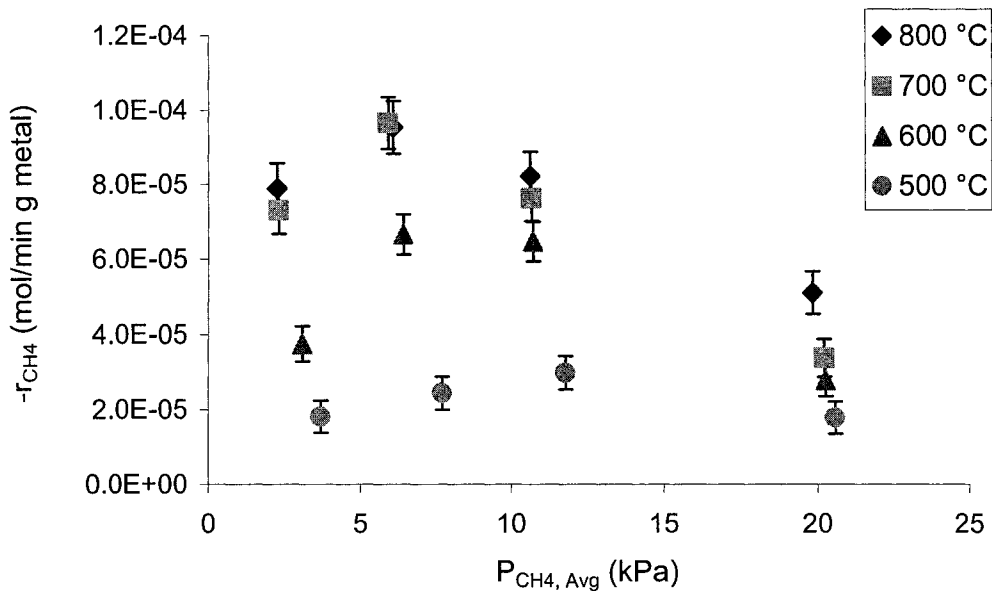


Figure 4-14. Rate of methane disappearance as a function of methane partial pressure for  $LiCoO_2$  Prep 1 ( $H_2S$ -free).

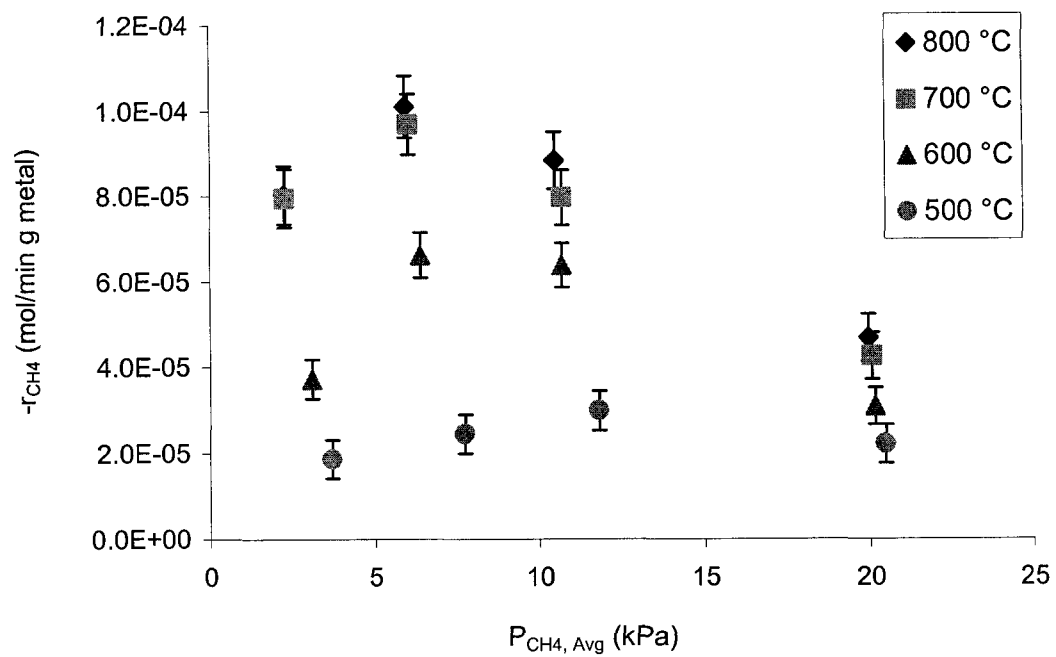


Figure 4-15. Rate of methane disappearance as a function of methane partial pressure for LiCoO<sub>2</sub> Prep 2 (H<sub>2</sub>S-free).

by Figure 4-11. Figure 4-13 demonstrates similar trends for Ni/Cu/YSZ compared to Ni/YSZ. It is important to note that at Period D ( $P_{CH_4} \sim 20$  kPa), the rate drops dramatically, as shown by Figure 4-13. The remaining catalysts (Cu/YSZ and LiCoO<sub>2</sub>/YSZ), showed an increasing rate of methane disappearance for the first two periods (A and B), and then decreases with increasing methane partial pressure (Period C and D). This indicates that the maximum partial pressure of methane was reached in which adsorption of methane is so strong that it prohibits adsorption of oxygen and thus retards the surface reaction. It is important to note that if methane partial pressure is increased, the reaction rate does not necessarily have to increase. For a certain value of methane partial pressure, there will be a maximum rate; above this pressure the rate will decrease with increasing methane partial pressure, which is evident for all of the catalysts, with the exception of the Ni/YSZ catalyst.

#### **4.4.4 Rate of Disappearance of Methane as a Function of Methane Partial Pressure for the Catalysts in an H<sub>2</sub>S Environment**

The rate of disappearance of methane as a function of methane partial pressure for the catalysts exposed in H<sub>2</sub>S is summarized in Figures 4-16, 4-17, 4-18, 4-19 and 4-20. The Ni/YSZ catalyst appeared to be poisoned by H<sub>2</sub>S the most compared to the other catalysts. This is illustrated by Figure 4-16, which shows the decreasing rate of methane uptake as methane concentration increases. When H<sub>2</sub>S is added to Ni/Cu/YSZ, the disappearance of methane increases slightly in the first two periods then begins to decrease at Periods C and D, while at 500 °C, the rate decreases throughout the entire reaction, as illustrated by Figure 4-18. Similar trends were observed for Cu/YSZ

compared to Ni/Cu/YSZ. As the temperature drops (500 and 600 °C), the rate of methane disappearance decreases with methane concentration for the Cu/YSZ catalyst. The LiCoO<sub>2</sub>/YSZ catalysts showed an increasing rate of methane uptake between Period A and B then starts to descend in Period C and D at the higher temperatures (700 and 800 °C). At 600 °C, the rate of disappearance of methane increases linearly until Period C, then starts to decrease, while at 500 °C, there does not appear to be a significant change in the methane uptake as methane concentration increases for the LiCoO<sub>2</sub>/YSZ catalysts.

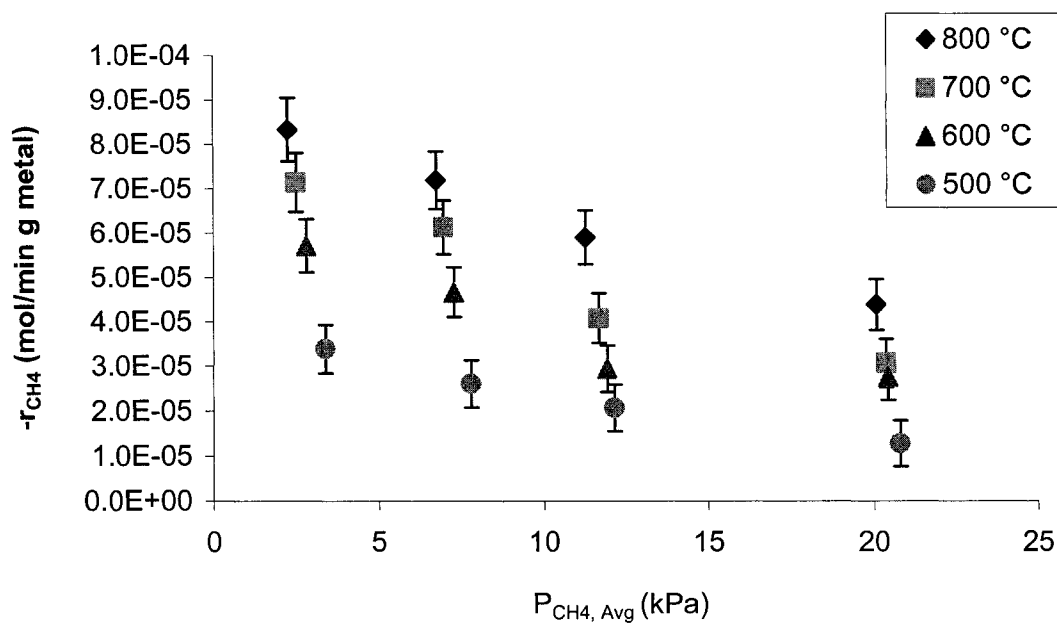


Figure 4-16. Rate of methane disappearance as a function of methane partial pressure for Ni/YSZ (H<sub>2</sub>S).

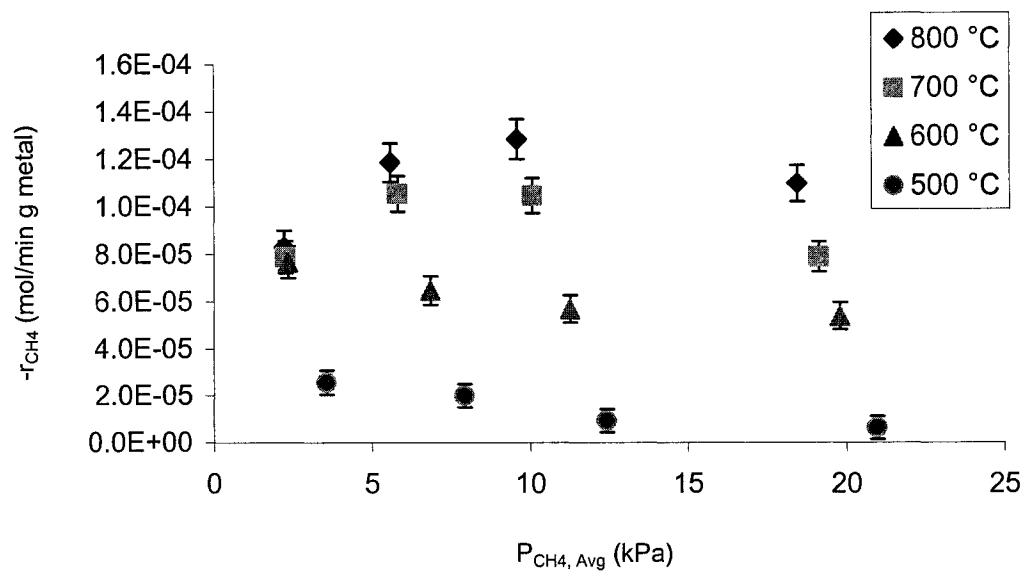


Figure 4-17. Rate of methane disappearance as a function of methane partial pressure for Cu/YSZ (H<sub>2</sub>S).

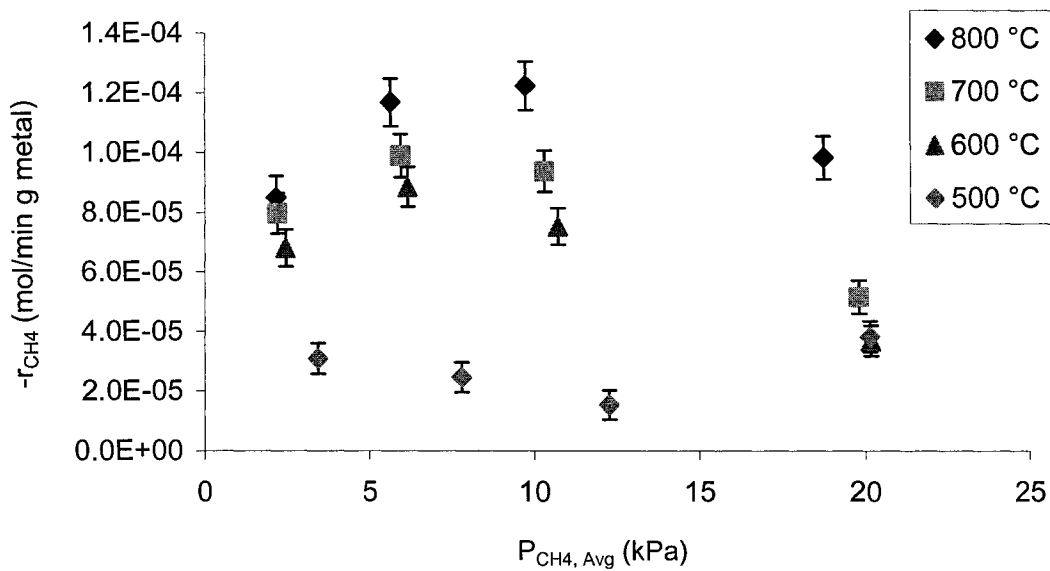


Figure 4-18. Rate of methane disappearance as a function of methane partial pressure for Ni/Cu/YSZ (H<sub>2</sub>S).

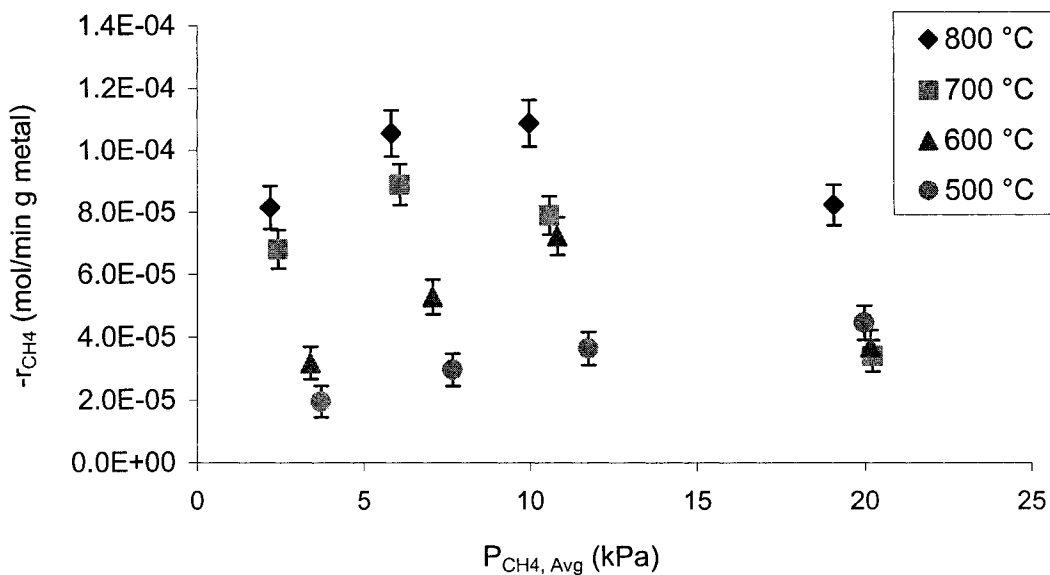


Figure 4-19. Rate of methane disappearance as a function of methane partial pressure for LiCoO<sub>2</sub> Preparation 1 (H<sub>2</sub>S).

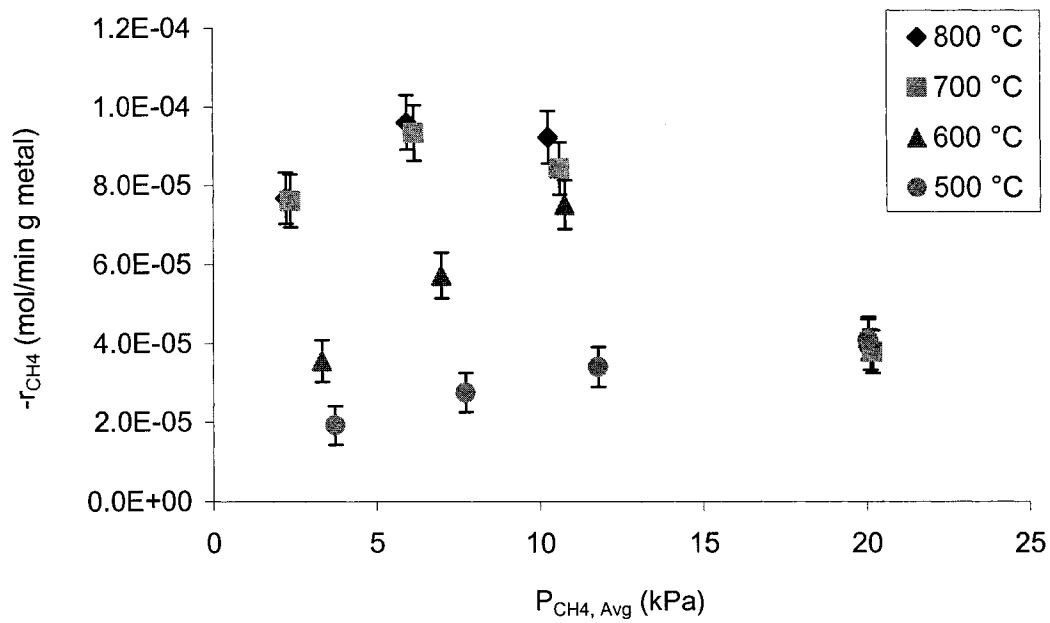


Figure 4-20. Rate of methane disappearance as a function of methane partial pressure for LiCoO<sub>2</sub> Preparation 2 (H<sub>2</sub>S).

## Chapter 5

### Discussion

#### 5.1 XPS Analysis and BET Surface Measurements

The metal loadings determined by the XPS are shown in Table 4-1 in the previous chapter. The Ni/YSZ and Cu/YSZ metal loadings are about 25 % lower compared to the target metal loadings. This could be caused by metal evaporation during the calcination process or the catalyst may not have formed uniform metal distribution throughout the catalyst. Wet impregnation methods for catalyst preparation may cause non-uniform metal distribution over the support. The adsorption of the nitrate solution in the YSZ support is governed by the porosity of the support, and the amount of active component incorporated in the catalyst depends on the solution concentration and its penetration into the support (Wijngaarden et al., 1998). For example, when the metal nitrate aqueous solution is created and mixed with the support, excess water solution may accumulate on top of the catalyst surface. This may produce excess metal distributed on the top layer of the catalyst during the drying process.

The Ni/Cu/YSZ catalyst showed a high metal loading of copper and a low metal loading of nickel. Impregnation with a multi-component solution may result in a more uneven distribution of components compared to a single metal component impregnation because of chromatographic effects (Wijngaarden et al., 1998). The more strongly adsorbed component will be deposited preferentially on the surface, whereas the weakly adsorbed metal will penetrate into the interior of the support (Wijngaarden et al., 1998). In this case, the nickel is the weakly adsorbed metal compared to the copper. Another



possible reason for the inconsistent XPS metal loadings may be due to the evaporation stage of the impregnated supports. The drying stage may change the distribution of the components, unless they are strongly adsorbed to the support. For example, evaporation starts at the surface of the catalyst and continues preferentially in the large pores, in which the vapor pressure is higher (Wijngaarden et al., 1998). If the drying process is slow and the nickel is soluble, the nickel is preferentially concentrated in the small pores in the center of the catalyst particle, where it later may not be accessible to the reactants.

In terms of the  $\text{LiCoO}_2/\text{YSZ}$  catalyst, there was no indication of any lithium in the sample using XPS. Surprisingly, there was a high and low cobalt loading for preparations 1 and 2, respectively. A possible reason for zero lithium loading in the catalyst could be related to the fact that only 0.6 weight percent (20 mole percent) was used. Thus, XPS was not able to detect any lithium metal or the small amount of lithium was not well distributed over the surface of the catalyst. It is important to note that concentrations lower than 1 wt% can be difficult to detect by XPS. The high and low cobalt loading is probably related to the solid-state reaction procedure. Preparation 1 for  $\text{LiCoO}_2/\text{YSZ}$  catalyst consists of a single calcination step, whereas preparation 2 consists of reacting the carbonates first, calcinations, and then adding the YSZ to the carbonates with a second calcination procedure. Thus, preparation 2 of the  $\text{LiCoO}_2/\text{YSZ}$  catalyst may have lost cobalt metal during the second calcination procedure, possibly due to evaporation of cobalt.

The BET surface area measurements show that  $\text{Ni}/\text{YSZ}$  catalyst exhibits the highest surface area compared to the other catalysts. Thus, nickel metal may be highly dispersed on the support, which allows the reactants to contact the metal surface more

readily, resulting in a more active catalyst. The Cu/YSZ catalyst showed the lowest surface area. Therefore, the copper metal was not well dispersed over the support but may have formed larger agglomerates of metal particles on the support. This may be caused by sintering of copper during the calcination process since copper is more likely to sinter due to its lower melting point (1083 °C) compared to nickel (1455 °C) (Spencer and Twigg., 2005). The lower surface area of Cu/YSZ results in a less active catalyst, which is evident by the reaction kinetics and methane conversion results. It is important to note that the surface area is not the main factor in determining the activity of the catalysts, but is only a small indication of the nature of the catalysts.

## **5.2 Methane Conversion and CO<sub>2</sub> Selectivity Analysis**

As seen in the previous chapter, methane conversion was highest for the Ni/YSZ catalyst without the influence of H<sub>2</sub>S, compared to the other four catalysts. Unfortunately, the Ni/YSZ catalyst exhibits catalyst degradation by carbon formation at temperatures above 500 °C. This was consistent with research by Mogensen and Kammer (2003). Indication of carbon formation on Ni/YSZ was evident from the dramatic decrease in CO<sub>2</sub> selectivity between Period A and C at temperatures above 500 °C. Moreover, it was evident in the large CO<sub>2</sub> selectivity change between Period A and E at temperatures above 500 °C. Thus, there was much more CO being produced compared to CO<sub>2</sub>. CO could then produce CO<sub>2</sub> and carbon, which was shown earlier from Equation (2-15). The other possible reaction that could cause the formation of carbon was shown by Equation (2-16). This involves methane decomposing into hydrogen and carbon. Carbon deposits on the nickel catalyst surface were also observed physically after the reaction was

performed and from the mass increase due the excess carbon formation on the catalyst surface. The other four catalysts (without H<sub>2</sub>S) did not exhibit signs of carbon formation.

Substitution of nickel with copper was shown to eliminate the formation of graphite for hydrocarbon fuels as demonstrated by Hyuk et al. (2001). As well, nickel/copper alloys as anodes for direct oxidation of methane at 800 °C had shown only small amounts of carbon formation and did not show signs of deactivation (Kim et al., 2002a). It is interesting to note that replacing nickel with cobalt led to similar catalytic properties to that of nickel and result in carbon pyrolysis (Gorte et al., 2000). Carbon formation was not evident for the LiCoO<sub>2</sub>/YSZ catalysts examined in this study, which contained mostly or almost all cobalt which was evident from the XPS results.

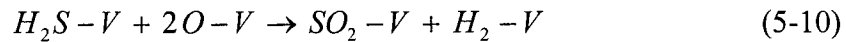
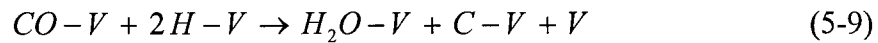
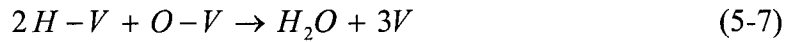
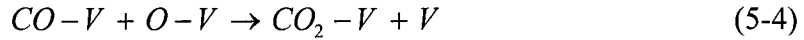
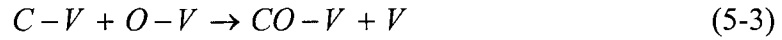
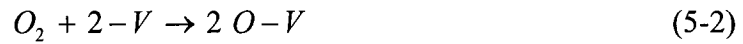
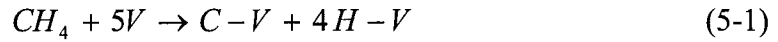
Carbon deposits were not observed on the Ni/YSZ catalyst when exposed in H<sub>2</sub>S. Therefore, carbon deposition was not a factor when using H<sub>2</sub>S, as seen by the small change in CO<sub>2</sub> selectivity and methane conversions between Period A and E at 700 and 800 °C. Surprisingly, there was a large change in CO<sub>2</sub> selectivity and methane conversions between Period A and E at the lower temperatures (500 and 600 °C) for all the catalysts with the exception of LiCoO<sub>2</sub>/YSZ. There was no visible carbon deposits for any of the catalysts exposed in H<sub>2</sub>S. A possible reason for the degradation by H<sub>2</sub>S at the lower temperatures could be that sulfur adsorption occurs more readily at lower temperatures, especially at 500 °C. This was evident in the studies performed by Lui et al. (2003) and Matsuzaki and Yasuda (2000). Thus, more sulfur adsorbed on the catalyst surface results in less active sites for adsorption of methane and oxygen. This leads to a poisoning effect on the catalyst due to sulfur, which makes the catalyst much less active. Generally, at higher temperatures, desorption of methane is more dominant, implying that

the coverage of the methane is smaller on the catalyst surface. This does not mean that the methane oxidation reaction does not take place, but the residence times for surface desorption of methane or reaction are short (Chorkendorff and Niemantsverdriet, 2003). Thus, at higher temperatures, sulfur desorption occurs more readily than adsorption on the surface of the catalyst.

The methane conversion is much lower at Period B, C and D for the Ni/YSZ and Ni/Cu/YSZ catalysts exposed in H<sub>2</sub>S compared to those performed without H<sub>2</sub>S. For example, Ni/YSZ exposed in an H<sub>2</sub>S-free and H<sub>2</sub>S environment at 800 °C in Period C resulted in conversions of 96% and 22%, respectively, while, Ni/Cu/YSZ produced methane conversions of 90% and 46%, respectively. H<sub>2</sub>S poisoning seems to be more pronounced on the Ni/YSZ and Ni/Cu/YSZ. Cu/YSZ produced similar methane conversions in both systems at 700 and 800 °C; therefore, there is not a significant effect on methane conversion by H<sub>2</sub>S at higher temperatures. However, comparing methane conversions performed at Period A and E at 500 and 600 °C, there was a significant drop in methane conversion when the catalysts were exposed to H<sub>2</sub>S, with the notable exception of the LiCoO<sub>2</sub>/YSZ catalysts. In addition, there was a noticeable drop in reactivity of methane at lower temperatures (500 and 600 °C) for all the catalysts except for the LiCoO<sub>2</sub>/YSZ catalysts exposed in H<sub>2</sub>S compared to those exposed without H<sub>2</sub>S. Thus, H<sub>2</sub>S deactivation becomes more apparent at the lower temperatures, which is evident by the methane conversion and CO<sub>2</sub> selectivity results. It can be concluded that the LiCoO<sub>2</sub>/YSZ catalysts did not show signs of H<sub>2</sub>S deactivation at all operating conditions.

### 5.3 Reaction Kinetic Analysis on Methane Oxidation Reactions

The methane oxidation on the catalysts in the absence and presence of H<sub>2</sub>S may involve several elementary steps. Equations (5-1) to (5-12) represent some possible reactions based on the Langmuir-Hinshelwood model. However, the exact mechanism for the methane oxidation reactions is not easily obtained and is quite complex. The following reactions facilitate the discussion of the experimental results, where V is an active site on the catalyst surface.



The reaction kinetics were studied by using a combined power law and Arrhenius relationship as shown by Equation (4-7) in the previous chapter. The Ni/YSZ exposed without H<sub>2</sub>S showed a slightly higher dependence of methane compared to oxygen, which was evident by the calculated methane and oxygen reaction order of 0.976 and 0.757, respectively. The other four catalysts performed without H<sub>2</sub>S resulted in a higher order of oxygen with respect to methane, demonstrating the stronger dependence of oxygen towards methane oxidation. A possible reason for the higher dependence of methane for the Ni/YSZ catalyst could be due to CO production being more dependent on methane, shown by Equations (5-1), (5-3) and (5-5). In contrast with the other catalysts, CO<sub>2</sub> production was more dependent on oxygen concentration, shown by Equations (5-2), (5-4), and (5-6).

It is interesting to note that Itome (2004) reported a negative order of reaction for Ni/YSZ. The negative oxygen order for Ni/YSZ would make sense since oxygen should decrease the rate of reaction because of carbon pyrolysis mainly governed by Equation (5-3) and (5-8). This would cause an increase formation rate of carbon on the catalyst surface, which deactivates the catalyst by reducing the oxygen-adsorbing active sites, thereby increasing oxygen concentration in the gas phase. This in turn, would inhibit CO<sub>2</sub> production and would further inhibit CO production. This was seen earlier by the dramatic decrease in CO<sub>2</sub> selectivity for Ni/YSZ. The negative order of oxygen for Ni/YSZ was not evident in this research, most likely due to the limited amount of oxygen used throughout the reaction (Periods A thru D). Thus, most of the oxygen was adsorbed to carbon to form mainly CO. It is important to note that Itome (2004) did not physically

observe signs of carbon deposits on the Ni/YSZ catalysts which was seen in this study, as discussed earlier.

On the other hand, when Ni/YSZ was exposed to H<sub>2</sub>S the methane reaction order became negative (-0.193). This demonstrates that increasing the concentration of methane, thereby increasing the concentration of H<sub>2</sub>S, decreases the rate of reaction. Therefore, the Ni/YSZ is poisoned by the H<sub>2</sub>S by blocking the active sites with sulfur, inhibiting adsorption of oxygen on the Ni/YSZ catalyst surface. The other four catalysts exposed in H<sub>2</sub>S showed a similar trend to those catalysts performed without H<sub>2</sub>S, which was demonstrated by the higher dependence on oxygen compared to methane. Oxidation of H<sub>2</sub>S to SO<sub>2</sub> may be another possible reaction as shown by Equation (5-10), (5-11) and (5-12). Unfortunately, SO<sub>2</sub> could not be monitored by the mass spectrometer, because its concentration was too low for detection. A study discussed by Meeyoo et al. (1998) involved catalytic methane oxidation reactions on a platinum catalyst in the presence of H<sub>2</sub>S. Meeyoo et al. (1998) found that an increase in the partial pressure of oxygen removed H<sub>2</sub>S through chemical reaction, and hence increased the rate of reaction.

The Ni/YSZ and LiCoO<sub>2</sub>/YSZ catalysts (without H<sub>2</sub>S) have higher activation energies compared to the other catalysts, which means that high temperatures are needed to produce an active catalyst for high methane conversion. The higher the activation energy, the more temperature sensitive the reactions become (Wijngaarden et al., 1998). The pre-exponential factor was shown to be highest for Ni/YSZ. Thus, Ni/YSZ is expected to be the most active catalyst compared to the other catalysts operated at high temperatures. This is consistent with the methane conversion results. For example, Ni/YSZ reacts with methane approximately twice as fast as the LiCoO<sub>2</sub>/YSZ catalysts at

$P_{\text{CH}_4} \sim 6.5$  kPa at 800 °C. Unfortunately, as discussed earlier, carbon deposition was a major problem for Ni/YSZ. On the other hand, Cu/YSZ (without H<sub>2</sub>S) produced the lowest value of activation energy (11.3 kJ/mol), with the lowest pre-exponential factor ( $1.8 \times 10^{-4}$ ), thus resulting in lower methane uptake compared to the other catalysts, especially at higher temperatures. The low activation energy of Cu/YSZ shows that the copper can become active at low temperatures, but is not nearly as active as the other catalysts at the higher temperatures. This is not surprising since copper is known to exhibit poor reactivity towards the oxidation of methane (Park et al., 1999).

The presence of H<sub>2</sub>S had a more pronounced effect on the Ni/YSZ catalyst. This is evident in the drop in the pre-exponential factor (four times smaller). Thus, nickel becomes less active in an H<sub>2</sub>S environment towards the oxidation of methane. The activation energy for the Ni/YSZ catalyst also decreased, suggesting that the rate of disappearance of methane was not affected by temperature nearly as much as Ni/YSZ exposed without H<sub>2</sub>S. Surprisingly, Cu/YSZ in the presence of H<sub>2</sub>S produced a pre-exponential factor that was 25 times larger than the H<sub>2</sub>S-free Cu/YSZ catalyst. Cu/YSZ was more active at the higher temperatures (700 and 800 °C) and becomes deactivated by the H<sub>2</sub>S and thus less active at the lower temperatures. For example, the rate of methane disappearance at  $P_{\text{CH}_4} \sim 10$  kPa was about 12 times larger at 800 °C compared to that at 500 °C. This is consistent with the much higher activation energy possessed by the Cu/YSZ (with H<sub>2</sub>S). The reaction parameters from Table 4-6 demonstrate that Ni/Cu/YSZ exhibits similar trends compared to the Cu/YSZ, although the Ni/Cu/YSZ catalyst without H<sub>2</sub>S showed higher methane reactivity than when H<sub>2</sub>S was present. Therefore, H<sub>2</sub>S did cause some deactivation (loss of activity) in the Ni/Cu/YSZ catalyst



possibly due to the small amount of nickel present on the surface of the catalyst. The LiCoO<sub>2</sub>/YSZ catalysts showed similar calculated reaction parameters for both systems. As discussed earlier, no signs of poisoning on the LiCoO<sub>2</sub>/YSZ catalysts were evident.

It is interesting to note that some noble metal catalysts, such as palladium, have been reported to be active for the oxidation of SO<sub>2</sub> (Meeyoo et al., 1998). Adsorbed oxygen on the metal surface is known to be an important intermediate in the direct oxidation of hydrocarbons (Meeyoo et al., 1998). It was reported by Meeyoo et al. (1998), that any H<sub>2</sub>S or SO<sub>2</sub> present could be oxidized by the adsorbed oxygen on the metal surface to form SO<sub>3</sub>. This might indicate another possible mechanism involved on the Ni/YSZ catalyst surface, in which formation of a nickel sulfate on the surface may result. This would cause deactivation of the Ni/YSZ catalyst, which is evident in this study. However, catalysts such as Cu/YSZ which are known to be less active for oxidation of hydrocarbons, may result in much less adsorbed oxygen on the copper surface; thus methane oxidation would be promoted by the copper metal. In this case, interaction of SO<sub>3</sub> with the support would be more probable. This is consistent with the results for Cu/YSZ and Ni/Cu/YSZ in this study, where no significant influence by H<sub>2</sub>S at the higher temperatures was observed. However, the exact mechanism due to the poisoning affect of H<sub>2</sub>S on these catalysts is not clear.

## Chapter 6

### Conclusions and Recommendations

#### 6.1 Conclusions

This work focused on the effects of hydrogen sulfide on five different anode materials for the application in a hydrogen sulfide compatible SOFC. Reaction kinetic analysis aids in understanding the reactivity of the anode materials on methane oxidation in both an H<sub>2</sub>S-free and H<sub>2</sub>S environment. As discussed in the previous chapter, the Ni/YSZ catalyst without the influence of H<sub>2</sub>S resulted in the most active catalyst and as expected, this led to carbon deposition. On the other hand, the presence of H<sub>2</sub>S suppressed carbon formation on the nickel surface, but degradation due to H<sub>2</sub>S appeared. This was consistent with the results that produced a decreasing rate of methane uptake as the methane concentration increases (negative reaction order). The cause of H<sub>2</sub>S poisoning was due to sulfur adsorption onto the active sites, inhibiting methane and oxygen to adsorb and therefore limiting the methane oxidation reactions. H<sub>2</sub>S degradation was also evident in the Ni/Cu/YSZ catalyst, but did not appear to be as severe as the Ni/YSZ catalyst alone. H<sub>2</sub>S did not appear to affect the Cu/YSZ catalyst at high temperatures. However, Cu/YSZ did exhibit catalyst degradation by H<sub>2</sub>S at the lower temperatures. Similar signs of degradation at low temperatures were also evident in the Ni/YSZ and Ni/Cu/YSZ catalysts. Surprisingly, the LiCoO<sub>2</sub>/YSZ catalysts did not appear to be poisoned by H<sub>2</sub>S at all operating temperatures. Degradation was suppressed at higher temperatures most likely due to the increased desorption rate of sulfur compared to the adsorption rate onto the catalyst surface.

As discussed earlier, the Ni/YSZ catalyst is severely poisoned by H<sub>2</sub>S, which is consistent with previous researchers. Thus, possible replacements for Ni/YSZ would include Cu/YSZ, Ni/Cu/YSZ and LiCoO<sub>2</sub>/YSZ catalysts. Although, the LiCoO<sub>2</sub>/YSZ catalysts appears to be resistant to sulfur at all operating temperatures, the reactivity towards methane oxidation is not as high as the copper catalyst. In addition, the activation energy for Cu/YSZ, Ni/Cu/YSZ and LiCoO<sub>2</sub>/YSZ catalysts exhibits similarly high values. Thus, high temperature operation is required to provide active catalysts and also to avoid H<sub>2</sub>S degradation that occurs at lower temperatures. Therefore, low temperature operation in the presence of H<sub>2</sub>S is not viable for the catalysts studied in this research. The best candidate for an SOFC anode operating in an H<sub>2</sub>S environment at high temperatures would be Cu/YSZ. The reason is that copper produced the highest activity (at high temperatures) compared to the other catalysts and appeared to be resistant to H<sub>2</sub>S. In addition, copper is abundant and economical.

## **6.2 Recommendations and Future Work**

This study gained knowledge and understanding in the area of reaction kinetics on SOFC anode materials and their reactivity towards methane oxidation in the presence of H<sub>2</sub>S. This has led to uncertainties and future recommendations that may aid in improving the study for future work in this area of interest. Catalyst preparation is one area that can be altered to produce a more elaborate comparison of catalyst preparation and its effect on surface characterization. Various stages in preparing the catalysts may have affected the metal distribution and uniformity over the support, as discussed earlier. This would affect the surface area and metal compositions. For example, the Cu/YSZ catalyst

produced the smallest surface area, possibly due to sintering during the calcination process. Calcination temperature and time parameters could be altered and results compared to evaluate their effect on catalyst characterization. The Ni/Cu/YSZ catalyst showed an unusually high and low metal content of copper and nickel, respectively. Wet impregnation of the bimetal catalyst could have been done using a combination of steps. For example, the copper could have been impregnated first followed by drying and calcination, then a second impregnation for the nickel could have been done and vice versa. The characterization results could then be compared among the different preparation methods to examine the effects of catalyst preparation on surface composition and surface area.

In terms of the experimental procedure in developing the methane oxidation reactions, reduction temperature and time could be altered to monitor the effects on metal composition and carbon deposition. It was found in literature that increasing reduction temperature and time significantly suppresses carbon formation. It was also suggested that increasing the reduction temperature led to increased copper enrichment (Kim et al., 2002a). In this study, it was found that all the catalysts with the exception of Ni/YSZ did not exhibit carbon formation. It was also concluded that H<sub>2</sub>S did not affect the LiCoO<sub>2</sub>/YSZ catalysts and the Cu/YSZ catalyst at high temperatures. The methane oxidation reactions could be developed in such a way, to examine the regenerative capabilities of the individual catalysts. For example, the methane oxidation reactions were performed from Period A thru E, which could then be brought back to Period D (least amount of oxygen) for one day then back to Period E for another day to see if the catalysts are able to regenerate from carbon formation and H<sub>2</sub>S poisoning. Other

additional experiments that could have been done would involve reducing the catalysts in the XPS instrument, then analyzing the oxidation state of the metals on the surface of the support.

Calculations such as determining the adsorption constants and the heat of adsorption of methane, oxygen and H<sub>2</sub>S would be helpful in determining the degree of adsorption of each reactant and their effects on methane consumption. This would also allow for evaluation of the inhibition term (H<sub>2</sub>S influence) and thus, the effects of H<sub>2</sub>S concentration on the activity of the catalysts. A suitable kinetic model would have to be developed in order to fit the appropriate data. Attempts have been made to fit this type of model using Langmuir-Hinshelwood kinetics and a deactivation inhibition model. The Langmuir-Hinshelwood model was developed but, unfortunately, the model produced several solutions for the reaction parameters. Thus, it was concluded this model was not sufficiently stable. An inhibition model was also developed, but failed to converge to an appropriate solution and thus was not used in this study.

The study of metal sulfides and their reactivity towards methane oxidation and resistance to H<sub>2</sub>S would have been useful knowledge. Most reported work that has studied metal sulfides as anodes for SOFCs, is related to H<sub>2</sub>S oxidation. Therefore, more research is required on metal sulfides and their reactivity towards direct oxidation of hydrocarbon fuels and their resistance to H<sub>2</sub>S.

It would also be useful to measure the performance of the anode materials studied. For example, screen printing could be used to combine the anode, electrolyte and cathode. A tubular furnace could then be set up to run the reactions and a potentiometer used to measure overall cell voltages and currents produced by the pilot-scale SOFC.

## References

- Aguilar, L.; Zha, S.; Cheng, Z.; Winnick, J.; Liu, M. J. *Power Sources* **2004**, *135*, pp 17-24.
- Antolini, E. *J. Eur. Ceram. Soc.* **1998**, *18*, pp 1405-1411.
- Appenzeller, T.; Dimick, D. *Natl Geogr.* **September 2004**, pp 11-12.
- Attard, G.; Barnes, C. *Surfaces*, Oxford Chemistry Primers, Oxford University Press Inc: New York, 1998.
- AutoChem II 2920 Operating Manual by Micromeritics.
- Bartholomew, C. H.; Agrawal, P. W.; Katzer, J. R. *Adv. Catal.* **1982**, *31*, pp 135-242.
- Cengel, Y. A.; Boles, M. A. *Thermodynamics, An Engineering Approach*, 3<sup>rd</sup> Edition, McGraw-Hill, United States, 1998.
- Chivers, T.; Hyne, J. B.; Lau, C. *Int. J. Hydrogen Energy* **1980**, *5*, pp 499-506.
- Chorkendorff, I.; Niemantsverdriet, J. W. *Concepts of Modern Catalysis*, Wiley-VCH: Weinheim, Germany, 2003.
- Chuang, K. T.; Sanger, A. R.; Slavov, S. V.; Donini, J. C. *Int. J. Hydrogen Energy* **2001**, *26*, pp 103-108.
- Craciun R.; Park, S.; Gorte, R. J.; Vohs, J. M.; Wang, C; Worrell, W. L. *J. Electrochem. Soc.* **1999**, *146*, pp 4019-4022.
- Farrauto, R.; Hobson, M.; Kennelly, T.; Waterman, E. *Appl. Catal., A* **1992**, *82*, pp 227.
- Foger, K.; Ahmed, K. *J. Phys. Chem. B* **2005**, *109*, pp 2149-2154.
- Gardner, F. J. *Proc. Instn. Mec. Engrs. Part A* **1997**, *211*, pp 367-380.
- Gorte, R. J.; Seungdoo, P.; Vohs J. M.; Wang, C. *Adv. Mater.* **2000**, *19*, pp 1465- 1469.
- Hassanzadeh, H; Mansouri, S. H. *Proc. Instn. Mec. Engrs. Part A* **2005**, *219*, pp 245-254.
- Hatae, T.; Kakuda, N.; Taniyama, T.; Yamazaki, Y. *J. Power Sources* **2004**, *135*, pp 25-28.
- He, P.; Liu, M.; Luo, J. L.; Sanger, A. R.; Chuang, K. T. *J. Electrochem. Soc.* **2002**, *149*, pp A808-A814.

- Hongpeng, H.; Gorte, R. J.; Vohs, J. M. *Electrochem. Solid-State Lett.* **2005**, *8*, pp A279-A280.
- Hyuk K.; Vohs J. M.; Gorte R. J. *ChemComm Commun.* **2001**, *22*, pp 2234-2235.
- Israelson, G. *J. Mater. Eng. Perform.* **2004**, *13*, pp 282-286.
- Itome, Masaki MSc. Thesis, University of Alberta, Edmonton, Alberta, 2004.
- Kim, H.; Park, S.; Vohs, J. M.; Gorte, R. J. *J. Electrochem. Soc.* **2001**, *148*, p A693.
- Kim, H.; Lu, C.; Worrell, W. L.; Vohs, J. M.; Gorte, R. J. *J. Electrochem. Soc.* **2002a**, *149*, pp A247 – A250.
- Kim, S. K.; Kim, J. S.; Han, J. Y.; Seo, J. M.; Lee, C. K.; Hong, S. C. *Surf. Sci.* **2002b**, *453*, p 47.
- Liu, M.; He, P.; Luo, J. L.; Sanger, A. R.; Chuang, K. T. *J. Power Sources* **2001**, *94*, pp 20-25.
- Liu, M.; Wei, L.; Sanger, A. R.; Chuang, K. T. *J. Electrochem. Soc.* **2003**, *150*, pp A1025-A1029.
- Luis, A.; Zha, S.; Li, S.; Winnick, J.; Liu, M. *Electrochem. Solid-State Lett.* **2004**, *7*, pp A324-A326.
- M200ED Operating Manual by Dycor, 1994.
- Macintyre, Dictionary of Inorganic Compounds, 1<sup>st</sup> Edition, Chapman & Hall: London, 1992, p 14.
- Majumdar, S.; Claar, T.; Flandermeyer, B. *J. Amer. Ceram. Soc.* **1986**, *69*, p 628.
- Matsuzaki, Y.; Yasuda, I. *Solid State Ionics* **2000**, *132*, pp 261-269.
- Marina, O. A.; Mogensen, M. *Appl. Catal., A* **1999**, *189*, pp 117-126.
- McIntosh, S.; Gorte, J. *Chem. Rev.* **2004**, *104*, pp 4845 – 4865.
- McIntosh, S.; Vohs, J. M.; Gorte, R. J. *J. Electrochem. Soc.* **2003**, *150*, pp A470-A476.
- Meeyoo, V.; Lee, J. H.; Trimm, D. L.; Cant, N. W. *Catal. Today* **1998**, *44*, pp 67-72.
- Minh, N. Q. *J. Amer. Ceram. Soc.* **1993**, *76*, p 563.
- Mogensen, M.; Sammes, N. M.; Tompsett, G. A. *Solid State Ionics* **2000**, *129*, p 63.

- Mogensen, M.; Kammer, K. *Annu. Rev. Mater. Res.* **2003**, *33*, p321.
- Murray, E. P.; Barnett, S. A. J. *Electrochem. Soc.* **1999**, *99*, p 1001.
- Murray, E. P.; Tsai, T.; Barnett S. A. *Nature* **1999**, *400*, p 649.
- Nakagawa, N.; Sagara, H.; Kato, K. *J. Power Sources* **2001**, *92*, pp 88-94.
- National Center for Atmospheric Research*, News release, **July 2001**.
- National Oceanic and Atmospheric Administration, Climate of 2001, Annual review.
- Niemantsverdriet, J. W. *Spectroscopy in Catalysis*, VCH Publishers: Weinheim, 1995.
- Ormerod, R. M. *Chem. Soc. Rev.* **2003**, *32*, pp 17-28.
- Ohzuku, T.; Ueda, A. *J. Electrochem. Soc.* **1994**, *141*, pp 2972-2977.
- Park, S.; Cracium, R.; Vohs, J. M.; Gorte, R. J. *J. Electrochem. Soc.* **1999**, *146*, pp 3603-3605.
- Sangtongkitcharoen, W.; Assabumrungrat, S.; Pavarajarn, V.; Laosiropojana, N.; Spencer, M. S.; Twigg, M. V. *Annu. Rev. Mater. Res.* **2005**, *35*, pp 427-464.
- Stambouli, A. and Traversa, E., *Renew. Sust. Energ. Rev.* **2002**, *6*, pp 433-455.
- Praserthdam, P. *J. Power Sources*, **2005**, *142*, pp 75- 80.
- Pujare, N. U.; Semkow, K. W.; Sammells, A. F. *J. Electrochem. Soc.* **1987**, *134*, pp 2639-2940.
- Steele, B.; Middleton, K. I.; Rudkin, R. *Solid State Ionics* **28-30**, **1988**, pp 1547-1552.
- Steele, B. C. H.; Heinzl, A. *Nature* **2001**, *414*, p 345.
- Tsai, T.; Barnett, S. A. *J. Electrochem. Soc.* **1998**, *145*, p 1696.
- Uchida, H.; Suzuki, H.; Wantanabe, M. *J. Electrochem. Soc.* **1998**, *145*, pp 615-620.
- Wei, G. L.; Luo, J.; Sanger, A. R.; Chuang, K. T. *J. Electrochem. Soc.* **2004**, *151*, pp A232-A237.
- Wijngaarden, R. J.; Kronberg, A.; Westerterp, K. R., *Industrial Catalysis*, Wiley-VCH: Weinheim, Germany, 1998.
- Xia, C.; Lang, Y.; Meng, G. *Fuel Cells* **2004**, *4*, pp 41-47.



Yates, C.; Winnick, J. *J. Electrochem. Soc.* **1999**, *146*, pp 2841-2844.

Yokokawa, H.; Sakai, N.; Horita, T.; Yamaji, K. *Fuel Cells* **2001**, *2*, pp 117-131.

Zha, S.; Cheng, Z.; Liu, M. *Electrochem. Solid-State Lett.* **2005**, *8*, pp A406-A408.

Zhou, Z. F.; Gallo, C.; Pague, M. B.; Schobert, H.; Lvov, S. N. *J. Power Sources* **2004**, *133*, pp 181-187.

### **Websites**

<http://www.asms.org> (accessed October 15, 2005).

<http://www.siemenswestinghouse.com> (accessed July 2004).

<http://www.tosoh.com> (accessed August 2005)

<http://www.seca.doe.gov> (accessed July 2004).

## Appendix A

**Reaction Kinetic Data (Differential reactor) for Ni/YSZ in the absence of H<sub>2</sub>S**

Period	Temp (K)	F <sub>CH<sub>4</sub></sub> ,initial mol/min	Methane Conversion	C <sub>CH<sub>4</sub></sub> ,avg mol/m <sup>3</sup>	P <sub>CH<sub>4</sub></sub> , avg kpa	C <sub>O<sub>2</sub></sub> ,Avg mol/m <sup>3</sup>	dX <sub>CH<sub>4</sub></sub>	Mass of metal (g)	-r <sub>CH<sub>4</sub></sub> mol/min g metal
A	800	4.26E-06	0.980	0.869	2.153	1.725	0.196	0.2533	8.24E-05
B	800	1.70E-05	0.989	1.723	4.268	1.384	0.396	0.2533	1.66E-04
C	800	3.83E-05	0.961	2.656	6.580	1.158	0.577	0.2533	2.42E-04
D	800	1.07E-04	N/A	N/A	N/A	N/A	N/A	N/A	N/A
-----									
A	700	4.26E-06	0.978	0.871	2.157	1.717	0.196	0.3096	6.73E-05
B	700	1.70E-05	0.989	1.723	4.268	1.377	0.396	0.3096	1.36E-04
C	700	3.83E-05	0.941	2.707	6.706	1.037	0.565	0.3096	1.94E-04
D	700	1.07E-04	N/A	N/A	N/A	N/A	N/A	N/A	N/A
-----									
A	600	4.26E-06	0.969	0.878	2.176	1.742	0.194	0.358	5.77E-05
B	600	1.70E-05	0.975	1.747	4.327	1.389	0.390	0.358	1.16E-04
C	600	3.83E-05	0.831	2.988	7.404	1.053	0.499	0.358	1.48E-04
D	600	1.07E-04	N/A	N/A	N/A	N/A	N/A	N/A	N/A
-----									
A	500	4.26E-06	0.649	1.151	2.852	2.162	0.130	0.2937	4.71E-05
B	500	1.70E-05	0.480	2.590	6.417	1.686	0.192	0.2937	6.96E-05
C	500	3.83E-05	0.314	4.310	10.677	1.206	0.188	0.2937	6.83E-05
D	500	1.07E-04	0.136	7.941	19.674	0.414	0.136	0.2937	4.93E-05

**Reaction Kinetic Data (Differential reactor) for Cu/YSZ in the absence of H<sub>2</sub>S**

Period	Temp (K)	F <sub>CH<sub>4</sub>,initial</sub> mol/min	Methane Conversion	C <sub>CH<sub>4</sub>,avg</sub> mol/m <sup>3</sup>	P <sub>CH<sub>4</sub>, avg</sub> kpa	C <sub>O<sub>2</sub>,Avg</sub> mol/m <sup>3</sup>	dX <sub>CH<sub>4</sub></sub>	Mass of metal (g)	-r <sub>CH<sub>4</sub></sub> mol/min g metal
A	800	4.26E-06	0.952	0.893	2.212	1.720	0.190	0.2763	7.34E-05
B	800	1.70E-05	0.597	2.391	5.923	1.396	0.239	0.2763	9.20E-05
C	800	3.83E-05	0.365	4.179	10.354	1.061	0.219	0.2763	8.44E-05
D	800	1.07E-04	0.149	7.885	19.537	0.389	0.149	0.2763	5.74E-05
A	700	4.26E-06	0.950	0.895	2.216	1.723	0.190	0.3035	6.67E-05
B	700	1.70E-05	0.606	2.375	5.885	1.393	0.242	0.3035	8.51E-05
C	700	3.83E-05	0.330	4.269	10.576	1.059	0.198	0.3035	6.95E-05
D	700	1.07E-04	0.135	7.945	19.684	0.388	0.135	0.3035	4.74E-05
A	600	4.26E-06	0.890	0.946	2.343	1.804	0.178	0.2978	6.37E-05
B	600	1.70E-05	0.598	2.389	5.919	1.392	0.239	0.2978	8.55E-05
C	600	3.83E-05	0.310	4.320	10.702	1.059	0.186	0.2978	6.65E-05
D	600	1.07E-04	0.080	8.179	20.265	0.388	0.080	0.2978	2.86E-05
A	500	4.26E-06	0.570	1.218	3.019	2.254	0.114	0.3269	3.71E-05
B	500	1.70E-05	0.550	2.471	6.122	1.408	0.220	0.3269	7.17E-05
C	500	3.83E-05	0.309	4.322	10.709	1.058	0.185	0.3269	6.04E-05
D	500	1.07E-04	0.080	8.179	20.265	0.388	0.080	0.3269	2.61E-05

**Reaction Kinetic Data (Differential reactor) for Ni/Cu/YSZ in the absence of H<sub>2</sub>S**

Period	Temp (K)	F <sub>CH<sub>4</sub>,initial</sub> mol/min	Methane Conversion	C <sub>CH<sub>4</sub>,avg</sub> mol/m <sup>3</sup>	P <sub>CH<sub>4</sub>, avg</sub> kpa	C <sub>O<sub>2</sub>,Avg</sub> mol/m <sup>3</sup>	dX <sub>CH<sub>4</sub></sub>	Mass of metal (g)	-r <sub>CH<sub>4</sub></sub> mol/min g metal
A	800	4.26E-06	0.979	0.870	2.155	1.743	0.196	0.325	6.41E-05
B	800	1.70E-05	0.972	1.752	4.340	1.410	0.389	0.325	1.27E-04
C	800	3.83E-05	0.899	2.814	6.972	1.075	0.539	0.325	1.77E-04
D	800	1.07E-04	0.340	7.072	17.521	0.425	0.340	0.325	1.11E-04
A	700	4.26E-06	0.960	0.886	2.196	1.725	0.192	0.298	6.85E-05
B	700	1.70E-05	0.860	1.943	4.813	1.386	0.344	0.298	1.23E-04
C	700	3.83E-05	0.738	3.226	7.993	1.040	0.443	0.298	1.58E-04
D	700	1.07E-04	0.243	7.483	18.540	0.362	0.243	0.298	8.70E-05
A	600	4.26E-06	0.909	0.930	2.303	1.732	0.182	0.310	6.26E-05
B	600	1.70E-05	0.748	2.133	5.286	1.395	0.299	0.310	1.03E-04
C	600	3.83E-05	0.612	3.548	8.790	1.054	0.367	0.310	1.26E-04
D	600	1.07E-04	0.332	7.106	17.605	0.384	0.332	0.310	1.14E-04
A	500	4.26E-06	0.696	1.111	2.753	2.076	0.139	0.311	4.76E-05
B	500	1.70E-05	0.593	2.398	5.940	1.392	0.237	0.311	8.11E-05
C	500	3.83E-05	0.405	4.077	10.101	1.048	0.243	0.311	8.31E-05
D	500	1.07E-04	0.119	8.013	19.853	0.375	0.119	0.311	4.07E-05

**Reaction Kinetic Data (Differential reactor) for LiCoO<sub>2</sub>/YSZ Prep 1 in the absence of H<sub>2</sub>S**

Period	Temp (K)	F <sub>CH<sub>4</sub>,initial</sub> mol/min	Methane Conversion	C <sub>CH<sub>4</sub>,avg</sub> mol/m <sup>3</sup>	P <sub>CH<sub>4</sub>, avg</sub> kpa	C <sub>O<sub>2</sub>,Avg</sub> mol/m <sup>3</sup>	dX <sub>CH<sub>4</sub></sub>	Mass of metal (g)	-r <sub>CH<sub>4</sub></sub> mol/min g metal
A	800	4.26E-06	0.927	0.914	2.265	1.742	0.185	0.250	7.90E-05
B	800	1.70E-05	0.560	2.454	6.080	1.420	0.224	0.250	9.55E-05
C	800	3.83E-05	0.322	4.289	10.626	1.094	0.193	0.250	8.23E-05
D	800	1.07E-04	0.120	8.009	19.843	0.427	0.120	0.250	5.11E-05
A	700	4.26E-06	0.909	0.930	2.303	1.795	0.182	0.264	7.32E-05
B	700	1.70E-05	0.600	2.386	5.911	1.398	0.240	0.264	9.67E-05
C	700	3.83E-05	0.316	4.304	10.664	1.061	0.190	0.264	7.64E-05
D	700	1.07E-04	0.084	8.162	20.223	0.391	0.084	0.264	3.38E-05
A	600	4.26E-06	0.537	1.247	3.088	2.347	0.107	0.305	3.75E-05
B	600	1.70E-05	0.477	2.595	6.430	1.610	0.191	0.305	6.67E-05
C	600	3.83E-05	0.309	4.322	10.709	1.062	0.185	0.305	6.48E-05
D	600	1.07E-04	0.080	8.179	20.265	0.391	0.080	0.305	2.80E-05
A	500	4.26E-06	0.254	1.488	3.686	2.765	0.051	0.297	1.82E-05
B	500	1.70E-05	0.171	3.117	7.722	2.289	0.068	0.297	2.45E-05
C	500	3.83E-05	0.139	4.757	11.785	1.719	0.083	0.297	2.99E-05
D	500	1.07E-04	0.050	8.307	20.582	0.542	0.050	0.297	1.79E-05

**Reaction Kinetic Data (Differential reactor) for LiCoO<sub>2</sub>/YSZ Prep 2 in the absence of H<sub>2</sub>S**

Period	Temp (K)	F <sub>CH<sub>4</sub>,initial</sub> mol/min	Methane Conversion	C <sub>CH<sub>4</sub>,avg</sub> mol/m <sup>3</sup>	P <sub>CH<sub>4</sub>, avg</sub> kpa	C <sub>O<sub>2</sub>,Avg</sub> mol/m <sup>3</sup>	dX <sub>CH<sub>4</sub></sub>	Mass of metal (g)	-r <sub>CH<sub>4</sub></sub> mol/min g metal
A	800	4.26E-06	0.943	0.901	2.231	1.724	0.189	0.250	8.03E-05
B	800	1.70E-05	0.593	2.398	5.940	1.397	0.237	0.250	1.01E-04
C	800	3.83E-05	0.346	4.228	10.474	1.061	0.208	0.250	8.84E-05
D	800	1.07E-04	0.110	8.052	19.948	0.387	0.110	0.250	4.69E-05
A	700	4.26E-06	0.934	0.908	2.250	1.735	0.187	0.250	7.96E-05
B	700	1.70E-05	0.569	2.438	6.042	1.394	0.228	0.250	9.70E-05
C	700	3.83E-05	0.312	4.315	10.690	1.060	0.187	0.250	7.97E-05
D	700	1.07E-04	0.100	8.094	20.054	0.389	0.100	0.250	4.26E-05
A	600	4.26E-06	0.542	1.242	3.078	2.344	0.108	0.310	3.72E-05
B	600	1.70E-05	0.482	2.587	6.409	1.616	0.193	0.310	6.62E-05
C	600	3.83E-05	0.310	4.320	10.702	1.063	0.186	0.310	6.39E-05
D	600	1.07E-04	0.090	8.137	20.159	0.392	0.090	0.310	3.09E-05
A	500	4.26E-06	0.253	1.488	3.688	2.761	0.051	0.289	1.87E-05
B	500	1.70E-05	0.166	3.125	7.743	2.304	0.066	0.289	2.45E-05
C	500	3.83E-05	0.135	4.767	11.811	1.730	0.081	0.289	2.99E-05
D	500	1.07E-04	0.060	8.265	20.476	0.561	0.060	0.289	2.21E-05

**Reaction Kinetic Data (Differential reactor) for Ni/YSZ in the presence of H<sub>2</sub>S**

Period	Temp (K)	F <sub>CH<sub>4</sub>,initial</sub> mol/min	Methane Conversion	C <sub>CH<sub>4</sub>,avg</sub> mol/m <sup>3</sup>	P <sub>CH<sub>4</sub>, avg</sub> kPa	C <sub>O<sub>2</sub>,Avg</sub> mol/m <sup>3</sup>	dX <sub>CH<sub>4</sub></sub>	Mass of metal (g)	-r <sub>CH<sub>4</sub></sub> mol/min g metal
A	800	4.26E-06	0.927	0.914	2.265	4.553	0.185	0.237	8.33E-05
B	800	1.70E-05	0.400	2.726	6.755	3.760	0.160	0.237	7.19E-05
C	800	3.83E-05	0.219	4.552	11.279	2.944	0.131	0.237	5.90E-05
D	800	1.07E-04	0.098	8.104	20.078	1.313	0.098	0.237	4.39E-05
A	700	4.26E-06	0.813	1.011	2.506	4.763	0.163	0.243	7.14E-05
B	700	1.70E-05	0.349	2.813	6.970	3.556	0.140	0.243	6.13E-05
C	700	3.83E-05	0.155	4.716	11.684	2.731	0.093	0.243	4.08E-05
D	700	1.07E-04	0.070	8.222	20.371	1.060	0.070	0.243	3.07E-05
A	600	4.26E-06	0.669	1.134	2.810	5.270	0.134	0.249	5.72E-05
B	600	1.70E-05	0.273	2.943	7.291	4.255	0.109	0.249	4.67E-05
C	600	3.83E-05	0.115	4.818	11.937	3.699	0.069	0.249	2.95E-05
D	600	1.07E-04	0.065	8.245	20.426	1.047	0.065	0.249	2.77E-05
A	500	4.26E-06	0.394	1.368	3.390	6.333	0.079	0.248	3.39E-05
B	500	1.70E-05	0.152	3.149	7.802	5.132	0.061	0.248	2.61E-05
C	500	3.83E-05	0.080	4.907	12.156	4.164	0.048	0.248	2.07E-05
D	500	1.07E-04	0.030	8.393	20.795	1.807	0.030	0.248	1.28E-05

**Reaction Kinetic Data (Differential reactor) for Cu/YSZ in the presence of H<sub>2</sub>S**

Period	Temp (K)	F <sub>CH<sub>4</sub>,initial</sub> mol/min	Methane Conversion	C <sub>CH<sub>4</sub>,avg</sub> mol/m <sup>3</sup>	P <sub>CH<sub>4</sub>, avg</sub> kPa	C <sub>O<sub>2</sub>,Avg</sub> mol/m <sup>3</sup>	dX <sub>CH<sub>4</sub></sub>	Mass of metal (g)	-r <sub>CH<sub>4</sub></sub> mol/min g metal
A	800	4.26E-06	0.945	0.899	2.227	4.293	0.189	0.242	8.31E-05
B	800	1.70E-05	0.675	2.258	5.594	3.456	0.270	0.242	1.19E-04
C	800	3.83E-05	0.487	3.867	9.582	2.640	0.292	0.242	1.29E-04
D	800	1.07E-04	0.250	7.455	18.471	1.003	0.250	0.242	1.10E-04
A	700	4.26E-06	0.928	0.913	2.263	4.438	0.186	0.250	7.91E-05
B	700	1.70E-05	0.620	2.352	5.826	3.596	0.248	0.250	1.06E-04
C	700	3.83E-05	0.410	4.064	10.069	2.836	0.246	0.250	1.05E-04
D	700	1.07E-04	0.186	7.728	19.146	1.248	0.186	0.250	7.92E-05
A	600	4.26E-06	0.890	0.946	2.343	4.624	0.178	0.247	7.69E-05
B	600	1.70E-05	0.375	2.769	6.861	3.829	0.150	0.247	6.48E-05
C	600	3.83E-05	0.220	4.550	11.272	2.894	0.132	0.247	5.70E-05
D	600	1.07E-04	0.125	7.988	19.790	1.251	0.125	0.247	5.40E-05
A	500	4.26E-06	0.306	1.443	3.576	6.800	0.061	0.254	2.56E-05
B	500	1.70E-05	0.120	3.204	7.937	5.532	0.048	0.254	2.01E-05
C	500	3.83E-05	0.037	5.018	12.433	4.900	0.022	0.254	9.24E-06
D	500	1.07E-04	0.015	8.456	20.951	1.770	0.015	0.254	6.28E-06



**Reaction Kinetic Data (Differential reactor) for Ni/Cu/YSZ in the presence of H<sub>2</sub>S**

Period	Temp (K)	F <sub>CH<sub>4</sub>,initial</sub> mol/min	Methane Conversion	C <sub>CH<sub>4</sub>,avg</sub> mol/m <sup>3</sup>	P <sub>CH<sub>4</sub>, avg</sub> kPa	C <sub>O<sub>2</sub>,Avg</sub> mol/m <sup>3</sup>	dX <sub>CH<sub>4</sub></sub>	Mass of metal (g)	-r <sub>CH<sub>4</sub></sub> mol/min g metal
A	800	4.26E-06	0.963	0.884	2.189	4.397	0.193	0.241	8.51E-05
B	800	1.70E-05	0.661	2.282	5.653	3.678	0.264	0.241	1.17E-04
C	800	3.83E-05	0.462	3.931	9.740	2.911	0.277	0.241	1.22E-04
D	800	1.07E-04	0.223	7.570	18.756	1.353	0.223	0.241	9.85E-05
A	700	4.26E-06	0.950	0.895	2.216	4.331	0.190	0.254	7.98E-05
B	700	1.70E-05	0.590	2.403	5.953	3.544	0.236	0.254	9.91E-05
C	700	3.83E-05	0.373	4.159	10.303	2.744	0.224	0.254	9.40E-05
D	700	1.07E-04	0.123	7.996	19.811	1.122	0.123	0.254	5.16E-05
A	600	4.26E-06	0.832	0.995	2.466	4.697	0.166	0.260	6.82E-05
B	600	1.70E-05	0.541	2.486	6.160	3.562	0.216	0.260	8.86E-05
C	600	3.83E-05	0.307	4.327	10.721	2.665	0.184	0.260	7.55E-05
D	600	1.07E-04	0.090	8.137	20.159	1.036	0.090	0.260	3.69E-05
A	500	4.26E-06	0.375	1.385	3.430	4.849	0.075	0.258	3.10E-05
B	500	1.70E-05	0.149	3.155	7.816	4.190	0.060	0.258	2.46E-05
C	500	3.83E-05	0.062	4.953	12.272	3.371	0.037	0.258	1.54E-05
D	500	1.07E-04	0.093	8.125	20.130	1.824	0.093	0.258	3.83E-05

**Reaction Kinetic Data (Differential reactor) for LiCoO<sub>2</sub>/YSZ Prep 1 in the presence of H<sub>2</sub>S**

Period	Temp (K)	F <sub>CH<sub>4</sub>,initial</sub> mol/min	Methane Conversion	C <sub>CH<sub>4</sub>,avg</sub> mol/m <sup>3</sup>	P <sub>CH<sub>4</sub>, avg</sub> kPa	C <sub>O<sub>2</sub>,Avg</sub> mol/m <sup>3</sup>	dX <sub>CH<sub>4</sub></sub>	Mass of metal (g)	-r <sub>CH<sub>4</sub></sub> mol/min g metal
A	800	4.26E-06	0.956	0.890	2.204	1.762	0.191	0.250	8.16E-05
B	800	1.70E-05	0.618	2.355	5.835	1.456	0.247	0.250	1.06E-04
C	800	3.83E-05	0.425	4.026	9.974	1.147	0.255	0.250	1.09E-04
D	800	1.07E-04	0.193	7.698	19.072	0.513	0.193	0.250	8.24E-05
A	700	4.26E-06	0.849	0.981	2.430	1.877	0.170	0.266	6.81E-05
B	700	1.70E-05	0.555	2.462	6.101	1.409	0.222	0.266	8.90E-05
C	700	3.83E-05	0.329	4.271	10.582	1.081	0.197	0.266	7.92E-05
D	700	1.07E-04	0.085	8.158	20.212	0.420	0.085	0.266	3.41E-05
A	600	4.26E-06	0.387	1.374	3.405	2.592	0.077	0.259	3.19E-05
B	600	1.70E-05	0.321	2.861	7.089	1.942	0.128	0.259	5.29E-05
C	600	3.83E-05	0.293	4.363	10.810	1.221	0.176	0.259	7.24E-05
D	600	1.07E-04	0.090	8.137	20.159	0.422	0.090	0.259	3.71E-05
A	500	4.26E-06	0.234	1.505	3.728	2.820	0.047	0.255	1.95E-05
B	500	1.70E-05	0.178	3.105	7.692	2.481	0.071	0.255	2.97E-05
C	500	3.83E-05	0.146	4.739	11.741	1.956	0.088	0.255	3.65E-05
D	500	1.07E-04	0.107	8.064	19.980	0.718	0.107	0.255	4.46E-05

**Reaction Kinetic Data (Differential reactor) for LiCoO<sub>2</sub>/YSZ Prep 2 in the presence of H<sub>2</sub>S**

Period	Temp (K)	F <sub>CH<sub>4</sub>,initial</sub> mol/min	Methane Conversion	C <sub>CH<sub>4</sub>,avg</sub> mol/m <sup>3</sup>	P <sub>CH<sub>4</sub>, avg</sub> kPa	C <sub>O<sub>2</sub>,Avg</sub> mol/m <sup>3</sup>	dX <sub>CH<sub>4</sub></sub>	Mass of metal (g)	-r <sub>CH<sub>4</sub></sub> mol/min g metal
A	800	4.26E-06	0.948	0.896	2.221	1.731	0.190	0.263	7.69E-05
B	800	1.70E-05	0.593	2.398	5.940	1.405	0.237	0.263	9.62E-05
C	800	3.83E-05	0.380	4.141	10.259	1.075	0.228	0.263	9.25E-05
D	800	1.07E-04	0.095	8.115	20.107	0.418	0.095	0.263	3.85E-05
A	700	4.26E-06	0.885	0.950	2.354	1.824	0.177	0.247	7.62E-05
B	700	1.70E-05	0.543	2.483	6.151	1.412	0.217	0.247	9.35E-05
C	700	3.83E-05	0.327	4.276	10.595	1.083	0.196	0.247	8.45E-05
D	700	1.07E-04	0.088	8.144	20.177	0.422	0.088	0.247	3.80E-05
A	600	4.26E-06	0.429	1.339	3.316	2.565	0.086	0.256	3.56E-05
B	600	1.70E-05	0.345	2.820	6.987	1.932	0.138	0.256	5.73E-05
C	600	3.83E-05	0.302	4.340	10.753	1.231	0.181	0.256	7.53E-05
D	600	1.07E-04	0.100	8.094	20.054	0.431	0.100	0.256	4.15E-05
A	500	4.26E-06	0.237	1.502	3.722	2.770	0.047	0.262	1.93E-05
B	500	1.70E-05	0.170	3.118	7.726	2.401	0.068	0.262	2.77E-05
C	500	3.83E-05	0.140	4.754	11.779	1.825	0.084	0.262	3.42E-05
D	500	1.07E-04	0.101	8.090	20.043	0.571	0.101	0.262	4.11E-05